UNDERSTANDING THE BIOFUNCTION OF RNA G-QUADRUPLEXES IN HUMAN CELLS WITH THE NOVEL FLUORESCENT BINDING LIGANDS

CHAN KA HIN

MPhil

The Hong Kong Polytechnic University

2023

The Hong Kong Polytechnic University

Department of Applied Biology and Chemical Technology

Understanding the biofunction of RNA G-quadruplexes in human cells with the novel fluorescent binding ligands

Chan Ka Hin

A thesis submitted in partial fulfilment of the requirements for the degree of Master of Philosophy

February 2023

CERTIFICATE OF ORIGINALITY

I hereby declare that this thesis is my own work and that, to the best of my knowledge and belief, it reproduces no material previously published or written, nor material that has been accepted for the award of any other degree or diploma, except where due acknowledgement has been made in the text.

_____

Chan Ka Hin

February 2023

Abstract

Cancer is a leading cause of death worldwide. Despite the mechanism of causing cancer is not very clear at present, the overexpression of some oncogenes and their corresponding proteins such as RAS GTPase, RAF kinase, receptor tyrosine kinase KIT and transcription factor MYC in cancer cells usually leads to the suppression of antitumor mechanism and flavor the abnormal cancer cell proliferation. Currently, some drugs such as AMG 510, Sorafenib and Regorafenib have been developed and found able to target several cancers clinically; however, the *in vivo* cytotoxicity selectivity and off-target side effects of these clinical drug remain a great challenge to be overcome. In addition, there are still number of critically important and undruggable targets of cancer which result in a low survival rate and limited treatment options. One of the typically undruggable target of cancer hallmarks is encoded from the RAS family genes. The mutated genes express RAS proteins, the mutated GTPases, for abnormal cancer cell proliferation and only one drug is available for treating KRAS-driven cancers currently. Over the past decades, many studies have revealed that nucleic acids consisting of guanine(G)-rich sequences can adopt a four-stranded structure *in vitro*, which is termed G-quadruplex (G4), and play important roles in both gene transcription and translation in cancer cells. It is reported that the mRNA of oncogenes contains G-rich regions, particularly in the 5'-untranslated region, that may form G4 structures. These mRNA G4s may provide alternative drug targets for their undruggable RAS proteins including KRAS, NRAS and HRAS. It is because the protein expression can be inhibited at translational level through targeting RAS mRNA G4 structures with small-molecules. In this study, we designed and synthesized a series of novel fluorescent ligands that is able to interact and stabilize RNA G4s. Among eighteen ligands synthesized and examined in various *in vitro* and cellular bioassays, one of the ligands, **B3C**, was identified to show the best affinity and selectivity interacting with *NRAS* mRNA G4s. We found that the ligand markedly downregulated NRAS proteins, arrested the progression of cell cycle and induced apoptosis in HeLa cells in a dose-dependent manner. Further experiments suggested that the downregulation of NRAS might restore the activation of DNA damage response,

initiate the DNA repair mechanism, cause S phase prolongation for DNA repair, and ultimately induce apoptosis. To the best of our knowledge, this is the first study targeting *NRAS* mRNA G4 with RNA G4-ligand and provides evidence on restoring the DNA damage response that abrogated by RAS proteins in cancer cells. Cell-based MTT results also showed that **B3C** exhibit a low IC_{50} value about 6.5 against cancer cell lines HeLa, and a relatively high IC_{50} value in non-cancer human cell line HFF1. The results obtained may illustrate that the use of small ligands selectively targeting mRNA G4s of oncogenes such as *NRAS* is a promising anticancer strategy. Our study may provide novel insights into the development of effective therapy against RAS-related cancers.

Acknowledgement

Firstly, I would like to thank my chief supervisor Dr. W. L. Wong for his guidance and support during my M.Phil. study. He taught me how to think critically and solve the problems independently. Also, he can always provide valuable suggestion and comments on my study. I am greatly inspired by his problem-solving skills. I am grateful that he provided me a challenging and meaningful project. I believe that the skill set I learnt from him is valuable for my whole life.

Then, I would express my gratitude to my co-supervisor Prof. K. Y. Wong for his support and advice throughout my study. His ideas can always broaden my horizons on the full picture of the project. Besides, I would like to thank Dr. Y. W. Chen, Dr. Alan S. L. Leung and Dr. S. F. Chung for their assistance in different biological assays.

After that, I am truly appreciative to all of my colleagues in Y606 for their encouragement and assistance. They are always helpful and friendly. On the other hand, I would like to express my special thanks to the scientific officers in ULS for their continuous assistance for handling different equipment.

Moreover, I need to thank my family membranes and friends for their love through those times. Their encouragement is the most important support and let me know I can never give up.

Last but not least, I would like to express my gratitude to the members of the examination committee for spending their precious time on my thesis. I would additionally like to thank the Research Committee of the Hong Kong Polytechnic University for offering me a studentship in 2020-2022 and all the support from the State Key Laboratory of Chemical Biology and Drug Discovery (The Hong Kong Polytechnic University).

Table of Content

Chapter 1. Introduction

Nucleic acids including deoxyribonucleic acid (DNA) and ribonucleic acid (RNA) carry critically important genetic information for all organisms. DNA is a macro-molecule constructed by nucleobases, phosphate groups, and sugars called deoxyribose. The nitrogen-containing nucleobases such as adenine (A), thymine (T), cytosine (C) and guanine (G) connect with deoxyribose sugar groups to give a nucleoside. These nucleosides are joined with one another by phospho-diester linkage, which results in an alternating sugar-phosphate backbone. The connection of two separate polynucleotide strands through hydrogen bonds according to base-pairing rules (A pairs with T and C pairs with G) makes the well-known canonical double helix DNA.[1] RNA is similar to DNA but they have some distinctive features different from each other. Apart from lacking the complementary strand, the major structural differences of RNA are the 2'-hydroxyl group in the sugar backbone and the displacement of thymine (T) with uracil (U). For DNA secondary structures, in addition to the classical double helix structure, other noncanonical structures such as G-quadruplexes and i-motif are also reported and these special structures are generally believed taking important biofunctions in cells.[2-4]

1.1. Discovery of DNA and RNA G-quadruplexes

It was long thought that DNA was far less varied in both primary and secondary structure because there were only four types of building blocks for DNA construction. In 1988, Sen and Gilbert observed the formation of a non-helical secondary structure from a G-rich single-stranded DNA sequence.[5] Under physiological salt concentration, the G-rich sequence were self-associated and gave a four-stranded G-quadruplex (G4) structure. Further studies revealed that the formation of G4 structure showed effects on meiosis. The discovery of the noncanonical DNA secondary structures and its relevance to vital biological functions attracted great attention. The exploration of the G4s then began. Later studies revealed the existence of potential G4-forming sequences (PG4Ss). PG4Ss are the sequences that have at least 4 consecutive guanine residues and each

consecutive has at least 2 guanine nucleotides. PG4Ss usually have the sequence pattern of $G_{\geq 2}$ N_{1-7} $G_{\geq 2}$ N_{1-7} $G_{\geq 2}$ N_{1-7} $G_{\geq 2}$. A study predicted that the number of PG4Ss found in the human genome was more than 700,000 if intra and intermolecular structures of G4s are included.[6] For the DNA G4s identified in mammalian cells, they are found mainly located in functional regions, such as gene promoters, telomeres, and ribosomal DNA(rDNA).[7] Three years after the discovery of DNA G4s, RNA G4s were also discovered. In the study, Kim *et al.* extracted a short sequence from *Escherichia coli*, which was a rRNA located at the 3'-end region and was able to fold into G4s.[8] This finding was regarded as the first proof of the existence of RNA G4s. Over the past two decades, various studies have evidently demonstrated the formation of RNA G4s *in vitro*. As RNA contributes to post-transcriptional processes, it was believed that most of the RNA G4s were located in untranslated regions(UTRs). However, with more studies, RNA G4s were found not only in different classes of RNAs but also in various functionally distinct regions with the same type of RNA. For instance, in a sequence of mRNA, G4s can be presented in 5'-UTR, open reading frame (ORF), and 3'-UTR, which are the three functional regions of mRNA.[9]

1.2. Structure and properties of G-quadruplexes

G4s are a class of non-canonical secondary structure of nucleic acids formed by the guanine-rich sequence in both DNA and RNA. G4s are constructed by stacking of G-quartets, a square-planar arrangement of four guanine nucleobases assembled through Hoogsteen hydrogen bonding (Figure 1.1). The self-stacking of two or more G-quartets generates a G4 structure, which is further stabilized by cations between each of the stacks via the interaction with the 6' carbonyl oxygen of guanine. However, it was found that not all cations were suitable for the stabilization of G4s. Some early studies suggested that the stability of monovalent cations to G4s was in the order of $K^+ > Rb^+ > Na^+ > Li^+$.[10] Nonetheless, for divalent cations, Sravani *et al.* suggested that the stability order is $Sr^{2+} > Ba^{2+} > Pb^{2+} > Ca^{2+} > Mg^{2+}$.[11] At the same time, not all divalent cations contributed to G4-stabilization. It was also reported that Zn^{2+}, Cd^{2+}, Ni^{2+}, and Mn^{2+} disrupted G4 structures even

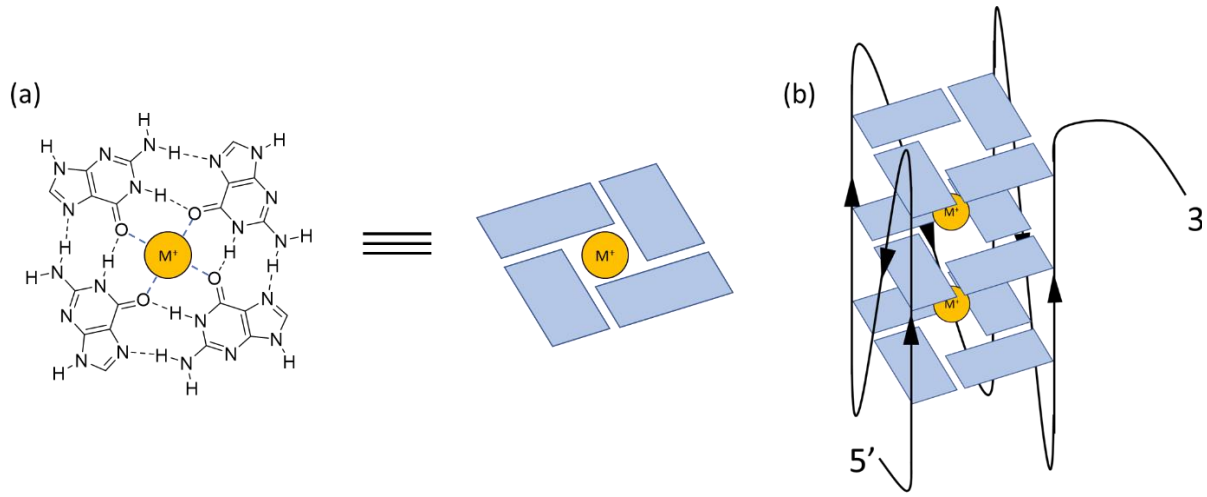

Figure 1.1. The basic structure of G-quadruplex. (a) A planar arrangement G-quartet. (b) The stacking of G-quartet to form a G4-structure stabilized with metal ions.

in the presence of K^+ ions. Altogether, the stabilization ability of ions can be attributed to the ionic radius, dehydration energy, and binding strength of ions to guanine O6.[12] However, due to the physiological existence of potassium ions and sodium ions, and potassium ions have higher stabilizing, potassium ions are thus frequently used to stabilize G4s in experiments.

G4s can be formed with various topologies that are affected by the orientation of strands. Generally, the topologies are divided into three types, including parallel, antiparallel, and hybrid.[4] Among these two topologies, both DNA and RNA G4s show similar rise, twist, and planar shapes within a single G4 (Figure 1.2a). Parallel G4s have their strands orientated in the same direction, while for antiparallel G4s, at least one of their strands is orientated in a different direction. For the specific structural difference, it is depending on the loop of the linker nucleotide between the continuous G-nucleotides. Three kinds of loops including propeller loop, lateral loop, and diagonal loop were identified from early studies (Figure 1.2b).[4] For propeller loops, the loop joins an adjacent phosphate backbone on the opposite G4 surface. As this loop orientates all the strands from bottom to top (or top to bottom), which show the same direction, it is the only loop that shows in parallel G4s. At the same time, the loop that links the adjacent strand on the same G4 surface is the lateral loop. The diagonal loop is the loop that connects two opposite strands on the same surface. Both

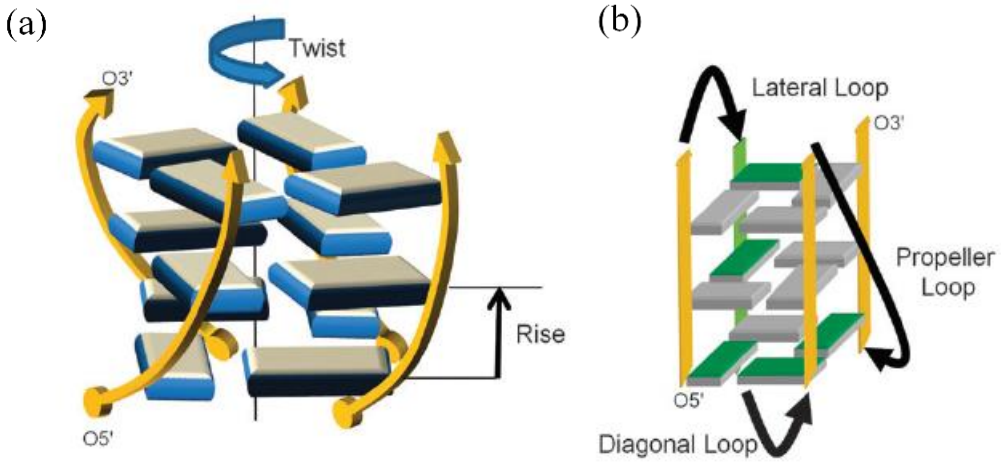

Figure 1.2. A G4 structure showing the (a) rise, twist, and planar shape; (b) the propeller loop, lateral loop, and diagonal loop.

lateral loop and diagonal loop orientate the strands on the same surface. In other words, as they show different directions of the strands, the two loops will be classified as antiparallel topologies. For DNA G4s, they can exist in the forms of parallel, anti-parallel, or hybrid topologies. However, RNA G4s mostly fold into parallel topology. This is due to the presence of 2'-hydroxyl groups in the RNA backbone.[13] Compared with DNA, the ultimate structural differences come from the existence of 2'-hydroxyl group and the absence of 5'-methyl group in uracil(U) in RNA. Among them, the 2'-hydroxyl groups appear to show higher importance due to their larger size when compared to the 2'-proton in DNA. As a result, there are additional steric constricts at the glycosidic bond, which is the bond between bases and sugar. This forces the glycosidic bonds to be in an anti-confirmation. Therefore, the topology of RNA G4s is mostly parallel. Besides, among each topology, the G4-structure formed can be intramolecular, bimolecular, or tetramolecular. For example, in a tetramolecular G4, four short sequences of *d*(TGGGGT) are associated together and thus called tetramolecular G4s. On the other hand, two sequences of linkers containing continuous G-nucleotides such as *d*(GGGGTTTGGGG) associate into bimolecular G4s. Last but not least, the self-folding of a single sequence into G4s is called intramolecular G4s.

In terms of stability, although DNA and RNA G4s generally showed an increase in stability when the loop length decreased, it was reported that RNA G4s had higher thermodynamic stability than DNA G4s. For this distinct difference, it is attributed to the presence of 2'-hydroxyl groups in RNA. There are two mechanisms in which the 2'-hydroxyl groups stabilize the RNA G4s. First, it provides additional intramolecular interaction in terms of several hydrogen bond donors and acceptors. For instance, hydroxyl groups contact with O4' atoms in ribose, phosphate group, and nitrogen atoms in guanines that are involved in the G-quartet. With all the additional interactions, the structure of RNA G4s is more ordered. Many studies have been performed to compare the stability of DNA and RNA G4s. From an early study, Sugimoto *et al.* chose a naturally existing sequence, a BCL-2 gene, for comparison.[14] After experiments, they confirmed that RNA G4s had higher stability than DNA G4s. By doing more tests, they revealed that there was a notable difference in hydration patterns. As the DNA and RNA from of BCL-2 shared almost no difference, like G4 topology and nucleotides, apart from the ribose and deoxyribose, the significant difference in hydration pattern seemed to be critical in terms of stability. Later, a study reported by Sacca and co-workers further confirmed the importance and functions of 2'-hydroxyl groups on G4-stability.[15] They performed experiments by modifying the substituent at the C2-position, phosphate group, and T/U bases. The results illustrated the destabilization of G4s once 2'-hydroxyl groups were removed. Combined the finding of the other similar studies, it was found that 2'-hydroxyl groups contributed to the high thermodynamic stability of RNA G4s.

Furthermore, RNA G4s showed a higher G4 folding tendency than DNA G4s. The main reason is probably due to the absence of a complementary strand.[15, 16] As mentioned above, RNA G4s have higher thermodynamic stability than the equivalent DNA G4s. Given that G4s are a more stable secondary structure, the sequences thus tend to fold into G4s if there is no other competitor for stabilization. As a result, compared to single-stranded RNA, the formation of RNA G4s structure is more favorable. While for DNA G4s, as they contain complementary strands, they are stabilized by the complements. The folding of G4s is thus relatively less favored.

1.3. Bio-functions of G-quadruplexes

1.3.1. Bio-functions of DNA G-quadruplexes

DNA G-quadruplexes containing genes have been implicated in various regulation processes, from telomeres to genomic regions, as well as oncogenes and tumor suppressors. Some typical examples on DNA G4s associated regulation processes are discussed in the following sections.

1.3.1.1. Telomere regulation

Telomere is the end of the chromosomes that consist of a hexanucleotide repeating sequence $d(TTAGGG)_n$ playing a crucial role in genomic integrity.[17] The telomeric DNA has a length around three to seven kilobases. It is interesting that the last 100 to 200 nucleotides at the 3' end are single-stranded instead of the well-known double-stranded DNA structure.[18] Although single-stranded overhang is associated with a number of single-strand telomere binding proteins such as POT1[19] for telomere end-protection and thus G4s are not extensively formed, this G-rich ssDNA is in principle available to form G4s as it is free from the Watson-Crick base pairing. In fact, several studies already revealed that the induction and stabilization of G4s in 3' single-stranded end was effective to hinder the elongation of telomere.[20-23] It is due to fact when telomerase, such as human telomerase reverse transcriptase (hTERT), assembles the nascent telomeric DNA to the 3' single-stranded telomeric DNA by hybridizing with the complementary RNA template from telomerase, the 3' end telomeric DNA must be single-stranded in the absent of other single-strand telomere binding proteins. Thus, the enzymatic activity of telomerase is inhibited when the 3' single-stranded end is converted into the G-quadruplex motif.

1.3.1.2. Transcription regulation

In parallel with telomeric regulation with G4s, the expression of gene is also regulated through G4s formation in genomic regions. In fact, numerous G4s are found in different oncogenes. For instance, the oncogene c-MYC has a 27-nt G-rich DNA sequence that adopts an intramolecular parallel-stranded G4 conformation.[24, 25] This G-rich sequence is located at position -142 to -115

upstream the P1 promoter, termed hypersensitivity element III_1 (Pu27), in which 85-90% of c-MYC transcriptions are activated and controlled by Pu27.[26-28] Grand[29] and Long[30] reported that the stabilization of Pu27 with ligand *in vitro* and *in vivo* inhibited the transcription of the gene and the expression of c-MYC. Apart from c-MYC, the oncogene c-KIT was identified containing two G-rich sequences located upstream the promoter near the SP1 (an activating transcription factor) and the sequences were able to fold into G4s.[31] Bejugam *et al.*[32, 33] reported that the stabilized c-KIT G4s in promotor region down-regulated the expression of c-KIT. These examples illustrated that the G4-ligand complex could be an effective impediment toward the association of transcription factor. Furthermore, several tumor suppressive genes were found containing G-rich sequences that were able to form G4 structures. The retinoblastoma (Rb) gene encoded the tumor suppressor protein, pRB, and played a critical role in preventing excessive cell growth by inhibiting cell cycle from progressing.[34] In addition, Murchie[35] and Xu[36] demonstrated that there was an antiparallel intramolecular G4s formation in the G-rich region of RB gene promoter. The formation of G4s in RB gene was also associated with genomic rearrangement breakpoints, which were contributed to double-strand breaks(DSB) and destabilization of gene.

1.3.2. Bio-functions of RNA G-quadruplexes.

RNA G4s participate in a lot of intracellular regulations. Although RNA G4s primarily affect the post-transcription, various kinds of RNA G4s play different roles before proteins being expressed. As a lot of RNA G4s are reported implicating in the regulation of proteins expression. Some important examples are selected for discussion in the following sections.

1.3.2.1. Translational regulation

Generally, RNA G4s for translational regulations attract the most attention and they are divided into two types including repression and augmentation. In terms of repression, the first finding of translational repression by RNA G4s was reported by Kumari and co-workers.[37] They found that the thermodynamically stable G4s in 5'-untranslated regions (UTR) of the transcript of human

neuroblastoma RAS (NRAS) proto-oncogene down-regulated its protein expression. Although the studies were performed by cell-free translation reporter assay, which was an *in vitro* experiment, their results had important implications for RNA G4s in terms of regulating translations. Later studies reported by Arora *et al.* revealed the inhibition of proteins expression by inducing the formation of RNA G4s in 5'-UTR of human Zic-1 in eukaryotic cells.[38] These examples further illustrated the function of using RNA G4s in translational regulation. Apart from the inhibition of proteins expression, the up-regulation of protein expression was found carried out by RNA G4s. Morris and co-workers illustrated the up-regulation of protein expression by the G4s within the 5'-UTR of human VEGF mRNA.[39] They found that the G4s within the 5'-UTR of human VEGF mRNA were capable to initiate the cap-independent translation by recruiting 40S ribosomal subunit. The results indicated that human VEGF mRNA did not require a 5' cap to initiate scanning from the 5' end of the mRNA until the start codon before expressing this protein. Based on these studies, researchers suggested that RNA G4s may function as a roadblock to stop the progress of the ribosome complex, recruit inhibitory factors to repress mRNA translation, and interact with activating factors to enhance protein expressions.

1.3.2.2. Transcription termination

In addition to translational regulation, RNA G4s were found capable of terminating the transcription process. Wanrooij *et al.* reported that a G-rich RNA sequence found in mitochondria, during transcription of conserved sequence block II (CSB II), could fold into a G4-structure and weaken the interaction between mitochondrial DNA and mitochondrial RNA polymerase (POLRMT).[40] They performed several experiments to investigate the termination efficient by disrupting the G4-structure formed in the sequence. The results indicated that there was a significant decrease in termination after the mutation of the RNA G4 sequence. In other words, the result could support that RNA G4s were the main determinant of premature transcription termination by blocking polymerases from passaging.

1.3.2.3. mRNA maturing

One of the most important steps to mature mRNA is 3'-end processing. This essential step ensures that the mRNA is endonucleolytically cleaved and a poly-A tail is added. Beaudoin and co-workers reported that a G4 in the 3'UTR of FXR1 mRNA could alternately polyadenylate the mRNAs.[41] As a result, several short transcripts were generated and thus the gene regulations were affected.

1.3.2.4. Alternative splicing

It is common in cells to undergo alternative splicing, which is a process to produce various protein products from a limited number of genes, to express various proteins. In fact, RNA G4s participate to mediate the regulations. Gomez *et al.* reported that the RNA G4s located in intron 6 of hTERT pre-mRNA could inhibit the intronic splicing.[42] Consequently, the expression of proteins would be inhibited. In contrast, another study reported by Blice-Baum and co-workers illustrated G4s in exon 15 of FMR1 pre-mRNA could enhance its alternative splicing[43]. From these examples, RNA G4s show regulatory functions to up- or down-regulate pre-mRNA splicing.

1.4. G4-ligands targeting RNA G-quadruplexes and their applications

RNA G4s are known important higher-order biomolecules that serve for cellular regulations by performing translation regulation, transcription regulation, mRNA maturing and alternative splicing. Theoretically, when RNA G4s are formed *in-situ*, despite the folding process may be just transient, the structure could be targeted and stabilized with G4-ligands. In addition, because of the abundance of G4-strcutures in RNA sequences, RNA G4s are found valuable in treating RNA related diseases, which could be from diagnosis to therapeutics. In the following, four most studied fields including molecular sensing and live cell imaging, cancer therapy, neurological disorders, and viral pathogenesis are discussed.

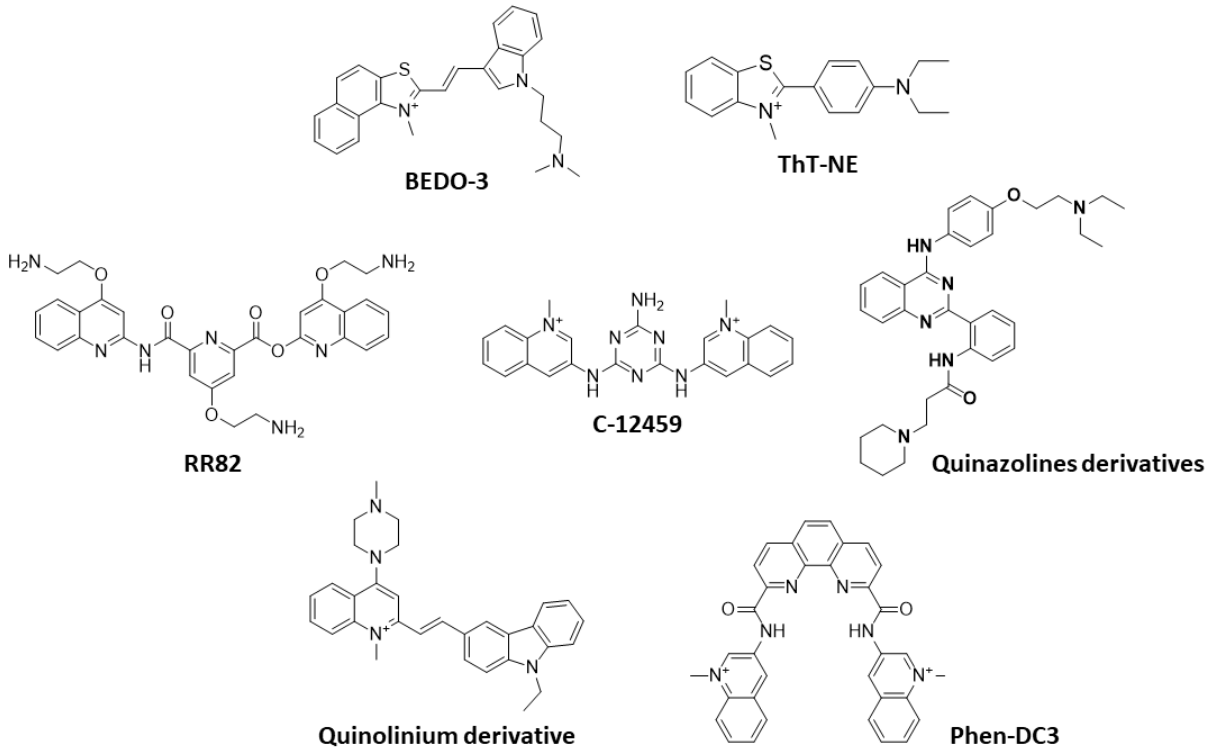

Figure 1.3. Discovered RNA G4 ligands in various fields of application.

1.4.1. Molecular sensing and live cell imaging

After the unravelling of the existence of G4s, studies to prove the locations and functions of both DNA and RNA G4s were performed. Fluorescent binding ligands were commonly used as a chemical tool because of their high sensitivity of fluorescence and the convenience of measuring enhanced fluorescence upon the addition of nucleic acid sequence for *in vitro* screening. Yu *et al.* reported a series of RNA G4 binding ligands (BEDO-1 to BEDO-3).[44] By using molecular modelling, the ligands were designed, optimized, and synthesized rationally based on BEDO-0, an RNA fluorescent probe. The result showed that BEDO-3 (Figure 1.3) had high selectivity toward RNA G4s. In addition, the limit of detection (LOD) calculated for the detection of RNA G4 FMR1 in buffer and in cells were found to be 0.43 nM and 1.08 nM, respectively. Comparing to a commercial RNA G4 specific fluorescent probe, QUMA-1, the LOD of BEDO-3 was 5-fold higher. It indicated that the BEDO-3 was capable to be an RNA G4s sensor due to its highly sensitive property. Another study reported by Chen *et al.* showed a novel RNA G4s fluorescent probe that binds to both RNA G4-structure and the tail sequence in a manner of G-quadruplex-triggered

fluorogenic hybridization (GTFH) [45]. The results illustrated the high selectivity of this ligand binding to 5'-UTR of *NRAS* mRNA. By mutating the nucleotides in sequences to disrupt G4-structure formation, the fluorescent signals were reduced significantly. It was thus confirmed that the binding site of the ligand was the G-quadruplex. Besides, live cells imaging studies by transfecting a long RNA into cells showed that the fluorescent foci had the similar trend as the *in vitro* result. This GTFH probe revealed a new pathway for further development of RNA G4-selective probes.

1.4.2. Cancer therapy

The investigation of RNA G4 ligands in cancer therapy is one of the most popular research topics. It is probably because of the crucial roles RNA G4s playing in cancer cell proliferation such as metastasis, angiogenesis, replication, self-sufficiency, and apoptosis. Thus, RNA G4s are regarded as a promising drug target for anticancer therapy. Three important G4-ligands targeting different hallmarks of cancer are selected for discussion in the following. RR82, a ligand reported by Bugaut *et al.*, was found able to bind to the G4s formed from 5'-UTR of *NRAS* mRNA.[46] *NRAS* mRNA is a kind of oncogenes that contribute to cancer and encodes protein p21, which responds for mediating signal transduction pathways for cell proliferation and differentiation. The interaction and stabilization of *NRAS* mRNA G4s with ligands could inhibit the translation of the oncogene. RR82 could be able to inhibit the cancer cells from undergoing self-sufficiency. Gomez and co-workers adopted another approach by targeting the human telomerase reverse transcriptase (hTERT) RNA G4s.[42] According to the study, the ligand, C-12459 (Figure 1.3), was illustrated to bind to the G4s in hTERT pre-mRNA in the PCR-stop assay. Then, by using RT-PCR, they found that C-12459 could significantly down-regulate the expression of the hTERT transcript by altering the splicing pattern of its pre-mRNA. The result showed that the active +α and +β transcripts which responded to the over-expression of telomerase for cancer immortalization were almost disappeared. In addition, the inactive -β transcripts became the dominant among +α, +β and -β transcripts. This phenomenon was probability due to the result of the alternative splicing of mRNA,

which suggested the feasibility of using RNA G4 ligands to control the splicing of pre-mRNA. This work provided new insights into addressing the limitless replication of cancer cells through RNA G4s. Another study reported by Wang *et al.* demonstrated the use of a quinazoline derivative (Figure 1.3) to down-regulate the human vascular endothelial growth factor (hVEGF) translation.[47] The hVEGF is an angiogenic growth factor that plays important roles in tumor progression. Over-expression of this protein may enhance the vascular formation in tumor. As a result, more blood and nutrients were supplied to the tumor and thus supporting the fast growth of tumor. The interaction of the ligand with G4s of VEGF mRNA destabilized the G4-structure and inhibited the expression of VEGF proteins. Finally, the growth of tumor cells was inhibited. This study indicated an indirect approach to control cancer cell growth, and this is an inhibition of the sustained angiogenesis of cancer cells.

1.4.3. Neurological disorders therapy

In addition to cellular regulations in cancer cells, RNA G4s may be involved in the activation of neurological disorders. Dai *et al.* reported a strategy to inhibit the formation of β-amyloid(Aβ), the neurotoxic peptides that may lead to Alzheimer's disease (AD), by stabilizing the G4 in 5'-UTR of ADAM10 mRNA with RNA G4s ligand (Figure 1.3) [48]. In general, the neurotoxic Aβs are generated from the amyloidogenic process by amyloid precursor protein (APP). Interestingly, the final protein produced could be cleaved by three different kinds of secretases, termed as the α, β, and γ secretases. Under the cleavage of β and γ secretases, neurotoxic Aβs were produced. While α-secretase liberates another product, the neuroprotective sAPPα. The activities of this α-secretase were greatly affected by ADAM10 mRNA. In the study, the ADAM10 mRNA G4 selective ligand showed a dual-function, which enhanced the activities of α-secretase and competed out the cleavage from β and γ-secretase to inhibit the formation of Aβ. They also found that the ligand functioned by interfering proteins binding to RNA G4s. Overall, this study revealed a new molecular strategy to modulate the translation of neurological-related proteins.

1.4.4. Antivirus

Last but not least, RNA G4s ligands could be applied for viral therapy. Jaubert *et al.* reported the use of G4 binding ligand, Phen-DC3 (Figure 1.3), to inhibit the replication of the Hepatitis C virus (HCV) in cells.[49] In the study, they revealed that the last 157 nucleotides at the 3' end of HCV (-) strand containing a highly conserved G4-prone sequence that was located in the stem-loop. Also, the existence of this G4 structure was found essential for viral replication. The results showed that there was a 30% decrease in RNA replication when G4-structures were induced by KCl. Furthermore, the incubation of PhenDC3 with an RNA template and HCV RNA-dependent RNA polymerase (RdRp) was found to reduce the RNA synthesis in the virus by 76%. In addition, the RdRp activity had not been affected. The results indicated that the stabilized G4s in HCV could affect the RNA replication. This work provides new insight into the inhibition of the virus from growing by targeting the viral RNA G4s.

1.5. The advantages of targeting RNA G-quadruplexes for cancer therapeutic study

After the discovery of DNA G4s, a lot of researchers focused on its structure and already revealed various significant results including the potential DNA G4s sequences, bio-functions of DNA G4s, potential G4s binding scaffold, and specific DNA G4s targeting ligands. The research is now moving to the utilization of G4-ligands to target a specific DNA G4 sequence. This directs the research topic from the understanding of G4-structures to the control of their bioactivities with G4-ligands in live cells. From literature, it is reported that DNA G4 ligands could be used to treat cancers. Furthermore, many ligands have been successfully developed to inhibit the expression of oncogenes that contribute to cancers. Some of these G4-ligands such as CX-3543[50] and CX-5461[51, 52] have been tested in clinical trial against cancers. These examples may brighten the future of using G4-structure as the drug target in drug discovery against human disease. In recent years, a lot of studies have reported that RNA G4s frequently take part in cellular regulations and play important roles especially in transcription and translation. To the best of our knowledge, the

research on RNA G4-ligand development is far less than that of targeting DNA G4s. The reasons might be due to the difficulty in targeting RNA G4s with ligands in cells. There are several difficulties for targeting RNA G4s with ligands compared to DNA G4s. First, the reason could be due to the requirement of highly specific ligands to a single RNA sequence among a large amount of G4-folding RNA sequence, proteins, and organelles. To achieve higher selectivity and binding affinity to RNA G4s, the design of ligands should be based on the ordered structures and the spatial environment, such as the length and the nucleotides of loops, of the RNA G4-strucure. However, it is difficult as there is only one crystal structure of RNA G4s reported so far.[53] Besides, the lifetime of RNA is short, which can be as short as several minutes.[54] This restricted the application of small molecules on several important G4s containing RNA sequence. Despite a few ligands have been reported to be selective to RNA G4s in recent years, there are a lot of unknown aspects regarding the rational design of RNA G4-specific ligands, the bio-function of RNA G4s, the mechanism in regulation of RNA G4s function with the ligand and the potential of using RNA G4s as the drug target in disease therapeutics.

Over the past decade, the therapeutic potential against human cancers and other diseases by targeting RNA G4s have been an emerging research topic because the induction and stabilization of RNA G4s with potent and specific small organic ligands may be able to provide alternative strategy for targeting undruggable mutated proteins, such as the mutated RAS family. Targeting RNA G4s compared to that of DNA could show some advantages in drug discovery. It was found that DNA G4s may cause replication stress by obstructing the progression of DNA replication.[55, 56] The replication stress generates double-strand breaks and cause genome instability eventually.[2] Previous studies in *Xenopus laevis*, a clawed fog model, revealed that the absence of G4s unwinding helicase, such as FANCJ or Pif1, or the presence of G4-stabilizing ligands increased genomic instability[57, 58]. In contrast, because RNA acts as temporary translational molecules, the stabilization of RNA G4s by ligands may reduce the possibility of genomic instability. In

addition, RNA G4s sequences are found usually over-represented in the 5'-UTR of many human proto-oncogene, and with high stability and strong self-folding tendency. Therefore, RNA G4s could be considered as a better alternative of DNA G4s for being used as a potential drug target for chemical biology and drug discovery. For this purpose, our group have attempted to explore novel and fluorescent RNA G4-selective ligands for understanding their biological effect in RNA-related process.

1.6. Discovery of novel ligands targeting *NRAS* mRNA G4s for anticancer study in this project

The neuroblastoma RAS (*NRAS*) is a proto-oncogene and belongs to the superfamily of three RAS oncogenes (*NRAS*, *KRAS*, and *HRAS*), which encode for highly homologous monomeric small (20-25 kDa) guanosine triphosphate (GTP)-binding proteins.[59, 60] The RAS proteins play a crucial role as molecular switches governing the activation of a network of signaling pathway.[61] Briefly, the extracellular growth factors activate RAS by recruiting guanine nucleotide exchange factors (GEFs) that catalyze the exchange from RAS-guanosine diphosphate (RAS-GDP) for RAS-guanosine triphosphate (RAS-GTP), in which the GTP-bound RAS is the active form for transmitting signals to downstream effector proteins such as RAF-MEK-ERK (also known as the mitogen-activating protein kinase, MAPK, pathway), and phosphatidylinositol 3-OH kinase (PI3K) for cell growth, proliferation, and differentiation.[62] Upon hydrolysis by GTPase-accelerating proteins (GAPs), the active RAS-GTP is exchanged back to RAS-GDP and the signals are thus terminated.[63, 64] However, the mutated RAS, such as mutated NRAS proteins, binds to GTP more tightly and impairs the GTP to GDP hydrolysis by GAPs. Therefore, the protein complexes are locked in an active state and transmitting the signals continuously for abnormal cell proliferation[65]. According to literature, RAS is critical for inducing abnormal cell proliferation, migration, and survival in cancer cells.[62] Also, it is reported that the mutation of *NRAS* accounts for about 15% of RAS related human malignancies, which are in codon 61 of *NRAS*: CAA

(glutamine) to CGA (arginine) or AAA (lysine).[66-68] Thus, targeting NRAS is considered as a promising strategy for anticancer therapy. However, unlike the FDA approved KRAS inhibitor AMG510,[69] NRAS-mutated human malignancies do not have any approved targeted inhibitor or therapy currently.[70] The reason of failure on directly targeting NRAS is due to the extremely high affinity of NRAS to the high intracellular concentration of GTP. Drugs, such as small molecules, are thus unable to compete out the GTP from RAS. Several strategies are raised by targeting upstream effectors of NRAS, downstream effectors of NRAS, combining MAPK inhibitors and PI3K inhibitors, and combining MAPK inhibitors with cell cycle regulator protein inhibitors. Some of these strategies were even entered the clinical trials. However, all of them failed because of the low inhibiting efficient, unaccepted toxicity or the compensatory of signaling within pathways.[65] Recent studies revealed that there is a G-rich sequence in 5'-UTR of the human *NRAS* proto-oncogene mRNA, which is located 222-nt upstream of translation start site (TSS).[37] The G-rich sequences are capable of forming G4-structures, which may play a various of regulation roles. The strategy of targeting and stabilizing *NRAS* mRNA G4s could be a potential therapeutic to direct downregulate the undruggable mutated NRAS proteins.

In the present study, we designed a series of fluorescent ligands to target mRNA G4s. Among the new G4-ligands synthesized and screened *in vitro*, the ligand, **B3C**, was identified interacting with *NRAS* mRNA G4s with strong affinity, downregulating the cellular NRAS protein expression, arresting cell cycle and inducing apoptosis of cancer cells in a dose-dependent manner. The experimental details of ligand design and synthesis, *in vitro* screening assays, cellular binding assays, and anticancer mechanism upon **B3C** treatment in human cancer cells will be discussed in-depth in the following chapters.

In chapter 2, the rational design and synthesis of new fluorescent G4-ligands and the screening methods to investigate the interaction between the ligands and various nucleic acid substrates including DNA and RNA G4s will be a focus of discussion. Besides, the validation of the target of

ligand both *in vitro* and *in cellulo* will be discussed. The results obtained from the experiments performed with UV-Vis spectrometry, circular dichroism spectroscopy, isothermal titration calorimetry, and confocal laser scanning microscopy are reported.

In chapter 3, in attempts to explore the biofunctions of RNA G4s in cancer cells, the anticancer mechanism after the treatment of ligand are analyzed. A series of cellular based assays including RNA expression, proteins expression, cell cycle analysis, apoptosis study, and immunofluorescence were applied for the study. These studies may provide understanding and experimental evidence on how the mRNA G4-selective ligand induce anticancer effects by targeting *NRAS* mRNA G4s in cancer cells.

1.7. Objective of the project

The primary objective of the present study is to develop novel fluorescent mRNA G4-selective small molecules as a chemical tool to understand and investigate the biofunction of RNA G4-structure, particularly *NRAS* mRNA G4s, in human cancer cells.

Chapter 2. Discovery of small-sized ligands targeting RNA G-quadruplexes

2.1. Synopsis

The G-rich RNA sequences are possibly folded into G4-structures and each sequence may form a unique G-quadruplex structure depending on the sequence of nucleotides, length of the loops, and the number of stackings of G-quartet. To have a better understanding on the structural property of RNA G4s and their *in vitro* and intracellular interactions with G4 ligands, we have designed and synthesized a series of novel RNA G4-ligands for investigations. Several *in vitro* and cellular bioassays were performed to study the RNA G4-target selectivity, cellular localization of the ligand in live human cells, and their cytotoxicity against a panel of cancer cells.

2.1. Rational design of RNA G-quadruplexes ligands

In the design of G4-ligands, the benzothiazole was adopted as the basic molecular scaffold for structural modification because this small scaffold is commonly reported for designing G4-DNA selective ligands. In addition, Thioflavin T (ThT) and Thiazole Orange (TO) are the fluorescent ligands with similar structures and are well-known binding to G4s with good enhanced fluorescence signal upon interaction despite these ligands are not selectively targeting G4s.[71-73] In particular, the ligand TO binds double-stranded DNA with a high affinity and is usually used as a nucleic acids stain. Interestingly, both ThT and TO share the same benzothiazole moisty, which have been demonstrated as a useful scaffold for G4-DNA ligand interaction, probably due to the similar size and shape of molecular structure of benzothiazole and guanine.[74] Furthermore, many studies have revealed that benzothiazole-based ligands may exhibit excellent selectivity toward some G4-forming sequences (Figure 2.1).[74-77] More importantly, the moiety of benzothiazole could also be readily modified to couple with other planar conjugated molecular unit via a methylene or ethylene bridge. This rotatable design can provide the ligand a degree of flexibility to match with the rigid G4-binding pocket. In addition, an aromatic planar system can be extended

through the rotatable and conjugated bond, which allow the induction of fluorescence response (a fluorescence turn-on switch) upon interactions between ligand and G4s. The enhanced fluorescence response provides a convenient and sensitive mean to study the interaction between the ligand and G4s in live cells with confocal imaging techniques.

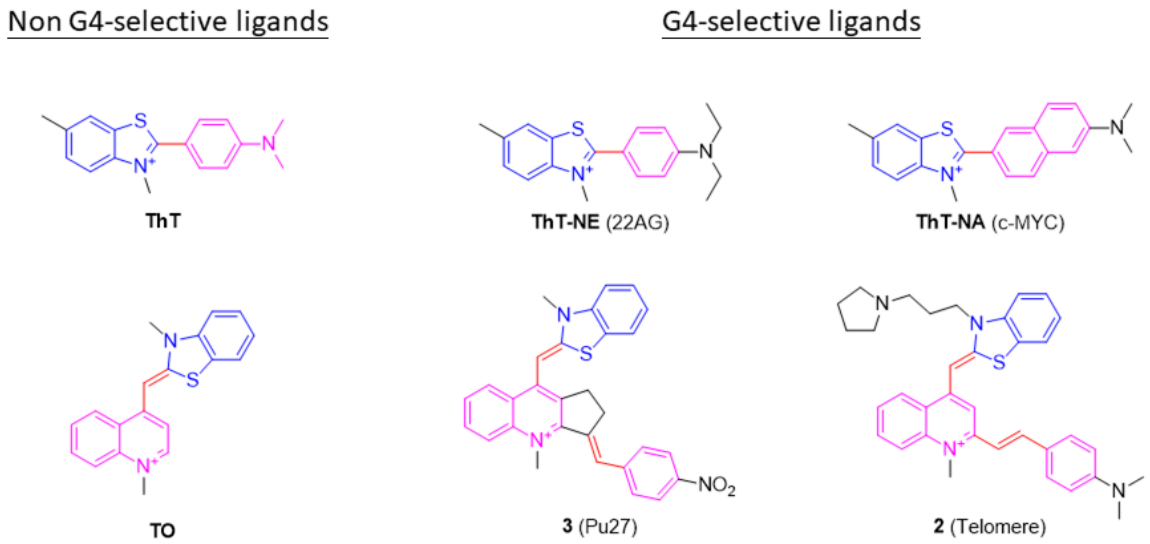

Figure 2.1. Diagrams showing the molecular structures of non G4-selective ligands ThT and TO, and the reported benzothiazole bearing G4-selective ligands. The colored scaffolds are used to discriminate different parts of component within the ligands, in which the benzothiazole moiety, rotatable bonding, and the extended aromatic system are represented in blue, red and violet, respectively.

In addition to the basic benzothiazole moiety, the use of other aromatic ring to form a larger conjugated planar system is critical to increase the G4-ligand π-π interaction. Various studies have demonstrated that the use of different aromatic ring groups can target G4-structure selectively.[23, 44, 59, 78, 79] To the best of our knowledge, only a few studies demonstrated a systemic structural modification to study the G4-ligands and their structural influence in the selectivity targeting G4s. There are still a lot of unknown on the design of G4-specific ligands. In the present study, we modified the benzothiazole moiety by extending its aromatic system with the aromatic ring of different size, locations and functional groups as shown in **Figure 2.2**.

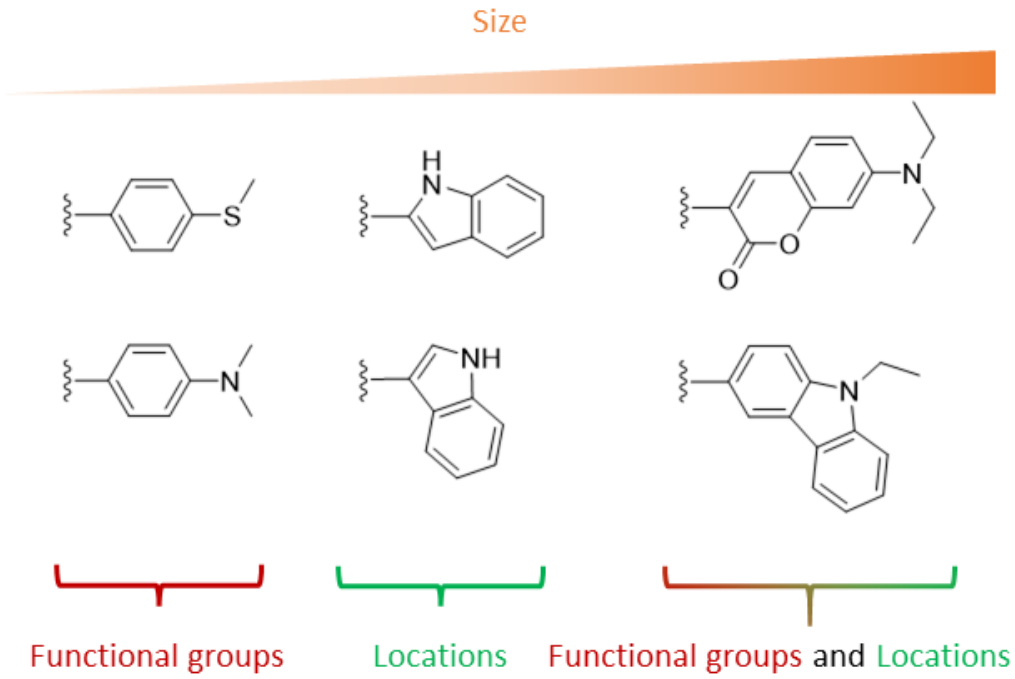

Figure 2.2. The selected aromatic rings conjugated to the benzothiazole moiety based on the size, functional groups, and the locations.

In attempts to target RNA G-quadruplexes with small molecules, it is important to consider the key difference between RNA and DNA. Apart from the difference of two unique nucleotides, Uracil (U) replacing Thymine (T), between RNA and DNA, the most significant difference is the 2'-OH group on the ribose group in RNA (Figure 2.3a and 2.3b). These 2'-OH groups are important in terms of stability of RNA G4 as it may provide an additional intramolecular interaction with ribose group, phosphate group, and nitrogen atoms in guanines of the G-quartet for a ordered G4-structure.[14] By comparing the 2'-H in DNA and 2'-OH in RNA, the 2'-OH may result in the RNA G4s being more polar than DNA G4s in nature. Therefore, the RNA G4 ligands designed with a relatively high polarity may benefit from the nature of RNA G4s to achieve better selectivity and affinity because it is supposed to follow the general rules of like-dissolve-like principle.

In the present study, we attended to design and modify the ligands by adding a side chain bearing either a polar functional group or a negative charge onto the nitrogen atom of benzothiazole (Figure

2.3c). The polar terminal group including hydroxyl group, carboxamide group and carboxyl group were selected for the synthesis and totally 18 new ligands were synthesized for investigation. In addition to the polarity, the carboxyl group is generally in the form of carboxylate ion under physiological conditions (pH 7.4). This special design of the ligand allows the study of the interaction between the ligand bearing a negative charged functional group and the negatively charged nucleic acid.

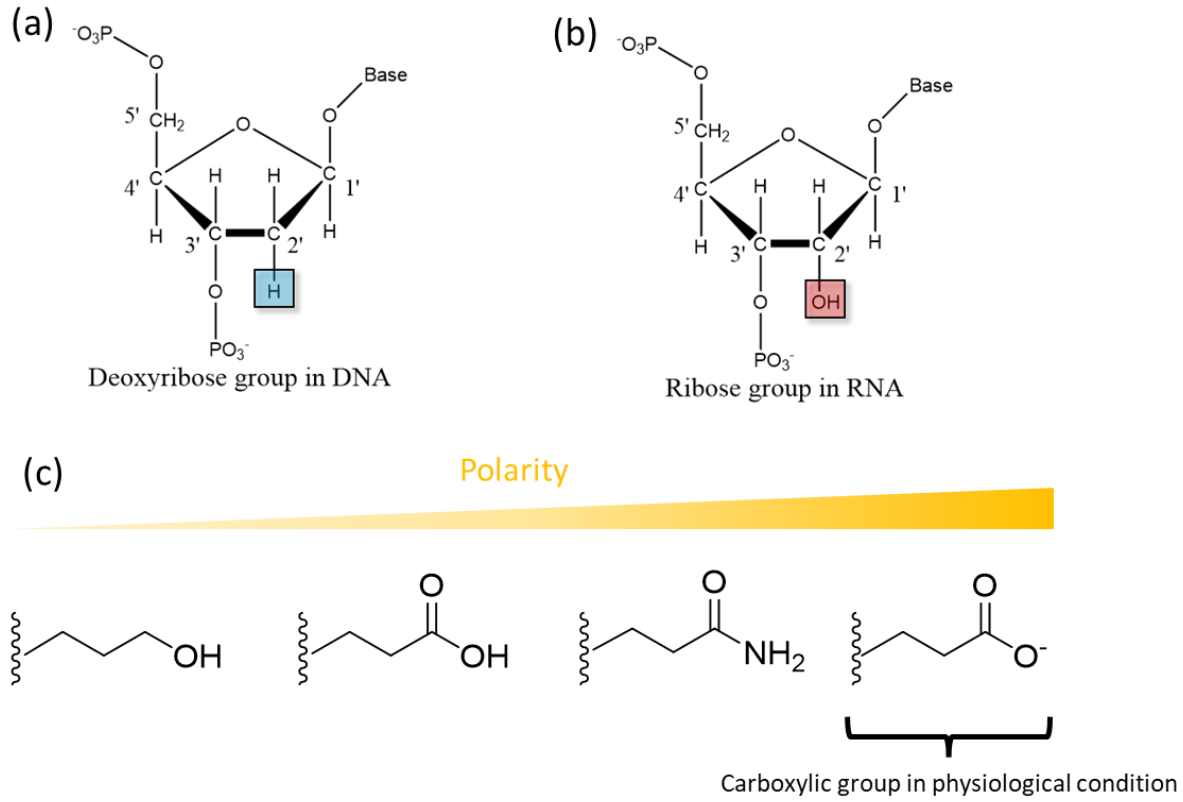

Figure 2.3. Diagram showing (a) deoxyribose group in DNA, (b) ribose group in RNA, and (c) the three side chains introduced on the ligands.

2.2. Result and discussion

2.2.1. Synthesis and characterization of G4-ligands

The general synthetic procedure to the ligands was described in Chapter 4, Section 4.2.1 and 4.2.2. The synthetic routes and molecular structures of the target ligands were shown in Figure 2.4 and Table 2.1. All ligands obtained were characterized with HRMS, ^{1}H NMR, and ^{13}C NMR. The detailed characterizations for the ligands were given in the section of Appendix.

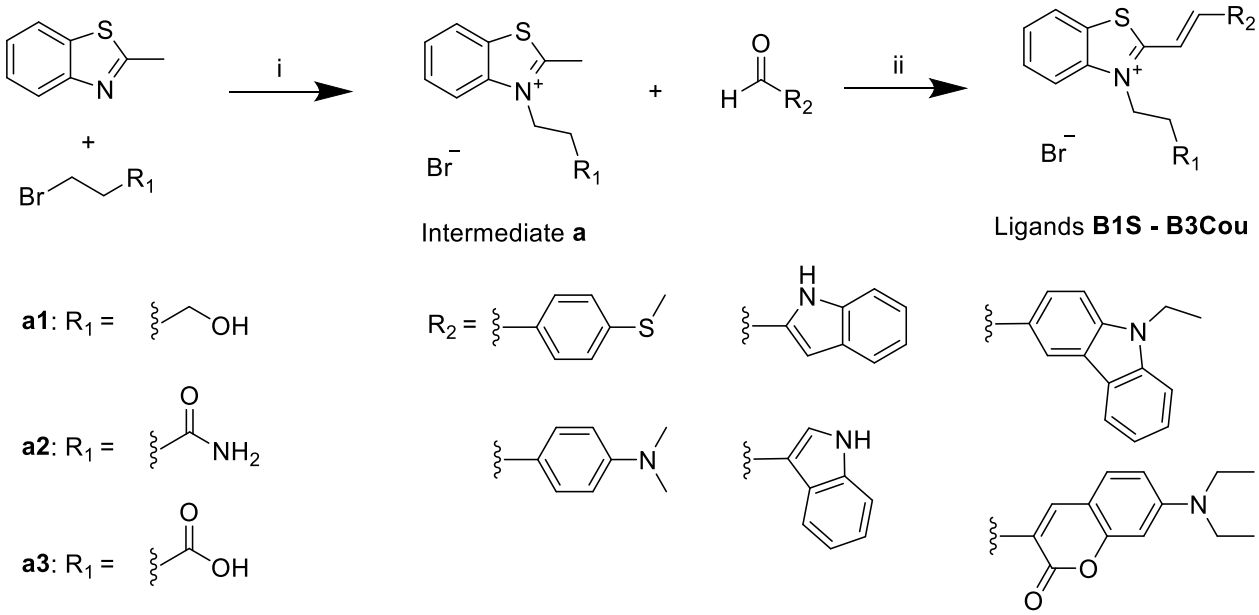

Figure 2.4. The synthetic route of (i) reaction of 2-methylbenzothiazole and 3-bromopropanol (or 3-bromopropionamide or 3-bromopropionic acid) in acetonitrile in pressure vessel at 110 °C under stirring condition for 24-48 hours; extraction of crude product in H_2O with ethyl acetate to obtain intermediate **a** with 60-80% yield. (ii) reaction of intermediate **a1** (or **a2** or **a3**) and corresponding aromatic aldehyde with potassium carbonate as a base in 1-butanol at 100 °C for 5 hours; after filtration, purification of product by flash silica gel column chromatography to obtain ligand **B1S** to **B3Cou** with 60-90% yield.

Table 2.1. Molecular structures of the new G4-ligands synthesized in the present study

Aromatic ring, R_2	Side chain, R_1		
	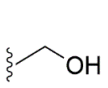	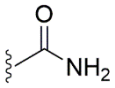	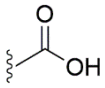
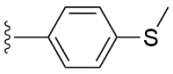	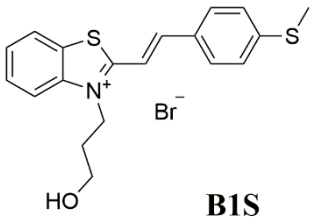 **B1S**	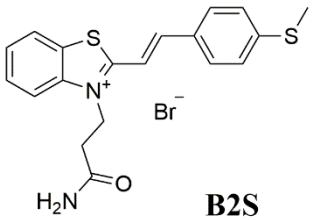 **B2S**	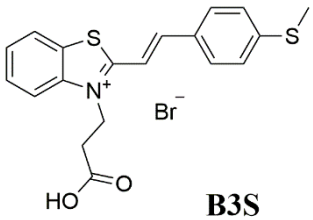 **B3S**
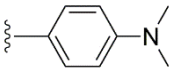	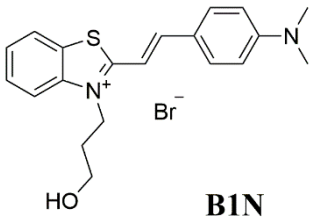 **B1N**	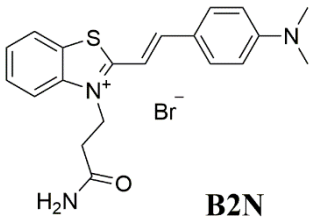 **B2N**	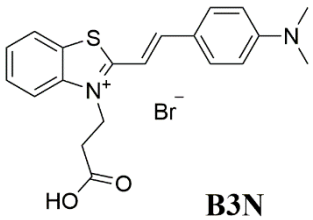 **B3N**
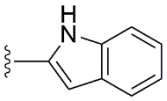	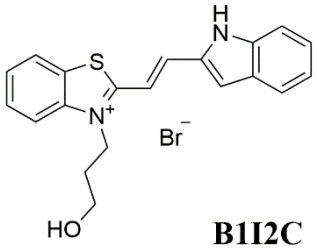 **B1I2C**	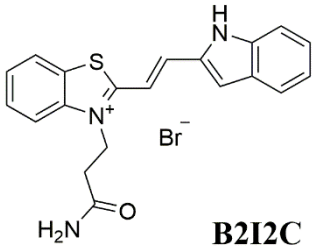 **B2I2C**	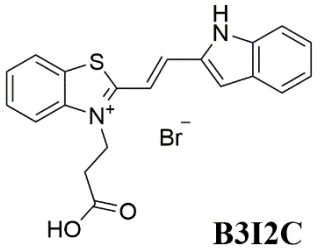 **B3I2C**
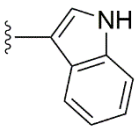	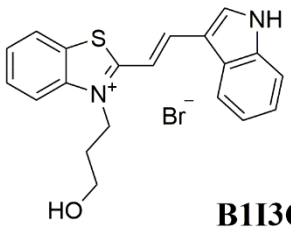 **B1I3C**	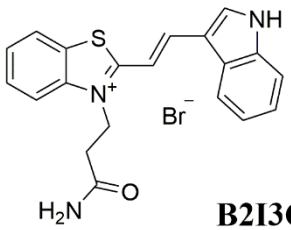 **B2I3C**	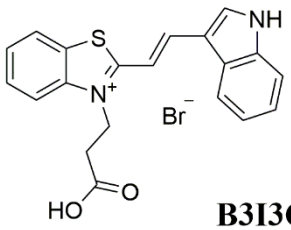 **B3I3C**
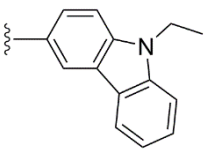	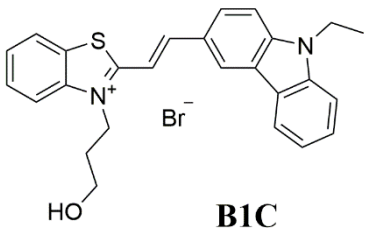 **B1C**	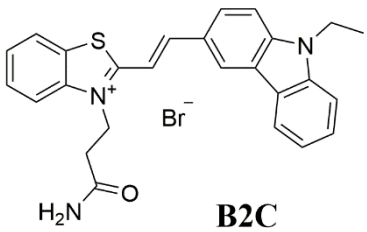 **B2C**	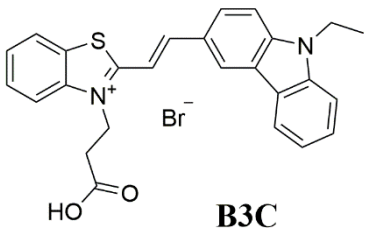 **B3C**
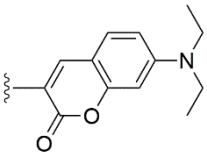	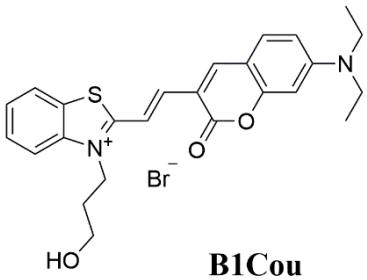 **B1Cou**	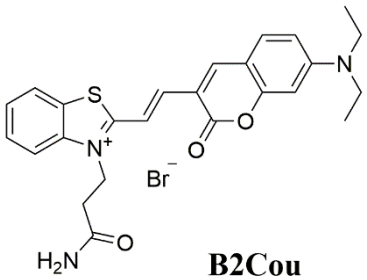 **B2Cou**	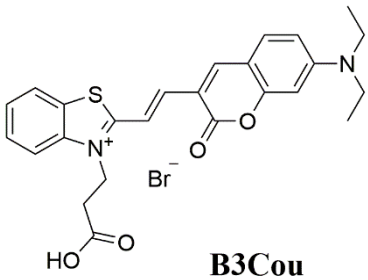 **B3Cou**

2.2.2. Screening of ligands selective to RNA G-quadruplexes and cytotoxicity evaluation

Fluorescence spectroscopy is a convenient and sensitive method to investigate the interaction between ligands and nucleic acids *in vitro* and cellularly. Attributed to the special structural design in which two aromatic rings are connected by the double bond, an enhanced fluorescent response can be measured upon the ligand interacted with the nucleic acid substrates in the solution for the study of G4-ligand interactions. This enhanced fluorescence signal can be explained by the restriction of the free rotation of the ligands.[71, 80, 81] In a solution state, the ligand rotates freely through the methylene bridge. These motions enhance the non-radiative deactivation of excited states of the ligand. Thus, the fluorescence of the ligands is weak. Upon the addition of nucleic acids, the ligand binds to the substrate. The interaction limits the free rotation of the ligand, and thus the non-radiative deactivation pathway is significantly reduced which enhances the fluorescence of the ligand. As the enhanced fluorescence signal is correlated with the interaction of the substrate and the ligand, it may possibly provide a convenient way to compare the binding selectivity of ligands toward different nucleic acids under the same titration conditions. In the present study, several DNA-G4 sequences (Telomere related: *Telo21* and *22AG*; oncogene related: *c-KIT* and *Pu27*), RNA-G4 sequences (Telomere related: *TERRA* and *TRF2*; oncogene related: *NRAS*, *KRAS*, and *VEGF*), non-G4 DNA sequences (dsDNA and Da21), and non-G4 RNA sequences (hairpin RNA) were selected as the model substrates to investigate the selectivity of the new ligands.

To facilitate a quick screening of 18 ligands toward various nucleic acid sequences, the concentration of nucleic acid at 100-equivalent of the ligand was used for the *in vitro* interaction study in buffer. The results were shown in Figure 2.5. From fluorescence titration results, six ligands which include **B1I3C**, **B2I3C**, **B3I3C**, **B1C**, **B2C** and **B3C** were found showing a higher selectivity toward RNA G4s than DNA G4s. Comparing the titration results, we also observed that **B3I3C** with a terminal carboxylic group enhanced the selectivity toward RNA G4s over DNA.

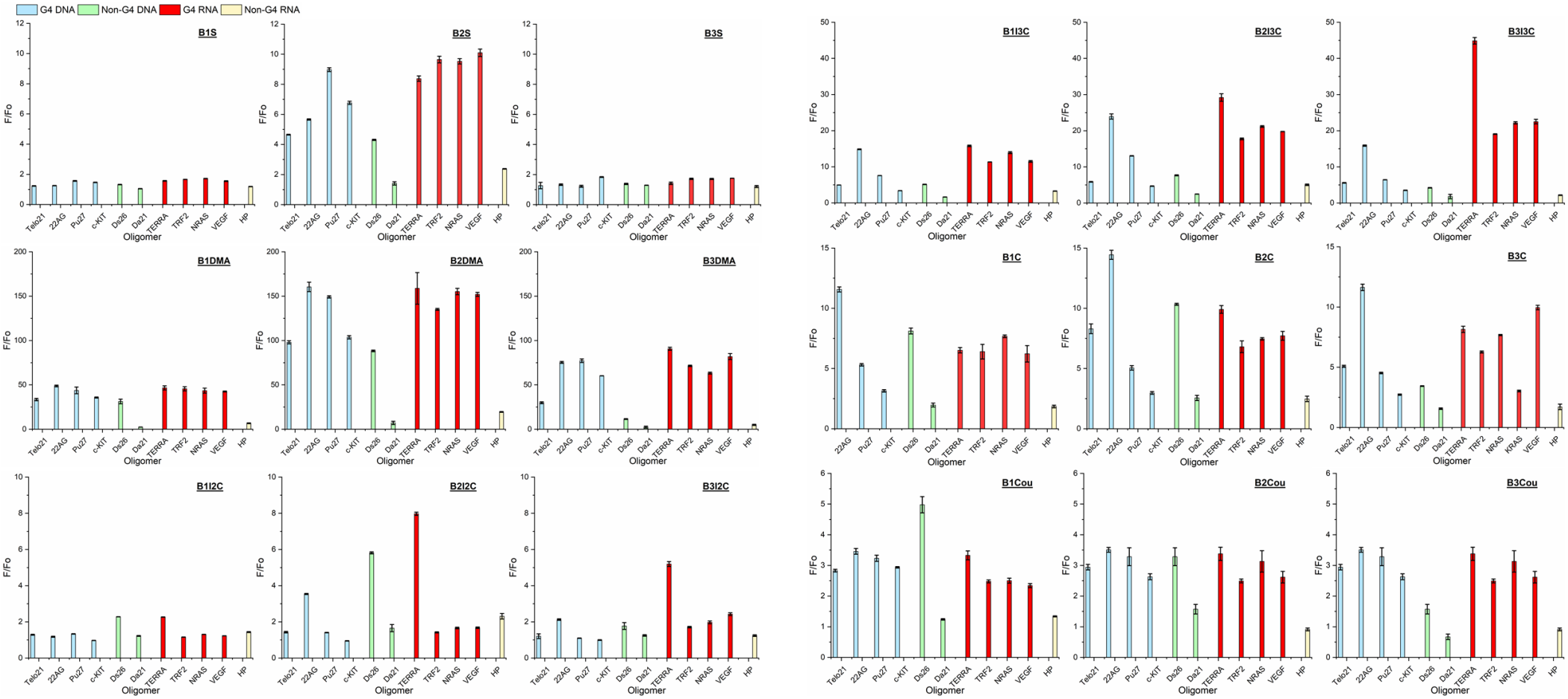

Figure 2.5. The enhanced fluorescent response of ligands upon addition of 100-folds of different DNA and RNA substrate.

In addition, we found that the introduction of a terminal carboxyl group at the side chain of the ligand generally showed a much weaker fluorescent response toward double-stranded DNA(dsDNA) as compared with G4s. The results may indicate that dsDNA have a weaker ability to restrict the free rotation of the ligand compared to that of RNA G4s under the same conditions, which may be due to their weak ligand-dsDNA interaction. The reported study suggests that the design of G4-ligands should possess positive side chains to enhance the binding affinity with nucleic acids.[14] In the present study, we demonstrated that the introduction of negative charged functional group could be an alternative approach for designing G4-selective ligands against dsDNA. Furthermore, the ligands with a carboxamide group were found generally showing a higher induced fluorescent response toward both DNA and RNA G-quadruplexes sequences. This result could be possibly due to the additional hydrogen bonding interactions with nucleic acids and that effectively restricts the free rotation of the ligand. Taken together, for the ligands that are capable of interacting with both G4s and dsDNA, the introduction of a carboxylate at the terminal group could generally enhance the *in vitro* discrimination ability of the ligand toward RNA G4s from dsDNA.

Apart from the terminal group effects, the aromatic scaffold integrated with benzothiazole via an ethylene bridge also shows critical influence to the selectivity of the ligand toward RNA G4s. From ligand series of **B1I2C** and **B3I3C**, a significant increase in the enhanced fluorescent response was observed for RNA G4s when the integrated molecular scaffold varied from 2-methyl-1H-indole to 3-methyl-1H-indole. The results suggest that the I3C series may have a better stacking on the G-quadruplexes because it is structurally similar to G-quartet compared to its analogues of I2C series. By analyzing the results of enhanced fluorescent responses obtained from fluorescence titrations, we identified six ligands, including **B1I3C**, **B2I3C**, **B3I3C**, **B1C**, **B2C** and **B3C**, having a high potential to bind to RNA G4s with a relatively high selectivity because these ligands generally generated stronger interaction signal toward RNA G4s than DNA G4s. In addition, considering the discrimination ability of ligands against dsDNA which is the key intracellular competitor, four

ligands including **B1I3C**, **B2I3C**, **B3I3C** and **B3C** were selected for further investigations.

Targeting G4s to inhibit their corresponding protein expression may be able to affect cell functions and induce apoptosis eventually.[3, 82, 83] We then performed cell-based 3-(4,5-dimethylthiazol-2-yl)-2,5-diphenyltetrazolium bromide (MTT) assays to evaluate the cytotoxicity of the RNA G4-targeting ligands screened. MTT assay is a colorimetric assay for evaluating the cell metabolic activity. Upon the addition of MTT, the NAD(P)H-dependent cellular oxidoreductase enzyme will reduce the MTT dye to the insoluble formazan. As only live cells contain active NAD(P)H-dependent cellular oxidoreductase enzyme, the number of formations of formazan is then proportional to the number of live cells, which can be used for assessing the half maximal inhibitory concentration (IC50). Among the 18 new ligands, for the carbazole series ligands, **B1C**, **B2C** and **B3C**, they were found having the IC50 at around 6.5-8.1 μM against human cervix cancer HeLa cell lines. More importantly, the IC50 of these three ligands against the non-cancer human fibroblast cell line (HFF1) were found greater than 50 μM (Figure 2.6 and Table 2.2). The results may indicate certain degree of cytotoxic selectivity of the ligands. It is reported that G4s generally are abundance in oncogenes in cancer cells compared to normal cells.[15] The results of the cell-based MTT assay imply that the ligand may possibly interact and stabilize the RNA G4s of certain oncogenes. Thus, the expression of the corresponding proteins may be inhibited or disrupted by the G4-ligand and that may cause cell death. By analyzing the MTT results and the ligand selectivity toward RNA G4s, ligand **B3C** was found generally exhibiting good performance and thus was selected for further investigations in live cells.

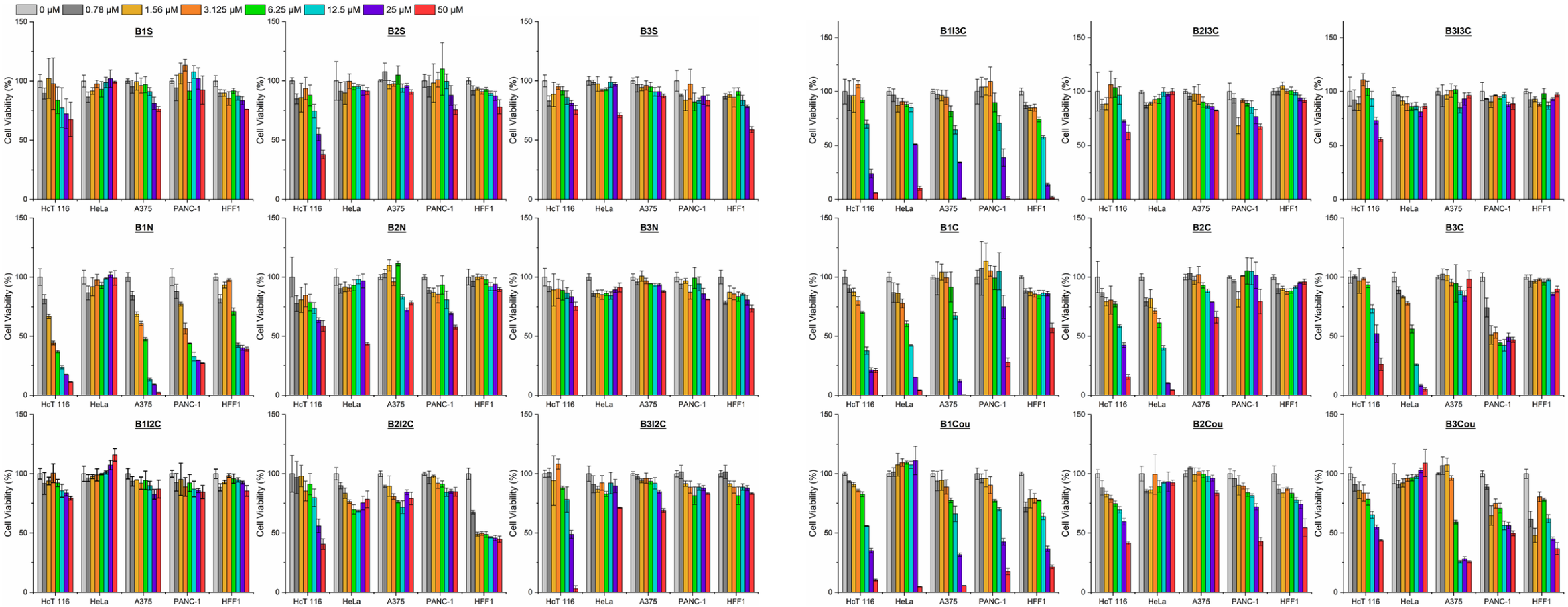

Figure 2.6. The cytotoxicity of eighteen ligands to different cancer cells and normal cell line, which were measured by MTT assay.

Table 2.2. Evaluation of the cytotoxicity (μM) of new compounds synthesized against human cancer cells and noncancerous cells with MTT assays.

Ligands	Cell lines				
	HcT 116	HeLa	A375	PANC-1	HFF1
B1S	>50	>50	>50	>50	>50
B2S	32.9 ± 4.5	>50	>50	>50	>50
B3S	>50	>50	>50	>50	>50
B1N	3.5 ± 0.2	>50	4.1 ± 0.6	5.6 ± 0.8	17.7 ± 2.4
B2N	>50	47.6 ± 1.9	>50	>50	>50
B3N	>50	>50	>50	>50	>50
B1I2C	>50	>50	>50	>50	>50
B2I2C	35.1 ± 4.7	>50	>50	>50	9.4 ± 2.7
B3I2C	22.2 ± 1.7	>50	>50	>50	>50
B1I3C	16.8 ± 1.0	24.3 ± 1.2	16.1 ± 0.7	18.9 ± 1.3	11.5 ± 0.9
B2I3C	>50	>50	>50	>50	>50
B3I3C	>50	>50	>50	>50	>50
B1C	9.9 ± 0.7	8.1 ± 0.61	15.0 ± 0.6	36.6 ± 2.9	>50
B2C	15.3 ± 1.9	6.8 ± 0.6	>50	>50	>50
B3C	25.9 ± 1.4	6.5 ± 0.3	>50	>50	>50
B1Cou	15.0 ± 0.9	44.5 ± n.d.	15.5 ± 1.0	19.3 ± 1.2	15.9 ± 3.2
B2Cou	40.4 ± 5.2	>50	>50	49.5 ± 6.1	>50
B3Cou	34.7 ± 3.5	>50	9.6 ± 1.0	38.8 ± 9.3	28.2 ± 15.9

2.2.3. Live cell imaging of the ligand targeting RNA G4s

In attempts to investigate RNA G-quadruplexes in live cells, the cellular localization of the ligand is critically important as most RNAs are in cytoplasm. We therefore performed live cell imaging for the ligand with confocal microscopic techniques to study the cellular location of the ligand after entering the cells. In the previous sections, our experimental results demonstrate that **B3C** shows high preference to interact with RNA G4s *in vitro* and generate strong fluorescence signal. From the live cell confocal image shown in Figure 2.7a the fluorescent foci of **B3C** were mostly located in cytoplasm while almost no fluorescent foci could be found in the nucleus of the cells. The results support that the ligand is not targeting nucleus. To illustrate **B3C** are actually localized in cytoplasm, immunofluorescent colocalization of lysosome associated membrane protein 1(LAMP-1) with **B3C** in cells was conducted. From Figure 2.7b, green fluorescent foci (**B3C**) and red fluorescent foci (LAMP-1) were found localized in a similar region and showed some colocalizations. The immunofluorescence colocalization study supports that both **B3C** and LAMP-1 in cells may have the same or similar location, which is presumably the cytoplasm .Mitochondria are the organelles located in cytoplasm and also contain DNA-G4s and RNA-G4s.[16, 17] In addition, a high potential different between the mitochondrial matrix (-220 eV) and cytoplasm may render the positively charged ligand entering the mitochondria easily.[18] We therefore investigated whether **B3C** entered and localized in mitochondria. In the live cell imaging experiments, **B3C** was co-stained with MitoTracker Deep Red in HeLa cells. As shown in Figure 2.7b, it was found that there was no observable colocalization between **B3C** and MitoTracker Deep Red. The results support that mitochondria are also not the cellular target of **B3C** and therefore the ligand may be most likely localized in cytoplasm and interacts with the cytoplasmic RNA-G4 to generate strong fluorescence.

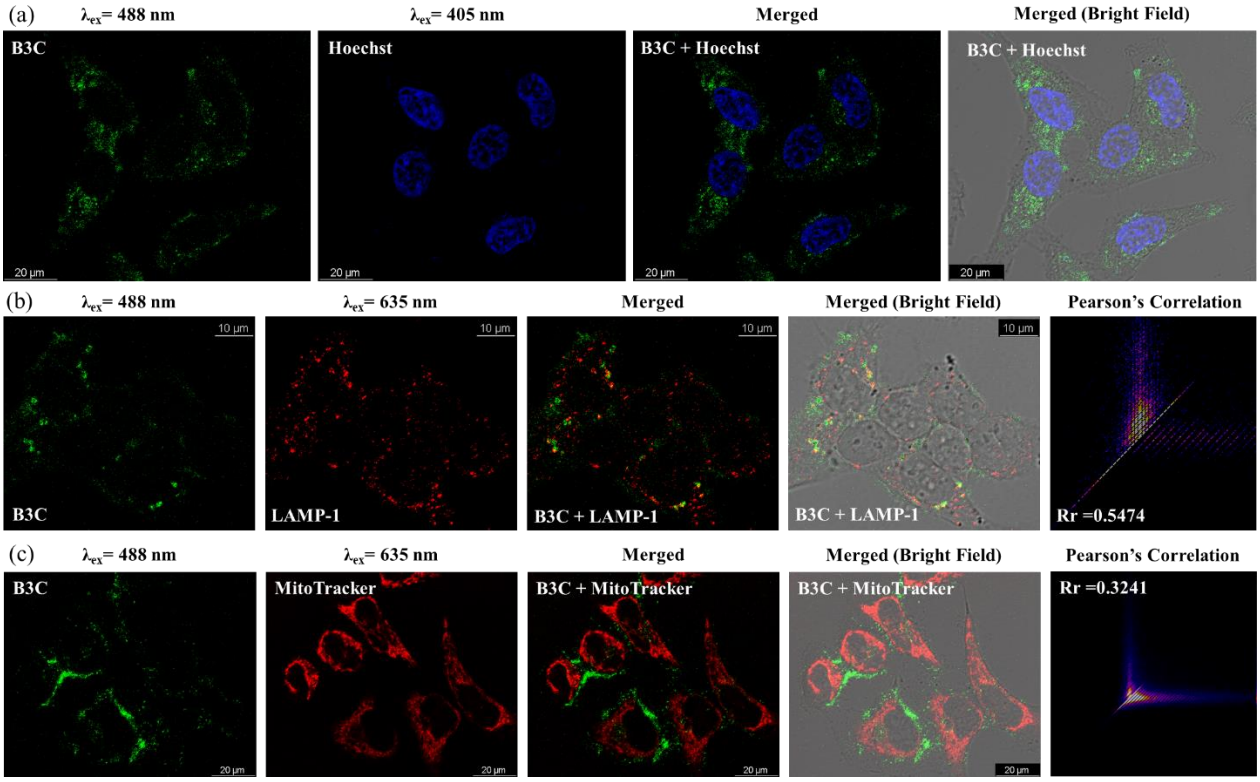

Figure 2.7. (a) Confocal images of live HeLa cells co-stained with 5 μM **B3C** and 2 μM Hoechst (b) Immunofluorescent images of fixed HeLa cells colocalized of **B3C** (5 μM) and lysosome-associated membrane protein-1, LAMP-1, to demonstrate that **B3C** localize in cytoplasm. (c) Confocal images of live HeLa cells co-stained with 5 μM **B3C** and 20 nM Mito-tracker DeepRed.

2.2.4. The study of **B3C**-nucleic acid interaction *in vitro*

To investigate the interaction of **B3C** with different nucleic acids, the photophysical properties of ligands upon the addition of nucleic acids were measured and analyzed. We first performed ultraviolet-visible (UV-vis) spectrophotometric titrations to study the binding mode of **B3C**. The result of UV-vis titrations of **B3C** toward different nucleic acids were shown in Figure 2.8a and 2.8b. The result shows that there is a decrease in absorption of **B3C** and a red shift of peak when RNA G4s and DNA G4s are added into the buffer solution containing **B3C**. The appearance of red shift may possibly be due to the enlargement of conjugate system of **B3C**.[84] Thus, the energy gap of π to π* is reduced and a peak appears at a higher wavelength region (520 nm). It indicates that **B3C** may bind to the planar G-quartet of the G4-structure through π-π stacking interactions. Among all the G4 sequences examined, we observed that there was only slightly or no red shift of **B3C** upon the addition of telo21 and 22AG. As the topology of telo21 and 22AG is hybrid (Figure

2.10b) in buffer solution with 60 mM K^+ ion, the result indicates that the **B3C** may not interact with hybrid or antiparallel G4s through π-π stacking with the G-quartet, which may be due to the steric diagonal loop. For RNA hairpin, dsDNA, and Da21, all these substrates only show a decrease in absorption which may indicate that **B3C** does not interact with them through π-π stacking. Taken together, the result of UV-vis titration suggests that the molecular design of **B3C** may render the ligand more favorable to interact with parallel G4s through the mode of π-π stacking interactions. Almost all RNA G4s are in the parallel topology[85] and that may possibly facilitate their interactions with **B3C**.

To investigated whether **B3C** induced the conformation change of the G4-structure upon interaction *in vitro*, circular dichroism (CD) measurements were performed. From the results shown in Figure 2.9a and 2.9b, the CD spectra show that there is an increase in both positive peak (264 nm) and negative peak (240 nm) of RNA G4 sequence after the addition of **B3C** in the buffer without K^+ ions. The result indicates that the folding of a parallel RNA G4-structure is increased after **B3C** interacting with the RNA G-rich sequences and also suggests that **B3C** may possibly induce the formation of RNA G4-structure *in vitro*.

Furthermore, we observed that there was very little or even no changes in the magnitude of peaks toward RNA hairpin, DNA G4 sequences, dsDNA, and Da21 after the addition of **B3C** in the same buffer condition. The results may imply that **B3C** can selectively induce the formation of RNA G4-structure. We then performed the same experiments in a 60 mM K^+ ions buffer to investigate the induced circular dichroism (ICD). ICD is the spectroscopic phenomenon for characterizing the structural changes and dynamic properties of the target biomolecules upon the addition of binding molecules. From the CD spectra from Figure 2.10a, no observable ICD was found on the RNA G4 sequences from 400 nm to 600 nm after the introduction of **B3C**. Under the same condition, there is also no significant ICD signal found for the DNA G4 sequences examined (Figure 2.10b). This suggest that **B3C** may not interact with the loop or flanking residues of the G4-structure. Taken

together with the result of UV-vis titration experiments, we found that the ligand **B3C** may induce G4s formation *in vitro* and bind to the G-quartet of the RNA G4-structure via π-π stacking interactions. The in-situ formed **B3C**-G4 complex is thus formed.

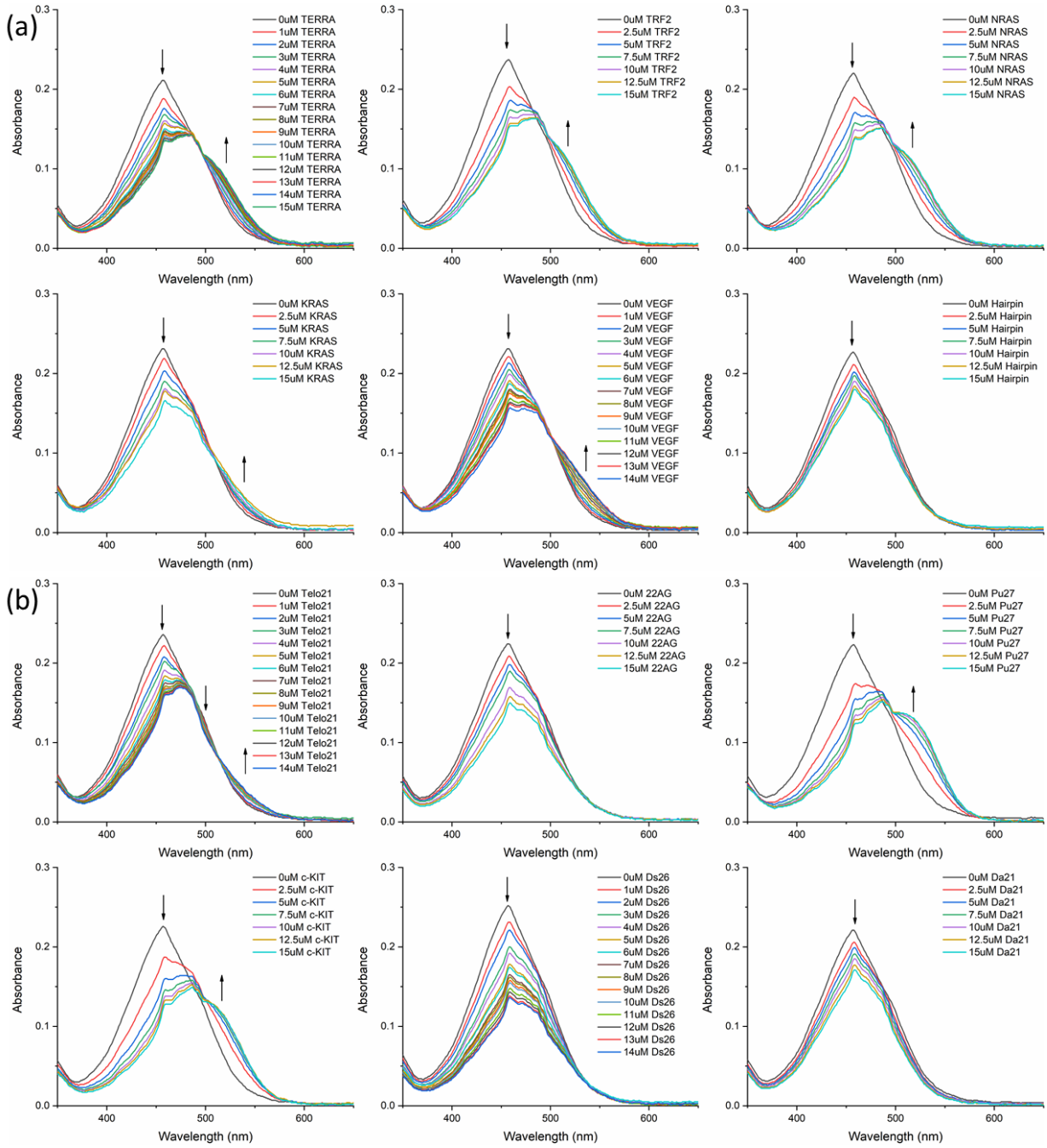

Figure 2.8. UV-vis spectra of **B3C** (5 μM) titrated with (a) RNA substrates, and (b) DNA substrates in a Tris-HCl buffer (10 mM, pH 7.4) containing 60 mM KCl.

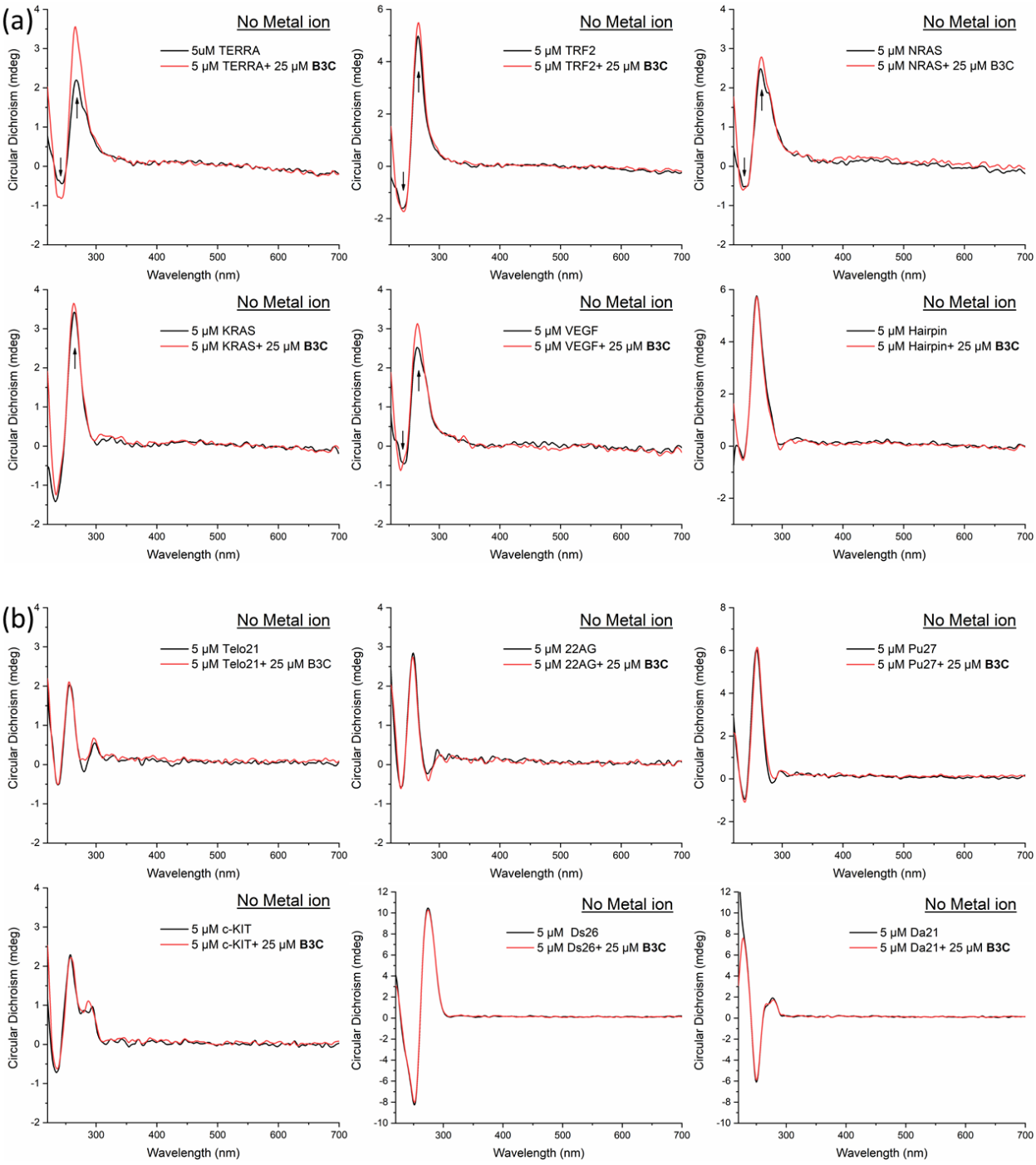

Figure 2.9. CD spectra of (a) RNA (5 μM) and (b) DNA (5 μM) substrates binding with or without the addition of **B3C** (25 μM) in a Tris-HCl buffer (10 mM, pH 7.4) without KCl.

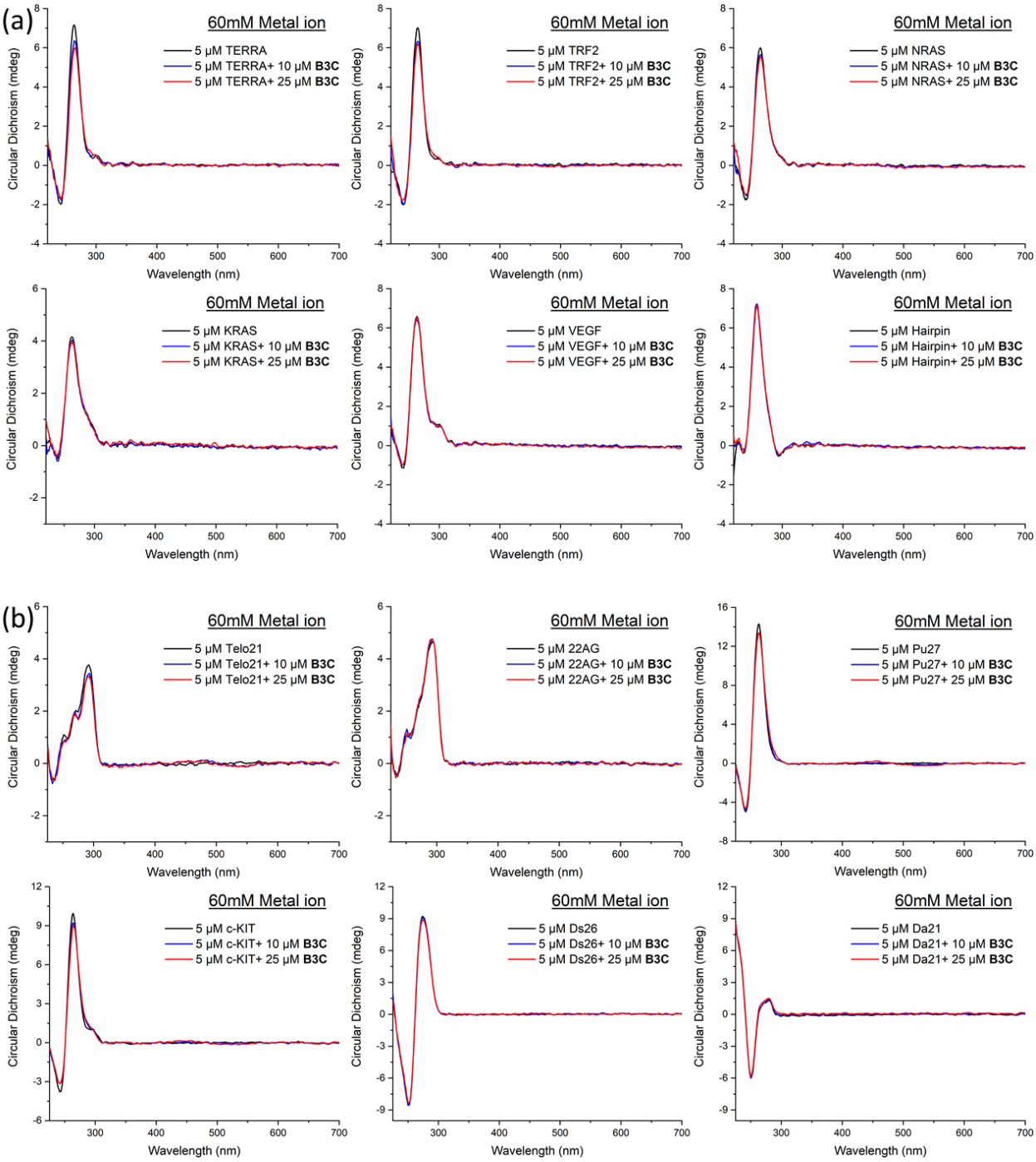

Figure 2.10. CD spectra of (a) RNA (5 μM) and (b) DNA (5 μM) substrates binding with or without the addition of **B3C** (10 and 25 μM) in a Tris-HCl buffer (10 mM, pH 7.4) containing 60 mM KCl.

To compare the stabilization ability of **B3C** toward different RNA and DNA sequences, CD melting experiments were carried out. The normalized CD melting curves of 5 μM RNA and DNA substrates before and after the addition of 25 μM **B3C** were shown in Figure 2.11. The results illustrate that **B3C** may stabilize most of the RNA and DNA G4-structures with an increase of melting temperature approximately from 0.4 to 8.6 °C and 0.2 to 5.5 °C, respectively. It is noteworthy to mention that the change in melting temperature (ΔTm) of dsDNA after the addition of **B3C** is very low. It may further suggest that the interaction between **B3C** and dsDNA is relatively weak. The results are found consistent with those observed from the fluorescence titration and CD experiments. Taken together, **B3C** may have a higher ability to stabilize the RNA G4s. To further confirm the stabilization ability of **B3C**, we performed an isothermal titration calorimetry (ITC) to determine the binding affinity of **B3C** toward different RNA G4s including *TERRA*, *TRF2*, *NRAS*, *KRAS* and *VEGF*. From the results of ITC assays (Figure 2.12), the estimated affinity (K_d) of **B3C** toward *TERRA*, *TRF2*, *NRAS* and *KRAS* were found to be 4.53, 8.75, 6.66 and 40.7 μM, respectively. For the K_d of **B3C** binding to VEGF, the thermal energy was too low to be detected by the instrument. Therefore, there was no binding determined for VEGF. Considering the result of ΔTm from CD melting curves and the binding affinity in terms of K_d obtained from ITC assays as shown in Table 2.3, a similar trend for both binding affinity and stabilization ability of the ligand was observed, which suggested that **B3C** could possibly interact with RNA G4s and also stabilize the complex formed *in vitro*. Based on the results obtained thus far, the ligand **B3C** appears to be a potential RNA G4-tageting ligand with good selectivity, particularly against the double-stranded DNA.

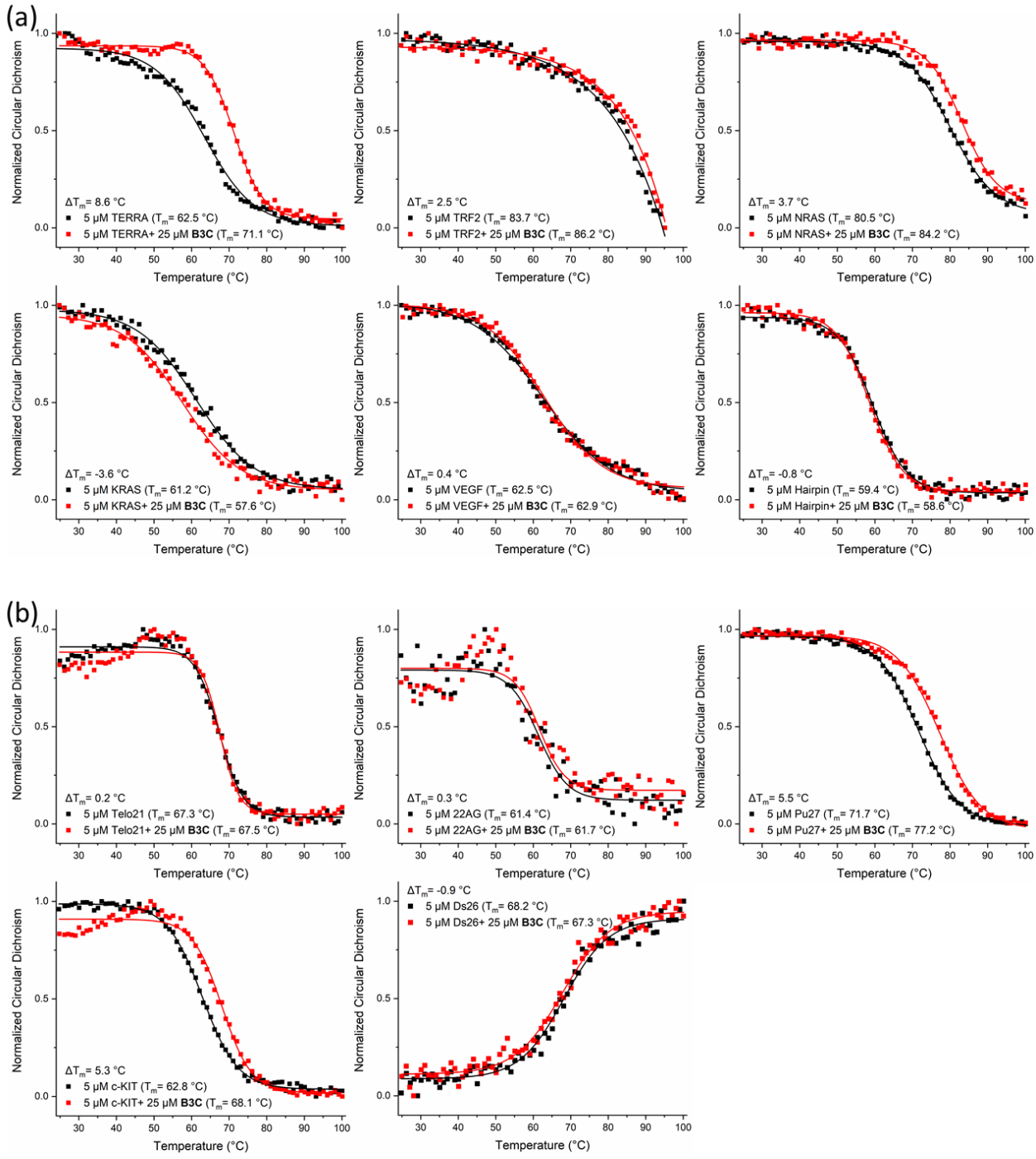

Figure 2.11. CD melting curves of (a) RNA (5 μM) and (b) DNA (5 μM) with or without the addition of **B3C** (25 μM) in a Tris-HCl buffer (10 mM, pH 7.4) containing 20 mM KCl.

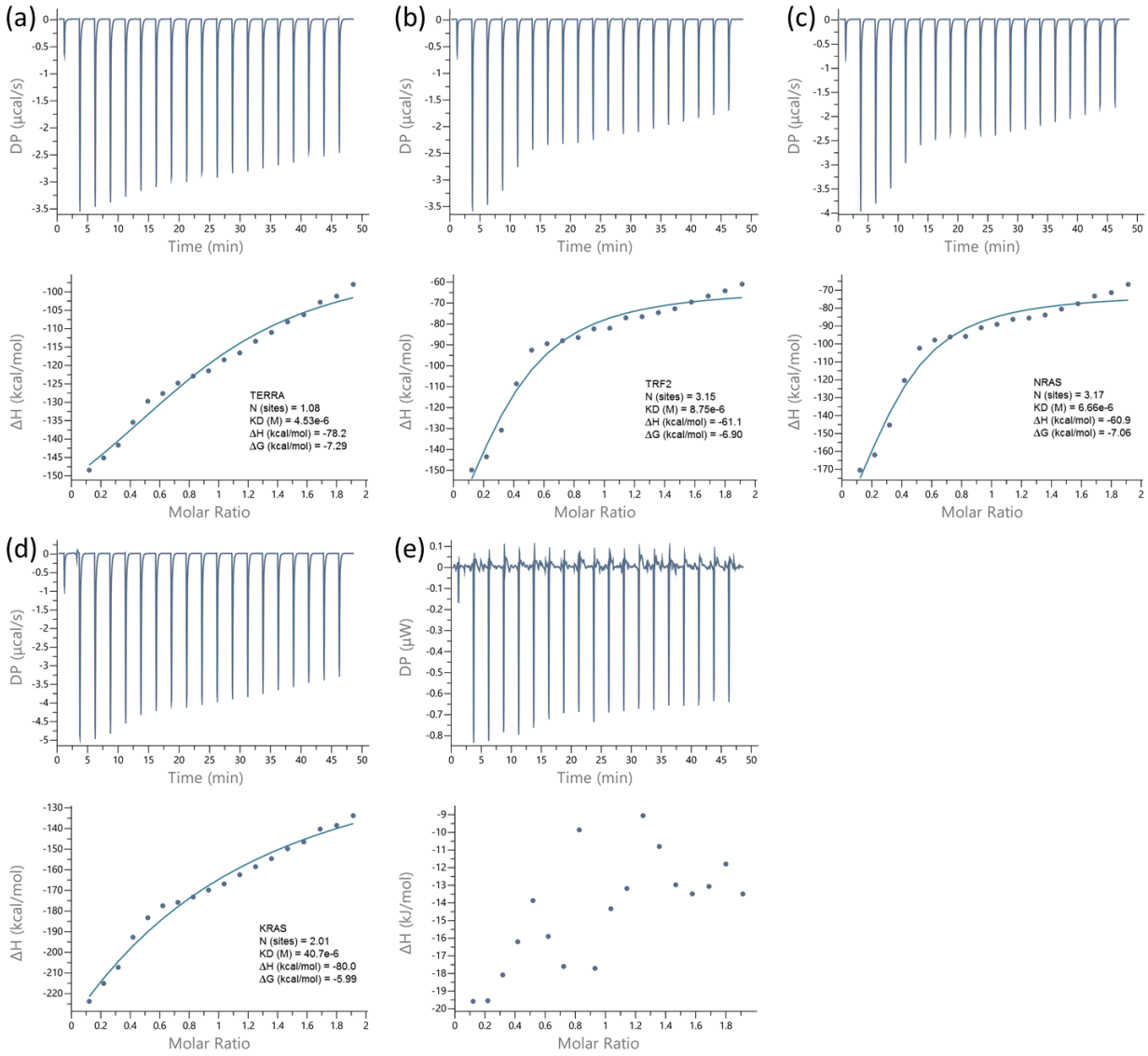

Figure 2.12. ITC assays for the study of **B3C** in KH_2PO_4 binding to (a) *TERRA*, (b) *TRF2*, (c) *NRAS*, (d) *KRAS*, and (e) *VEGF* in KH_2PO_4 buffer solution (25 mM, pH 7.4) containing 60 mM KCl. (Cell: 10 µM **B3C** in KH_2PO_4 buffer solution; titrant: 100 µM RNA substrates, both containing 0.1% DMSO).

Table 2.3. The value of ΔTm and K_d of binding of **B3C** to various RNA substrates.

RNA substrates	CD melting assay	ITC assay
	ΔTm (°C)	K_d (μM)
TERRA	8.8	4.53
TRF2	2.5	8.75
NRAS	3.7	6.66
KRAS	-3.6	40.7
VEGF	0.4	Not determined

2.2.5. The study of **B3C** interaction with intracellular RNA G4s in cells

To verify the cellular target of **B3C**, confocal microscope imaging of fixed HeLa was performed after the treatment of DNase and RNase. The result of enzymatic digestion assays was shown in Figure 2.13a to 2.13c. After the digestion of RNA by RNase, the fluorescent foci of **B3C** were almost completely disappeared (Figure 2.13c). On the contrary, the treatment of DNase did not affect the intensive fluorescent signal of **B3C** but the signal of the DNA stain, DAPI, was greatly reduced. This result revealed that DNA were digested. Therefore, the results of cell imaging suggest that the staining targets of **B3C** are possibly RNA and not DNA. We then performed another assay with confocal imaging to examine the intracellular targets stained with the ligand are most likely RNA G4s. In the assay, immunofluorescent colocalization of a G4-specific antibody, BG4,[86] with **B3C** in cells was conducted. From Figure 2.13d, several green fluorescent foci (**B3C**) and red fluorescent foci (BG4) were found well-colocalized. The overlapped foci were highlighted with arrows in the figure. The immunofluorescence colocalization study supports that both **B3C** and BG4 in cells may have the same or similar cellular target, which is presumably a G4-structure.

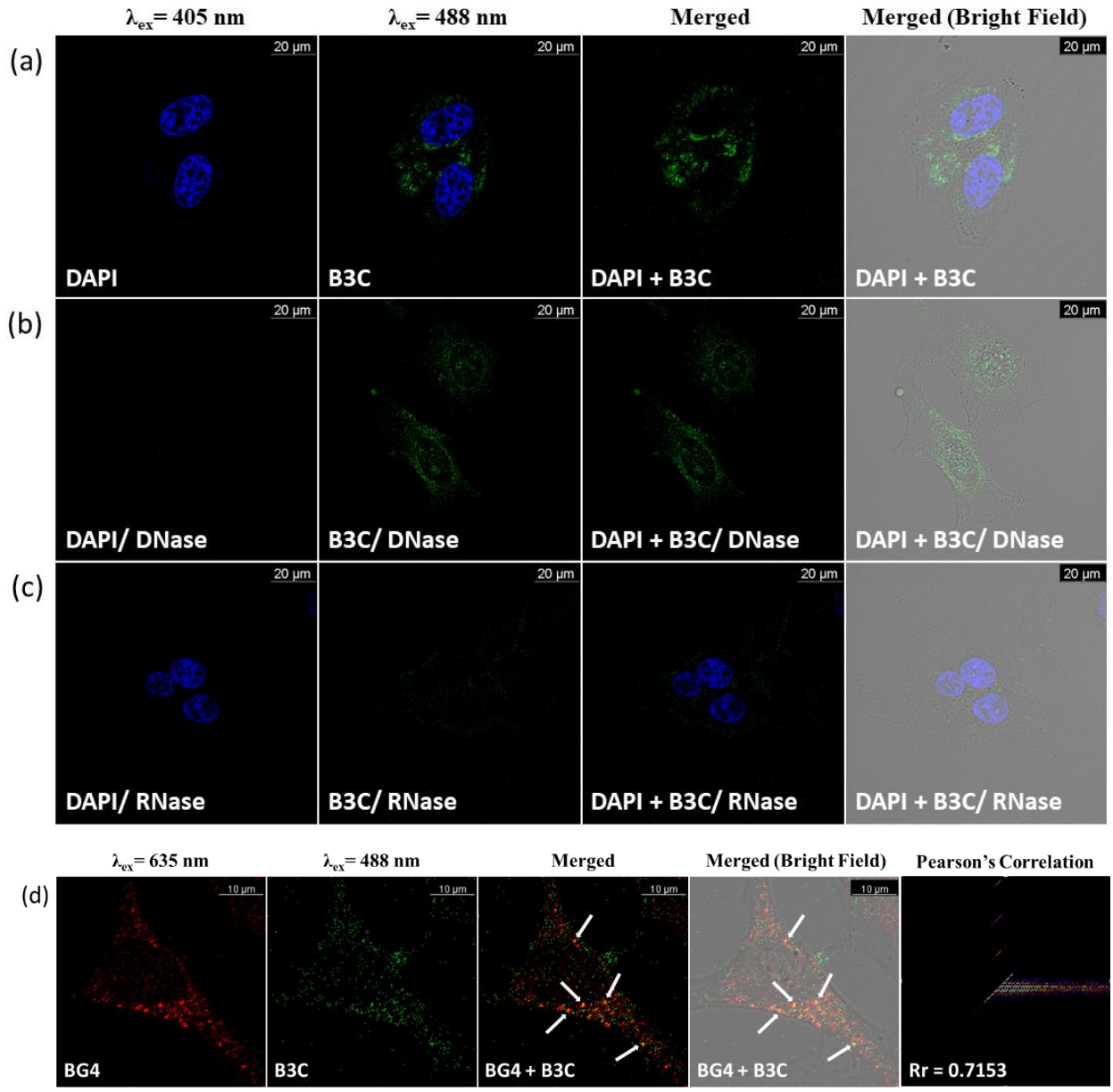

Figure 2.13. Confocal microscope fluorescent images of fixed HeLa cells co-stained with **B3C** (5 μM) and DAPI (2 μM) (a) without enzyme treatment, (b) with DNase I treatment, and (c) with RNase A treatment. (d) Confocal microscope fluorescent images of fixed HeLa cells colocalized of **B3C** (5 μM) and G4 specific antibody, BG4, in the immunofluorescence experiments.

2.3. Summary

In summary, eighteen new ligands were designed and synthesized for *in vitro* interaction investigations with various nucleic acid substrates. The ligands were evaluated for selectivity, cytotoxicity, and the cellular localization. The results revealed that ligands including **B1I3C, B2I3C, B3I3C,** and **B3C** showed a relatively high selectivity toward RNA G4 than DNA G4 and dsDNA. Among these ligands, **B3C** exhibited a low IC_{50} value, down to 6.5 against human cervix cancer HeLa and a relatively high IC_{50} value in non-cancer human cell line. The result may indicate that the ligand could possibly bind to target G-quadruplexes in cells. Live cell imaging of **B3C** also showed that the ligand mainly localized in cytoplasm instead of nucleus and mitochondria in live cells. Moreover, different *in vitro* experiments including UV-vis titration, CD melting study and ITC analysis revealed that **B3C** could interact with the G-quartet of the G4-structure and the ligand was demonstrated to be able to induce and stabilize the RNA G4-structure. In addition, the binding affinity (K_d) of the ligand toward the RNA G4s examined was found ranged from 4.53 to 40.7 μM. Furthermore, enzymatic digestion assays and BG4 co-localization assays showed that **B3C** possibly interacted with RNA G4s in cells. The results obtained thus far suggest that **B3C** may be a RNA G4-selective ligand and it inhibits cell proliferation effectively for a number of human cancers, particularly HeLa cancer cells. The anticancer mechanism was investigated, and the results were discussed in detail in Chapter 3.

Chapter 3. Study of anticancer mechanism of B3C

3.1. Synopsis

From the *in vitro* interaction and cellular imaging studies with the ligand targeting RNA G4-structure conducted in Chapter 3, **B3C** was found to be a potential RNA G4-selective ligand and capable to inhibit the proliferation of a panel of cancer cells. In attempt to investigate the anticancer mechanism of **B3C** targeting RNA G4s *in cellulo*, a series of experiments were carried out to study the response of the cells, such as the influence in the expression of DNA, RNA, and proteins, after the treatment of **B3C** in cancer cells.

3.2. Result and discussion

3.2.1. Study on the effect of gene and protein expression by **B3C**.

Targeting RNA G4s with small molecules to inhibit the corresponding protein expression is believed to be a promising strategy against oncogenic proteins. To directly access the impact of **B3C** on cellular processes, an evaluation of ability of **B3C** to modulate the transcription of different DNA to RNA in HeLa cells was first conducted. From previous studies shown in Chapter 2, it was found that **B3C** induced and stabilized the G4-structure of *TERRA*, *TRF2*, and *NRAS* with a binding affinity (K_d) of 4.53 to 8.75 μM. These results suggest that **B3C** may affect cellular functions of cells through targeting these oncogenic RNA G4-structures. Thus, the RNA level of *TERRA*, *TRF2*, and *NRAS* in HeLa cells were measured with qRT-PCR after the cells being cultured with 0, 5, 10, and 20 μM **B3C** for 48 h. As shown in Figure 3.1, only little changes of the mRNA level of *NRAS* was detected. This suggests that **B3C** may not affect transcription for expressing the *NRAS* mRNA from its corresponding DNA because the ligand is RNA-selective and thus it is less fovarable binding to DNA.

In addition, a significant increase in the mRNA level of *TERRA* and *TRF2* were found while **B3C** did not entery the nucleus to influence the DNA transcription. *TERRA* is a long non-coding RNA with G-rich repeating sequence of 5'-*d*(UUAGGG)-3' and is transcribed from telomeric DNA

sequences from multiple chromosome ends.[87-89] Recent studies have revealed that the binding of *TERRA* RNA to TRF2 proteins facilitates the heterochromatic foramtion to stabilize the DNA at telomere repeats.[90] It has also been reported that the mRNA level of *TERRA* and *TRF2* are upregulated upon DNA damage.[91-93] As both RNA levels of *TERRA* and *TRF2* were significantly upregulated in a concentration-dependent manner after the treatment with **B3C**, the results indicated that DNA damage was induced by the ligand in HeLa cells.

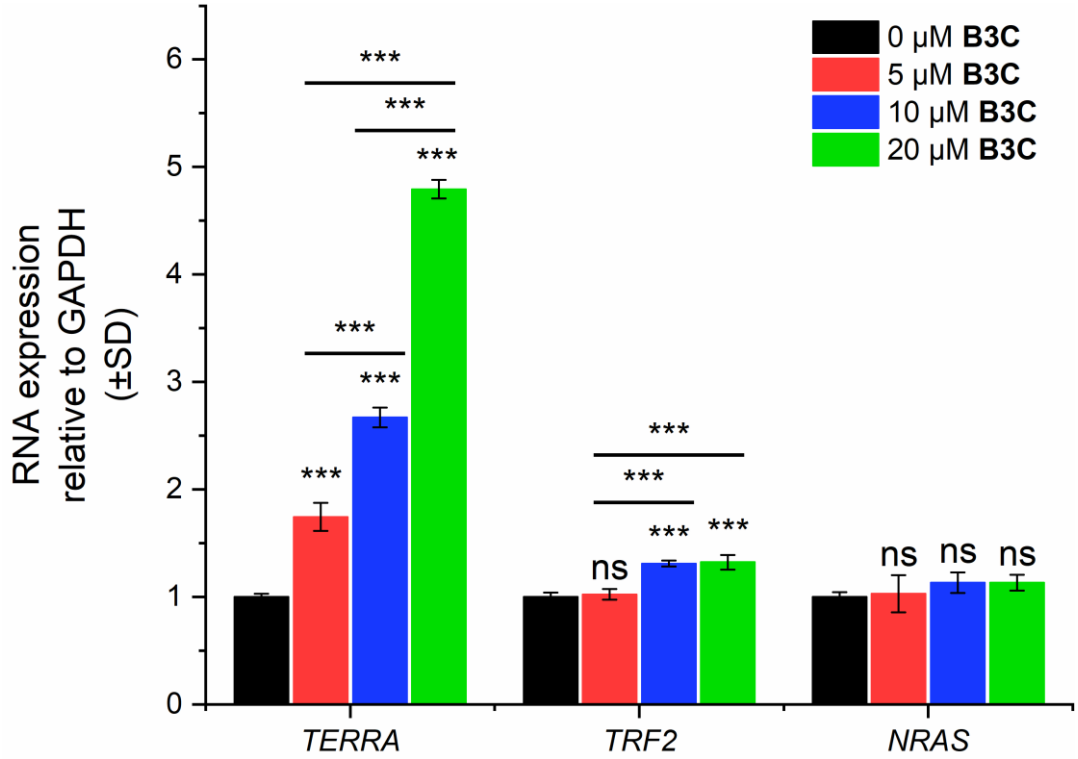

Figure 3.1. The relative transcription of *TERRA* RNA, *TRF2* mRNA and *NRAS* mRNA in HeLa cells treated with **B3C** (0, 5, 10, and 20 μM) for 48 h, and GAPDH was used as the endogenous control (N= 3, mean ± SD).

RNA G4s play a crucial role as translational repressor.[46, 94] Therefore, we further investigated the expression of proteins in HeLa cells by western blot asssays after the treatment with **B3C** for 48 h. It was observed that the the protein level of NRAS was significantly reduced in a dose-dependent manner (Figure 3.2). It indicates that the translation of NRAS is possibly repressed by **B3C** because the ligand is RNA G4-selective and shows strong interaction and stabilization ability toward *NRAS* mRNA G4-structure. Considering the all results obtained, we may conclude that **B3C**

could most likely interact with the *NRAS* mRNA G4s and stabilize the structure in cells and then inhibit the expression of NRAS protein via translational but not transcriptional pathway. On the contrary, the protein level of TRF2 only shows changes sightly upon the treatments of different concentration of **B3C**. It indicates that **B3C** may not repress the translation of TRF2 protein.

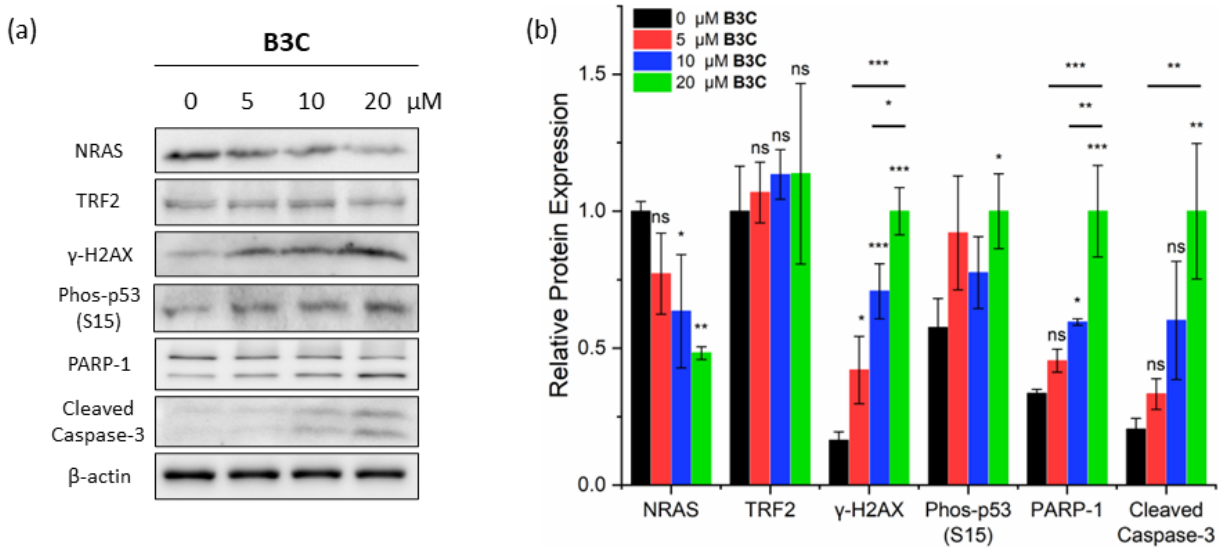

Figure 3.2. (a) Western blots assay to determine the translation of NRAS, TRF2, γ-H2AX, Phos-p53 (S15), PARP-1, Cleaved Caspase 3, and β-actin in HeLa cells treated with **B3C** (0, 5, 10 and 20 μM) for 48 h. (b) The relative proteins expression of HeLa cells after the treatments with **B3C** of different concentration (N =3, mean ± SD).

To better understand about the upregulation of the RNA of *TEERA* and *TRF2* observed from the qRT-PCR assays, we perforemed western blot again to determine the expression of γ-H2AX, a DNA damage marker for double-strand break (DSB).[95] It is because DNA damage could be a cause for upregulating the RNA of *TEERA* and *TRF2*. As shown in Figure 3.2, the expression of γ-H2AX is remarkably increased in a dose-dependent manner. When the HeLa cells were treated with 20 μM **B3C** for 48 h, a 5-fold increase in γ-H2AX is observed, which clearly supports that **B3C** induces DNA damage in HeLa cells.

From previous literature, studies reported that the treatment of small molecules in cells may trigger the formation of reactive oxygen species (ROS) which may damage the cellular DNA and also induce mitochondrial-related apoptosis.[96-98] To investigate the mechanism on the upregulation

of cellular γ-H2AX after the cells being treated with **B3C**, live cells imaging was performed to evaluate the level of cellular ROS. We first studied the ROS level inside mitochondria by MitoSOX Red. As shown in Figure 3.3, the red fluorescent signals are weak after the treatment with **B3C** at different concentration for 24 h. The cell imaging results indicate that **B3C** does not induce ROS production inside mitochondria.

We then further investigated the ROS level in the cytoplasm by using CellROX Deep Red reagent

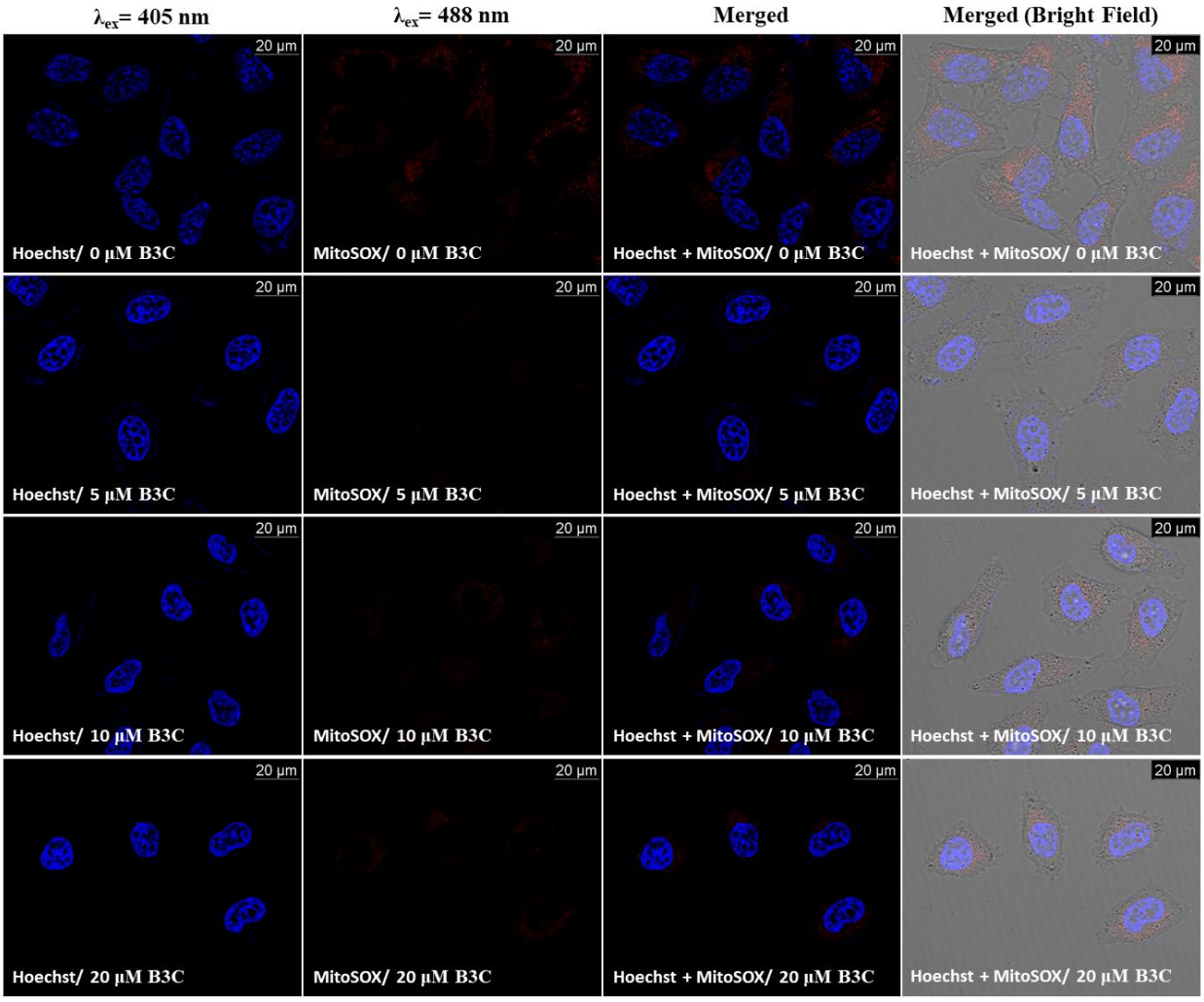

Figure 3.3. Confocal live cell imaging to investigate the ROS level in mitochondria with the use of MitoSOX after the treatment of **B3C** (0, 5, 10, and 20 μM) for 24 h.

with tert-butyl hydroperoxide (TBHP) as positive control. The live cell imaging results (Figure 3.4) show that the red fluorescence is marginal weak when comparing to the fluorescent signal from TBHP. The results from two ROS staining assays suggest that the treatment with **B3C** in HeLa cells may not trigger the formation of cellular ROS. In addition to the generation of ROS, we

performed the TMRE (tetramethylrhodamine, ethyl ester) staining assays to study the change on mitochondrial membrane potential. TMRE is a red-orange dye that accumulates in active mitochondria. TMRE cannot enter mitochondria if there is a change on the mitochondria membrane potential. Therefore, the fluorescent signal is reduced significantly. From the result shown in Figure 3.5, no significant change on the red fluorescent foci from TMRE were found after the treatment with **B3C** at different concentrations for 24 h, indicated that the mitochondria membrane potential

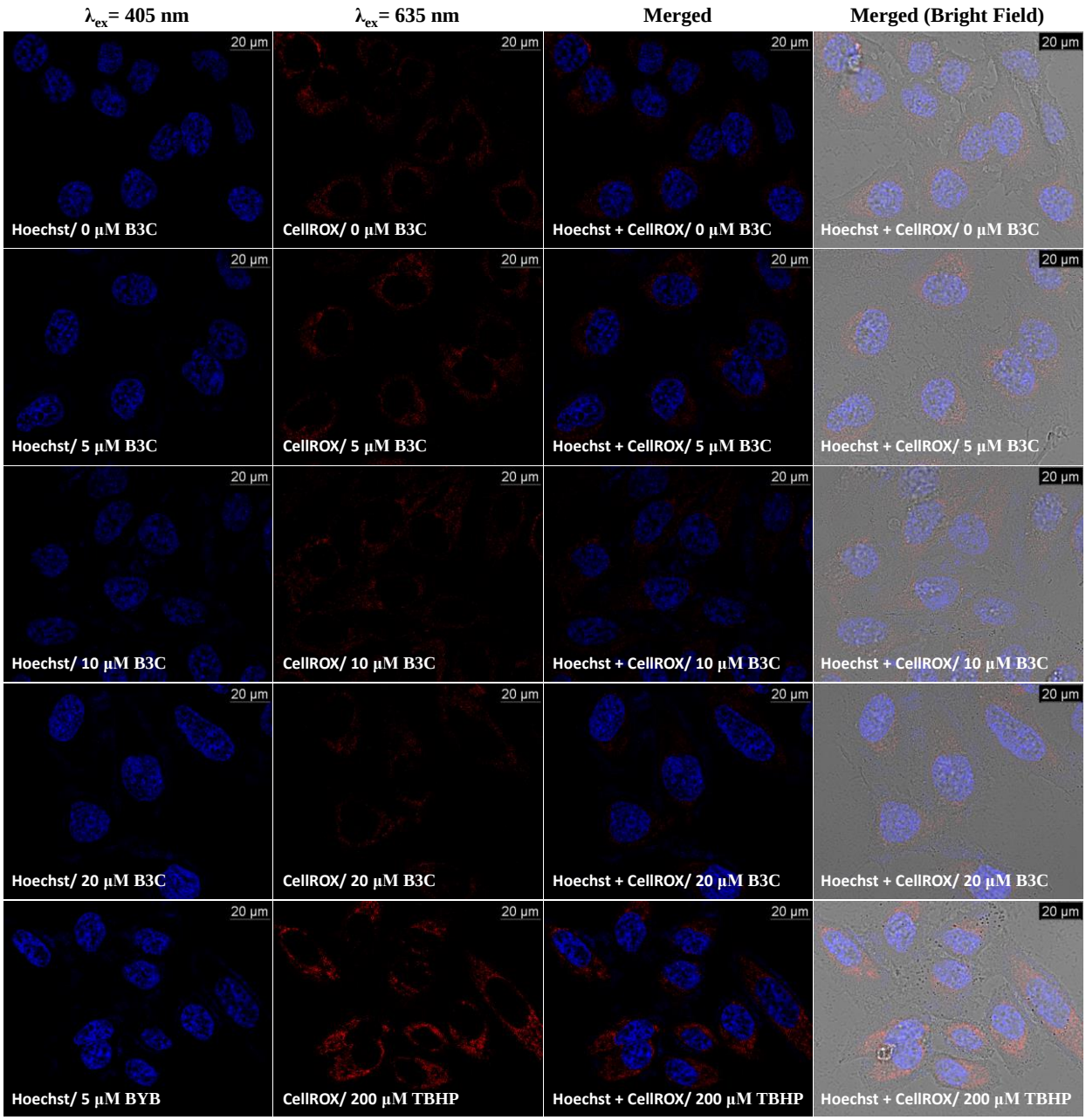

Figure 3.4. Confocal live cell imaging to investigate ROS levels in cytoplasm with CellROX Deep Red after the treatment of **B3C** (0, 5, 10, and 20 µM) and TBHP (200 µM) for 24 h.

of the cells was not influenced by the ligand. The results strongly support that **B3C** may not show

obvious effects on the integrity of mitochondrial membrane. Taken together, the treatment with **B3C** is not likely to generate cellular ROS and induce mitochondrial-related apoptotic pathway.

On the other hand, Abulaiti *et al.* illustrated that the expression of RAS proteins caused chromosomal instability.[99] The damaged DNA promotes the cells to exhibit transformation such

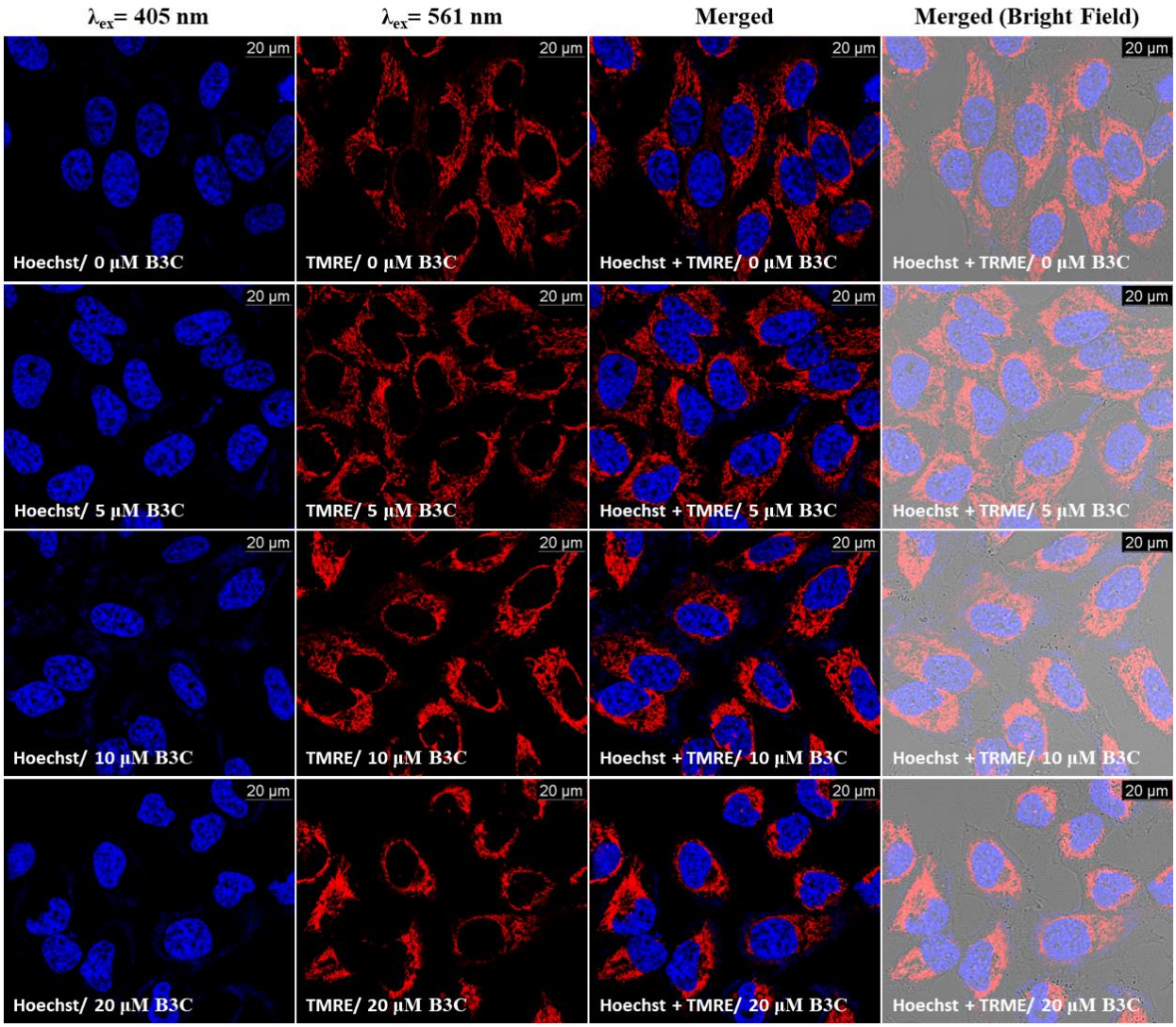

Figure 3.5. Confocal live cell imaging to investigate the change of mitochondrial membrane potential with the use of TRME after the treatment of B3C (0, 5, 10, and 20 μM) for 24 h.

as alteration in cell morphology, growth regulation, and dedifferentiation. Strikingly, it was found that the survived cells were a lack of γ-H2AX and also had a low activation on p53. They further treated the survived cells with a DNA-damage agent and found that the cells were not able to undergo cell cycle arresting nor induce the formation of γ-H2AX. These findings indicate that the RAS expressed cancer cells may be impaired in their ability to respond to DNA damage and leading

to defective repair despite the existing of chromosomal instability. These examples inspired us whether the downregulation of NRAS by **B3C** could be able to restore the ability of cells to respond to DNA damage by reactivating DNA damage response (DDR). In other words, the upregulation of γ-H2AX may not be a consequence of oxidative DNA damage induced by **B3C,** but it could be probably due to the repression of NRAS protein.

The study from Abulaiti *et al.* indicated that another biofunction of NRAS protein is to induce chromosome instability and abrogate the DDR by suppressing the phosphorylation of p53. As γ-H2AX functions to assemble various DNA repair proteins at the sites of damaged chromatin for initiating the DNA repair mechanism,[95, 100] the increasing in cellular level of γ-H2AX after treatment of **B3C** observed may indicate the restoration of DDR and the activation of DNA repairing. To understand the mechanism on the restoration of DDR, western blotting was performed to study the expression level of phosphorylated-p53 (phos-p53 (S15)). The result (Figure 3.2) clearly showed that the expression level of phos-p53 (S15) was upregulated after **B3C** treatment in a dose-dependent manner. Taken together, the result suggested that the downregulation of NRAS by **B3C** may increase the phosphorylation of p53 on the Serine 15 site significantly, and then DDR may be able to be activated the by phos-p53 in HeLa cells. Therefore, γ-H2AX was recruited to repair the damaged DNA caused by NRAS itself.

3.2.2. Study on the arresting of cell cycle and the induction of apoptosis by **B3C**

NRAS protein acts as the molecular switches to govern the activation of a number of signaling pathways, such as the RAF-MEK-ERK and PI3K-AKT-mTOR pathway, to regulate the cellular processes by enabling the cell cycles from processing.[66] As NRAS protein was downregulated together with the activation of DDR after the **B3C** treatment, the cell cycles may be affected from processing.[101, 102] Thus, cell cycle analysis was carried out to evaluate whether the activation of DDR after the downregulation of NRAS protein by **B3C** is able to inhibit cancer cells by arresting the cell cycles. After treating HeLa cells with different concentration of **B3C** for 24 h, the

cells were harvested, penetrated, and incubated with PI to analyze the proportion of cells in each phase (G_0/G_1, S, and G_2/M) by flow cytometry. From the result of cell cycle (Figure 3.6), it was found that the proportion of cells in S phase remarkably increased after **B3C** treatment and was found to be concentration dependent, in which a maximum increase of 48% (0 μM: 14.2%; 10 μM: 21.0%) was found in S phase. In term of G_0/G_1 and G_2/M phases, they both showed a decreasing trend as the concentration of **B3C** increased in the treatment. The results indicate that **B3C** is likely to induce the S phase arresting upon downregulating the expression of NRAS protein at translational level and that leads to cell growth inhibition. In addition, it is noteworthy that DNA damage is one of the key causes of S phase arresting[103, 104] as the cells may elongate S phase in order to repair the damaged DNA before entering G_2/M phase for cell division. In other words, it may support that the downregulation of the translation of NRAS protein by **B3C** may induce DDR, activate cell cycle checkpoints, and ultimately lead to S phase arresting in HeLa cells for repairing the damaged DNA. The detailed mechanism will be discussed further in the following.

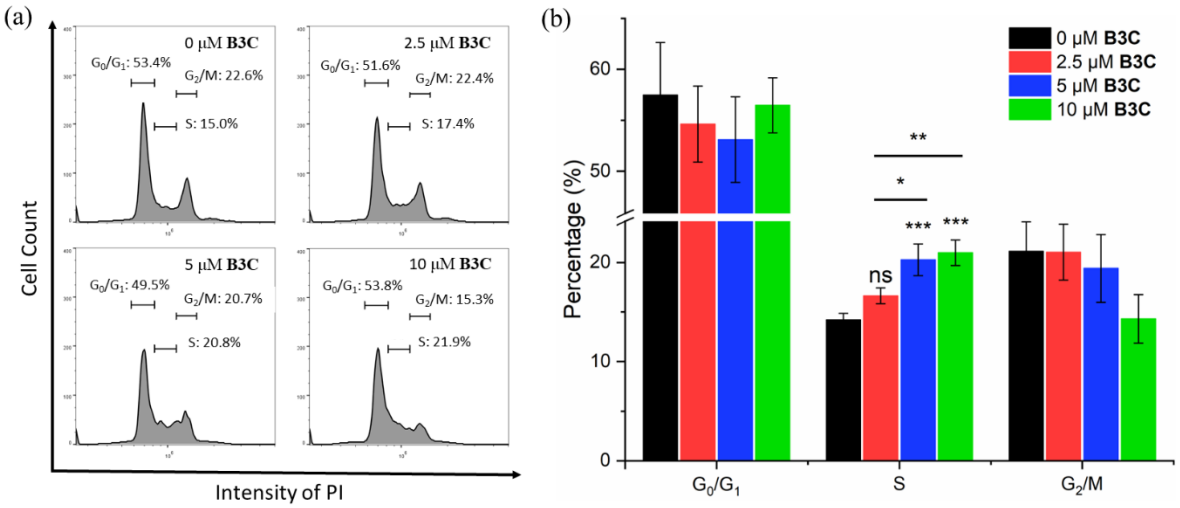

Figure 3.6. (a) Cell cycle analysis with PI staining to determine the proportion of HeLa cells in each phase after treating with **B3C** (0, 2.5, 5 and 10 μM) for 24 h. (b) The percentage of HeLa cells in different phases in the cell cycle after the treatments with **B3C** of different concentration (N= 3, mean ± SD).

Cell cycle is a series of basic biological activities for cell growth and division.[105-107] Among the phases, S phase is the stage for DNA and histone synthesis before DNA division.[108] The arresting of cell cycle at S phase inhibits the replication of DNA to undergo mitosis. The lacking of necessary DNA for cell division may inhibit the cell proliferation and lead to apoptosis eventually.[98] Therefore, the apoptotic effect caused by **B3C** in HeLa cells was studied by flow cytometry with the use of Alexa Fluor 647 conjugated Annexin V. The results (Figure 3.7) show that apoptosis of HeLa cells was induced from 4.8 % (Control group) to 7.5 %, 13.0 %, and 20.1 % upon the treatment with **B3C** of 5, 10 and 20 μM for 24 h, respectively. In addition to the apoptotic study by Annexin V, the expression of two apoptotic proteins, Poly [ADP-ribose] polymerase 1 (PARP-1) and cleaved caspase-3, were analyzed via western blot assays to confirm the induced apoptosis by **B3C**. From the result shown in Figure 3.2, a significant increase in the expression of cleaved PARP-1 (lower band) and cleaved caspase-3 was observed in a dose-dependent manner. Considering the results obtained from Annexin V staining study and western blots assays, **B3C** may induce apoptosis in HeLa cells effectively.

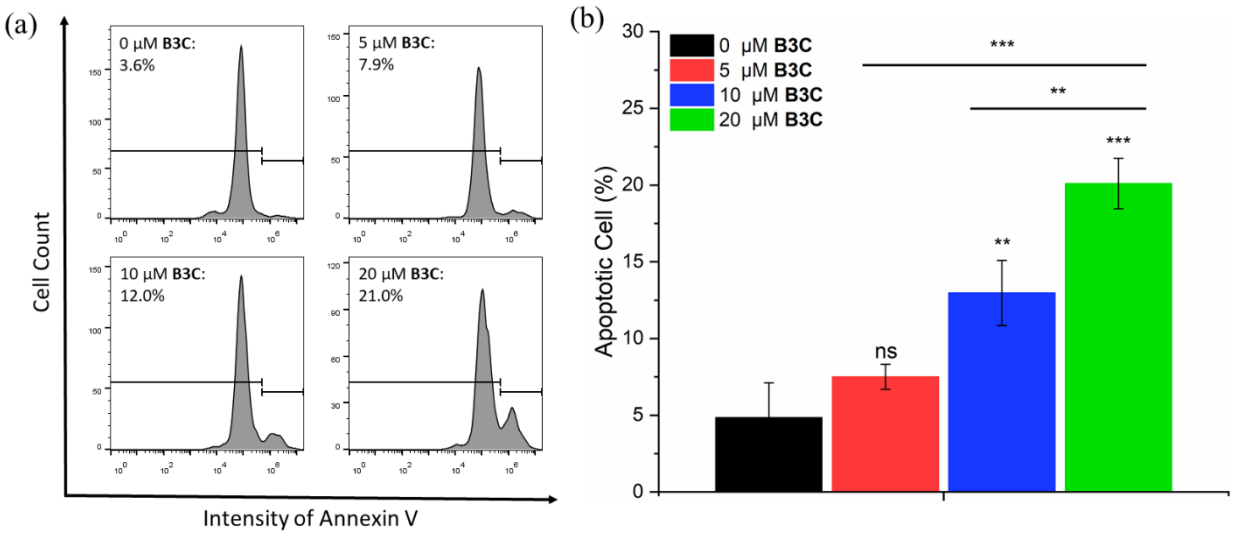

Figure 3.7. (a) Apoptosis analysis with Alexa Fluor 647 conjugated Annexin V to determine the apoptotic HeLa cells after treating with **B3C** (0, 5, 10 and 20 μM) for 24 h. (b) The percentage of apoptotic HeLa cells after the treatments with **B3C** of different concentration (N= 3, mean ± SD).

3.2.3. Study on the cell growth inhibition mechanism by **B3C**

Some recent studies have revealed that cell cycle arresting may be related to sencescence and

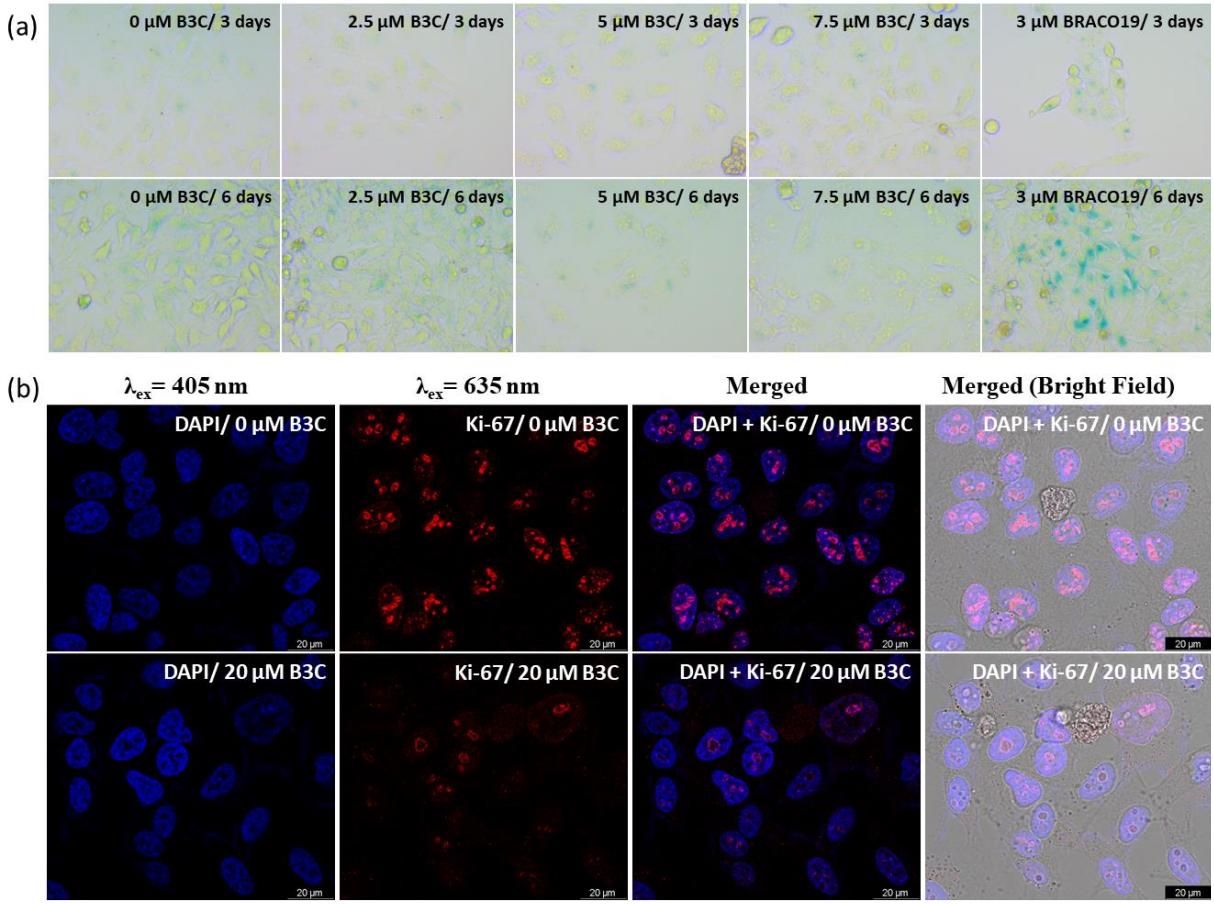

Figure 3.8. (a) SA-β-gal assays to investigate the induced senescence on HeLa cells after treatment with **B3C** (0, 2.5, 5, and 7.5 μM) and **BARCO19** (3 μM) for 3 and 6 days. (b) Ki-67 immunofluorescent assay with the use of confocal microscope to investigate the cell proliferation of HeLa cell after treatment with **B3C** (20 μM) for 24 h.

resultin apoptosis of cancer cells.[109, 110] In order to explore the mechanism on the induction of apoptosis by **B3C**, β-Galactosidase (SA-β-gal) staining assays were performed to investigate the senescence of HeLa cells treated with **B3C** at different concentrations for 3 and 6 days. In the assay, a commerial telomere G4-ligand, **BRACO19**, was used as a positive control for comparison. As indicated from the result of SA-β-gal assays (Figure 3.8a), the blue staining in HeLa cells was found very weak despite the treatment with **B3C** at 7.5 μM was carried out for 6 days. On the contrary, the positive control, **BRACO19**, showed a much stronger blue staining, which revealed clearly the induction of HeLa cells senescence by the ligand. Compared to the effects from **BRACO19**, this result indicates that **B3C** may not as effective as **BRACO19** in inducing HeLa cell senescence. However, it may support that **B3C** does not interact with cellular telomeric G4s that are located in the nucleus to cause senescence.

As previously indicated, NRAS protein is responsible for the signal transduction for cell proliferation.[61] Thus, a immunofluorescent imaging was carried out by staining Ki-67 protein, a proliferation marker, to study the effect on cell proliferation when NRAS was downregulated by **B3C**. From Figure 3.8b, a remarkable reduction in the fluorescent signal of Ki-67 staining was found after the treatment with **B3C** at 20 μM for 24 h. This result clearly suggests that **B3C** may inhibit the HeLa cells from proliferating actively, which is consistent with the functions of NRAS in cells. Taken together, the downregulation of NRAS by **B3C** most likely inhibits HeLa cells by suppressing the cellular proliferation through signaling pathway such as disrupting cell cycle but not inducing senescence.

3.3. Summary

In summary, it is found that the treatment of **B3C** downregulated the translation of NRAS in HeLa cells but with no observable effects on transcriptional level. The results also suggest that **B3C** may target the cellular *NRAS* mRNA G4s, repress the corresponding NRAS expression and inhibit the HeLa cells in a dose-dependent manner. Besides, it was observed that **B3C** upregulated DDR related protein, phos-p53 and γ-H2AX, caused cell cycle arresting at S phase, and induced apoptosis in a dose-dependent manner. We further investigated the inhibition mechanism for cell proliferation by performing the bioassays including SA-β-gal assays and confocal microscopic imaging assays. The results indicate that **B3C** inhibits the HeLa cells from active proliferating but with non-significant effects on both cellular senescence and ROS generation. This result is in alignment with the function of NRAS, which transducts the signal for cell proliferation. Reported studies revealed that RAS may impair the cell from activating DDR. The increase in the expression of phos-p53 and γ-H2AX without oxidative DNA damage by ROS indicate that the downregulation of NRAS may contribute to the reactivation of DDR, initiation of the DNA repair mechanism, causing S phase prolongation for DNA repair, and ultimately inducing apoptosis. These results obtained thus far clearly supported that the downregulation of NRAS protein can oppose the two main functions of NRAS, which showed a good alignment with the previous studies on RAS

proteins.[99] To the best of our knowledge, this is the first study targeting *NRAS* mRNA G4 with RNA G4-ligand and provides evidence on restoring the DNA damage response that abrogated by RAS proteins in cancer cells. The anticancer mechanism of **B3C** that effectively downregulates NRAS by targeting the proto-oncogenic *NRAS* mRNA G4 in HeLa cells may provide new insights into drug discovery against RAS-driven cancers.

Chapter 4. Experimental Section

4.1. Materials

4.1.1. Chemicals

2-Methylbenzothiazole, 3-bromopropanamide, 4-(methtlthio)benzaldehyde, indole-2-carboxaldehyde, indole-3-carboxaldehyde, and N-ethylcarbazole-3-carboxaldehyde were purchased from Tokyo Chemical Industry (TCI). 3-Bromopropanol, 3-bromopropanoic acid, 4-(dimethylamino)benzaldehyde, 7-(diethylamino)-2-oxo-2H-chromene-3-carbaldehyde, 1-butanol, potassium carbonate, tris(hydroxymethyl)aminomethane (Tris), hydrochloric acid, potassium chloride, potassium phosphate dibasic, and potassium phosphate monobasic were purchased from Sigma-Aldrich. Dimethyl sulfoxide-d6 (DMSO-d_6) was purchased from Cambridge Isotope Laboratories. All reagents and solvents were purchased from commercial sources and used without further purification.

4.1.2. Oligonucleotides and primers

All oligonucleotides and primers used in the present study were synthesized and purified via HPLC by BGI Genomics and their sequences were listed in Appendix (Table. S1 and S2)

4.1.3. Cell cultures

Dulbecco's Modified Eagle Medium (DMEM), Roswell Park Memorial Institute (RPMI) 1640 Medium, Fetal Bovine Serum (FBS) (United Stated), and Penicillin-Streptomycin (10,000 U/mL) (P/S) were purchased from Gibco^{TM} .

4.2. Synthesis

4.2.1. General synthetic procedures for intermediates **a1-a3**

2-Methylbenzothiazole (1g, 6.7mmol) and 3-bromopropanol (0.932g, 7.37mmol) (or 3-bromopropionamide or 3-bromopropionic acid) were added to a pressure vessel and then 5.0 mL acetonitrile was added into the mixture. The vessel was then closed. The reaction mixture was

heated up for reaction under stirring at 110 °C under stirring conditions for 24-48 hours. Reactions were monitored by TLC. Upon completed reaction, the reaction vessel was cooled down in room temperature for 15 minutes. Subsequently, 30 mL of ethyl acetate were added to the mixture. The precipitated solid was collected by suction filtration. The solid obtained was dissolved in minimum amount of D.I. H_2O and then was extracted with 15 mL ethyl acetate for 3 times. Intermediate **a1** (or **a2** or **a3**) was obtained by removing D.I. H_2O under vacuum and then was used for synthesis in the next step without further purification.

4.2.2. General synthetic procedures of ligands **B1S-B3Cou**

To the mixture of intermediate **a1** (50 mg, 0.173 μmol) (or **a2** or **a3**) and 4-(methtlthio)benzaldehyde (31.7 mg, 0.208 μmol) (or other aromatic aldehyde such as 4-(dimethylamino)benzaldehyde, indole-2-carboxaldehyde, indole-3-carboxaldehyde, N-ethylcarbazole-3-carboxaldehyde, and 7-(diethylamino)-2-oxo-2H-chromene-3-carbaldehyde) in 1 mL 1-butanol, 5mg potassium carbonate was added as a base. The reaction mixture was heated up to 100 °C for reaction under stirring condition for 3-5 hours. After that, the reaction mixture was cooled down in room temperature for 15 minutes. The precipitated solid was washed with ethyl acetate and collected under suction filtration. The solids collected were then further purified by column chromatography using a mixture of chloroform and methanol (10-30%) as an eluent.

4.2.3. The characterization of ligands synthesized

(E)-3-(3-hydroxypropyl)-2-(4-(methylthio)styryl)benzo[d]thiazol-3-ium Bromide (B1S). Isolated yield= 67%. ^{1}H NMR (400 MHz, DMSO-d_6) δ 8.45 (dd, J = 8.2, 1.3 Hz, 1H), 8.27 (d, J = 8.5 Hz, 1H), 8.23 (d, J = 15.8 Hz, 1H), 8.06 – 7.96 (m, 3H), 7.88 (ddd, J = 8.5, 7.3, 1.3 Hz, 1H), 7.82 – 7.75 (m, 1H), 7.43 (d, J = 8.4 Hz, 2H), 4.97 (t, J = 7.1 Hz, 2H), 4.87 (s, 1H), 3.55 (t, J = 5.7 Hz, 2H), 2.58 (s, 3H), 2.05 (p, J = 6.5 Hz, 2H). ^{13}C NMR (101 MHz, DMSO-d_6) δ 171.97, 148.48, 145.12, 141.35, 130.31, 130.19, 129.46, 128.33, 128.15, 125.47, 124.42, 116.68, 112.32, 57.35, 46.42, 31.42, 14.00. HRMS calculated m/z for $C_{19}H_{20}NOS_2^+$: 342.0986; found 342.0989.

(E)-3-(3-amino-3-oxopropyl)-2-(4-(methylthio)styryl)benzo[d]thiazol-3-ium Bromide (**B2S**). Isolated yield= 80%. ^{1}H NMR (400 MHz, DMSO-d_6) δ 8.44 (dd, J = 8.2, 1.3 Hz, 1H), 8.26 (d, J = 8.5 Hz, 1H), 8.22 (d, J = 15.8 Hz, 1H), 8.08 (d, J = 15.8 Hz, 1H), 7.98 (d, J = 8.4 Hz, 2H), 7.87 (ddd, J = 8.5, 7.3, 1.3 Hz, 1H), 7.81 – 7.75 (m, 1H), 7.58 – 7.49 (m, 1H), 7.43 (d, J = 8.5 Hz, 2H), 7.11 (s, 1H), 5.11 (t, J = 6.7 Hz, 2H), 2.79 (t, J = 6.6 Hz, 2H), 2.58 (s, 3H). ^{13}C NMR (101 MHz, DMSO-d_6) δ 172.34, 170.79, 148.29, 145.12, 130.38, 130.18, 129.44, 128.32, 128.01, 125.48, 124.39, 116.87, 112.83, 45.31, 33.70, 14.01. HRMS calculated m/z for $C_{19}H_{19}N_2OS_2^+$: 355.0939; found 355.0939.

(E)-3-(2-carboxyethyl)-2-(4-(methylthio)styryl)benzo[d]thiazol-3-ium Bromide (**B3S**). Isolated yield= 81%. ^{1}H NMR (400 MHz, DMSO-d_6) δ 12.71 (s, 1H), 8.44 (dd, J = 8.1, 1.3 Hz, 1H), 8.29 (d, J = 8.5 Hz, 1H), 8.22 (d, J = 15.7 Hz, 1H), 8.08 (d, J = 15.8 Hz, 1H), 8.01 (d, J = 8.5 Hz, 2H), 7.86 (ddd, J = 8.5, 7.2, 1.3 Hz, 1H), 7.81 – 7.75 (m, 1H), 7.45 – 7.39 (m, 2H), 5.08 (t, J = 7.2 Hz, 2H), 2.96 (t, J = 7.1 Hz, 2H), 2.58 (s, 3H). ^{13}C NMR (101 MHz, DMSO-d_6) δ 172.66, 171.50, 148.53, 145.13, 141.11, 130.36, 130.30, 129.46, 128.29, 127.99, 125.42, 124.38, 116.86, 112.74, 44.74, 32.53, 14.01. HRMS calculated m/z for $C_{19}H_{18}NO_2S_2^+$: 356.0779; found 356.0778.

(E)-2-(4-(dimethylamino)styryl)-3-(3-hydroxypropyl)benzo[d]thiazol-3-ium Bromide (**B1N**). Isolated yield= 61%. ^{1}H NMR (400 MHz, DMSO-d_6) δ 8.31 (dd, J = 8.1, 1.2 Hz, 1H), 8.14 – 8.06 (m, 2H), 7.89 (d, J = 8.7 Hz, 2H), 7.78 (ddd, J = 8.5, 7.3, 1.3 Hz, 1H), 7.71 – 7.60 (m, 2H), 6.84 (d, J = 8.8 Hz, 2H), 4.90 (t, J = 4.9 Hz, 1H), 4.83 (t, J = 7.1 Hz, 2H), 3.55 (q, J = 5.6 Hz, 2H), 3.11 (s, 6H), 2.01 (p, J = 6.6 Hz, 2H). ^{13}C NMR (101 MHz, DMSO) δ 171.24, 153.53, 150.39, 141.25, 132.85, 128.95, 127.41, 127.10, 123.97, 121.48, 115.80, 111.97, 105.89, 57.35, 45.48, 39.77, 31.25. HRMS calculated m/z for $C_{20}H_{23}N_2OS^+$: 339.1531; found 339.1534.

(E)-3-(3-amino-3-oxopropyl)-2-(4-(dimethylamino)styryl)benzo[d]thiazol-3-ium Bromide (**B2N**). Isolated yield= 92%. ^{1}H NMR (400 MHz, DMSO-d_6) δ 8.30 (dd, J = 8.1, 1.2 Hz, 1H), 8.13 – 8.04 (m, 2H), 7.90 (d, J = 8.8 Hz, 2H), 7.80 – 7.74 (m, 1H), 7.73 – 7.64 (m, 2H), 7.58 (s, 1H), 7.10 (s, 1H), 6.85 (d, J = 8.8 Hz, 2H), 4.98 (t, J = 6.7 Hz, 2H), 3.11 (s, 6H), 2.74 (t, J = 6.7 Hz, 2H). ^{13}C NMR (101 MHz, DMSO) δ 171.46, 170.88, 153.56, 150.33, 141.06, 132.88, 128.89, 127.39, 126.97, 123.92, 121.55, 115.96, 111.99, 106.28, 44.47, 39.76, 33.63. HRMS calculated m/z for $C_{20}H_{22}N_3OS^+$: 352.1483; found 352.1484.

(E)-3-(2-carboxyethyl)-2-(4-(dimethylamino)styryl)benzo[d]thiazol-3-ium Bromide (**B3N**). Isolated yield= 87%. ^{1}H NMR (400 MHz, DMSO-d_6) δ 12.70 (s, 1H), 8.30 (dd, J = 8.1, 1.2 Hz, 1H), 8.12 (d, J = 8.4 Hz, 1H), 8.07 (d, J = 15.2 Hz, 1H), 7.92 (d, J = 8.7 Hz, 2H), 7.76 (ddd, J = 8.5, 7.3, 1.3 Hz, 1H), 7.71 – 7.64 (m, 2H), 6.83 (d, J = 8.8 Hz, 2H), 4.95 (t, J = 7.2 Hz, 2H), 3.10 (s, 6H), 2.90 (t, J = 7.2 Hz, 2H). ^{13}C NMR (101 MHz, DMSO-d_6) δ 171.74, 171.57, 153.56, 150.58, 140.99, 133.02, 128.91, 127.36, 126.95, 123.91, 121.55, 115.92, 111.93, 106.17, 43.89, 32.38. HRMS calculated m/z for $C_{20}H_{21}N_2O_2S^+$: m/z: 353.1324; found 353.1325.

(E)-2-(2-(1H-indol-2-yl)vinyl)-3-(3-hydroxypropyl)benzo[d]thiazol-3-ium Bromide (**B1I2C**). Isolated yield= 72%. ^{1}H NMR (400 MHz, DMSO-d_6) δ 12.15 (s, 1H), 8.42 (dd, J = 8.2, 1.2 Hz, 1H), 8.27 (d, J = 15.6 Hz, 1H), 8.23 (d, J = 8.4 Hz, 1H), 7.97 (d, J = 15.6 Hz, 1H), 7.86 (ddd, J = 8.5, 7.3, 1.3 Hz, 1H), 7.80 – 7.74 (m, 1H), 7.70 (d, J = 8.1 Hz, 1H), 7.52 (dd, J = 8.3, 1.1 Hz, 1H), 7.37 – 7.29 (m, 2H), 7.10 (ddd, J = 8.0, 6.9, 1.0 Hz, 1H), 4.88 (t, J = 7.2 Hz, 2H), 4.83 (s, 1H), 3.61 (t, J = 5.8 Hz, 2H), 2.09 (p, J = 6.4 Hz, 2H). ^{13}C NMR (101 MHz, DMSO-d_6) δ 171.12, 141.30, 139.53, 138.23, 134.34, 129.34, 128.07, 127.91, 127.86, 126.20, 124.34, 122.16, 120.62, 116.39, 113.58, 111.92, 110.64, 57.66, 46.60, 31.40. HRMS calculated m/z for $C_{20}H_{19}N_2OS^+$: 335.1218; found 355.1215.

(E)-2-(2-(1H-indol-2-yl)vinyl)-3-(3-amino-3-oxopropyl)benzo[d]thiazol-3-ium Bromide (**B2I2C**). Isolated yield= 82%. ^{1}H NMR (400 MHz, DMSO-d_6) δ 12.40 – 12.18 (m, 1H), 8.40 (dd, J = 8.2, 1.2 Hz, 1H), 8.30 – 8.17 (m, 2H), 8.05 (d, J = 15.6 Hz, 1H), 7.84 (ddd, J = 8.5, 7.2, 1.2 Hz, 1H), 7.78 – 7.72 (m, 1H), 7.69 (d, J = 8.0 Hz, 1H), 7.66 – 7.59 (m, 1H), 7.51 (dd, J = 8.3, 1.1 Hz, 1H), 7.37 – 7.27 (m, 2H), 7.16 – 7.05 (m, 2H), 5.02 (t, J = 7.0 Hz, 2H), 2.83 (t, J = 7.0 Hz, 2H). ^{13}C NMR (101 MHz, DMSO-d_6) δ 171.93, 171.08, 141.53, 140.05, 138.69, 134.88, 129.75, 128.52, 128.39, 128.18, 126.72, 124.74, 122.67, 121.09, 117.11, 114.12, 112.40, 111.36, 45.71, 34.19. HRMS calculated m/z for $C_{20}H_{18}N_3OS^+$: 348.1171; found 348.1244.

(E)-2-(2-(1H-indol-2-yl)vinyl)-3-(2-carboxyethyl)benzo[d]thiazol-3-ium Bromide (**B3I2C**). Isolated yield= 84%. ^{1}H NMR (400 MHz, DMSO-d_6) δ 12.47 (s, 1H), 8.40 (d, J = 8.0 Hz, 1H), 8.27 (dd, J = 12.0, 3.5 Hz, 2H), 8.12 (d, J = 15.6 Hz, 1H), 7.83 (t, J = 7.8 Hz, 1H), 7.74 (t, J = 7.7 Hz, 1H), 7.68 (d, J = 8.0 Hz, 1H), 7.50 (d, J = 8.3 Hz, 1H), 7.31 (q, J = 5.9, 4.6 Hz, 2H), 7.08 (t, J = 7.5 Hz, 1H), 5.01 (t, J = 7.3 Hz, 2H), 3.01 (t, J = 7.3 Hz, 2H). ^{13}C NMR (101 MHz, DMSO-d_6) δ 172.17, 171.81, 141.53, 140.09, 138.81, 134.93, 129.76, 128.49, 128.37, 128.18, 126.70, 124.72, 122.66, 121.06, 117.11, 114.20, 112.43, 111.43, 45.04, 32.99. HRMS calculated m/z for $C_{20}H_{17}N_2O_2S^+$: 349.1011; found 349.1010.

(E)-2-(2-(1H-indol-3-yl)vinyl)-3-(3-hydroxypropyl)benzo[d]thiazol-3-ium Bromide (**B1I3C**). Isolated yield= 78%. ^{1}H NMR (400 MHz, DMSO-d_6) δ 12.54 (s, 1H), 8.52 – 8.40 (m, 2H), 8.34 (dd, J = 8.1, 1.2 Hz, 1H), 8.29 – 8.22 (m, 1H), 8.16 (d, J = 8.4 Hz, 1H), 7.79 (ddd, J = 8.5, 7.3, 1.3 Hz, 1H), 7.69 (t, J = 7.6 Hz, 1H), 7.65 – 7.51 (m, 2H), 7.34 (tt, J = 7.3, 5.7 Hz, 2H), 5.05 (t, J = 4.8 Hz, 1H), 4.87 (t, J = 7.0 Hz, 2H), 3.57 (q, J = 5.4 Hz, 2H), 2.08 (q, J = 6.4 Hz, 2H). ^{13}C NMR (101 MHz, DMSO-d_6) δ 171.63, 144.50, 141.27, 138.60, 128.89, 127.25, 126.81, 124.80, 123.95, 122.54, 121.01, 115.68, 114.64, 113.37, 105.01, 57.10, 45.29, 30.98. HRMS calculated m/z for $C_{20}H_{19}N_2OS^+$: 335.1218; found 335.1217.

(E)-2-(2-(1H-indol-3-yl)vinyl)-3-(3-amino-3-oxopropyl)benzo[d]thiazol-3-ium Bromide (**B2I3C**). Isolated yield= 87%. ^{1}H NMR (400 MHz, DMSO-d_6) δ 12.59 – 12.47 (m, 1H), 8.43 (dd, J = 8.9, 6.4 Hz, 2H), 8.37 – 8.30 (m, 2H), 8.14 (d, J = 8.4 Hz, 1H), 7.79 (ddd, J = 8.5, 7.3, 1.3 Hz, 1H), 7.72 – 7.66 (m, 2H), 7.61 – 7.52 (m, 2H), 7.38 – 7.31 (m, 2H), 7.15 (s, 1H), 5.01 (t, J = 6.4 Hz, 2H), 2.82 (t, J = 6.3 Hz, 2H). ^{13}C NMR (101 MHz, DMSO-d_6) δ 172.27, 171.05, 144.71, 141.11, 138.14, 138.12, 138.02, 128.90, 127.35, 126.77, 124.63, 123.98, 122.55, 121.12, 115.93, 114.54, 113.16, 105.93, 44.59, 33.52. HRMS calculated m/z for $C_{20}H_{18}N_3OS^+$: 348.1171; found 348.1168.

(E)-2-(2-(1H-indol-3-yl)vinyl)-3-(2-carboxyethyl)benzo[d]thiazol-3-ium Bromide (**B3I3C**). Isolated yield= 86%. ^{1}H NMR (400 MHz, DMSO-d_6) δ 12.68 (s, 2H), 8.43 (d, J = 16.1 Hz, 2H), 8.31 (dd, J = 8.1, 1.2 Hz, 1H), 8.29 – 8.23 (m, 1H), 8.14 (d, J = 8.4 Hz, 1H), 7.78 (ddd, J = 8.5, 7.2, 1.3 Hz, 1H), 7.72 – 7.62 (m, 2H), 7.62 – 7.55 (m, 1H), 7.39 – 7.28 (m, 2H), 5.01 (t, J = 6.7 Hz, 2H), 2.96 (t, J = 6.7 Hz, 2H). ^{13}C NMR (101 MHz, DMSO-d_6) δ 172.46, 171.88, 144.66, 141.08, 137.99, 137.91, 128.92, 127.36, 126.77, 124.75, 123.98, 123.92, 122.49, 120.89, 115.93, 114.44, 113.21, 105.90, 44.03, 32.41. HRMS calculated m/z for $C_{20}H_{17}N_2O_2S^+$: 349.1011; found 349.1008.

(E)-2-(2-(9-ethyl-9H-carbazol-3-yl)vinyl)-3-(3-hydroxypropyl)benzo[d]thiazol-3-ium Bromide (**B1C**). Isolated yield= 71%. ^{1}H NMR (400 MHz, DMSO-d_6) δ 8.88 (d, J = 1.7 Hz, 1H), 8.49 – 8.38 (m, 2H), 8.31 – 8.16 (m, 3H), 8.05 (d, J = 15.6 Hz, 1H), 7.90 – 7.81 (m, 2H), 7.81 – 7.70 (m, 2H), 7.57 (ddd, J = 8.3, 7.2, 1.2 Hz, 1H), 7.35 (t, J = 7.5 Hz, 1H), 4.98 (t, J = 7.1 Hz, 3H), 4.54 (q, J = 7.1 Hz, 2H), 3.60 (s, 2H), 2.09 (t, J = 6.4 Hz, 2H), 1.37 (t, J = 7.1 Hz, 3H). ^{13}C NMR (101 MHz, DMSO-d_6) δ 171.92, 150.88, 142.21, 141.29, 140.29, 129.23, 128.04, 127.96, 127.69, 126.85, 125.22, 124.23, 123.93, 122.93, 122.22, 120.78, 120.25, 116.34, 110.10, 110.07, 109.83, 57.41, 46.17, 37.44, 31.44, 13.84. HRMS calculated m/z for $C_{26}H_{25}N_2OS^+$: 413.1688; found 413.1689.

(E)-3-(3-amino-3-oxopropyl)-2-(2-(9-ethyl-9H-carbazol-3-yl)vinyl)benzo[d] thiazol-3-ium Bromide (**B2C**). Isolated yield= 81%. ^{1}H NMR (400 MHz, DMSO-d_6) δ 8.88 (d, J = 1.8 Hz, 1H), 8.47 – 8.37 (m, 2H), 8.22 (dt, J = 8.9, 2.7 Hz, 3H), 8.11 (d, J = 15.6 Hz, 1H), 7.88 – 7.81 (m, 2H), 7.75 (dd, J = 14.6, 7.8 Hz, 2H), 7.62 – 7.53 (m, 2H), 7.35 (t, J = 7.5 Hz, 1H), 7.14 (s, 1H), 5.13 (t, J = 6.7 Hz, 2H), 4.54 (q, J = 7.1 Hz, 2H), 2.83 (t, J = 6.6 Hz, 2H), 1.37 (t, J = 7.1 Hz, 3H). ^{13}C NMR (101 MHz, DMSO-d_6) δ 172.33, 170.85, 150.78, 142.25, 141.15, 140.32, 129.24, 128.01, 127.81, 127.59, 126.89, 125.30, 124.23, 124.06, 122.91, 122.21, 120.63, 120.32, 116.58, 110.30, 110.21, 110.15, 45.06, 33.75, 13.85. HRMS calculated m/z for $C_{26}H_{24}N_3OS^+$: 426.1640; found 426.1640.

(E)-3-(2-carboxyethyl)-2-(2-(9-ethyl-9H-carbazol-3-yl)vinyl)benzo[d]thiazol-3-ium Bromide (**B3C**). Isolated yield= 81%. ^{1}H NMR (400 MHz, DMSO-d_6) δ 12.72 (s, 1H), 8.88 (d, J = 1.7 Hz, 1H), 8.48 – 8.38 (m, 2H), 8.24 (t, J = 8.3 Hz, 3H), 8.09 (d, J = 15.6 Hz, 1H), 7.84 (t, J = 8.3 Hz, 2H), 7.75 (dd, J = 15.3, 8.0 Hz, 2H), 7.57 (t, J = 7.7 Hz, 1H), 7.35 (t, J = 7.5 Hz, 1H), 5.11 (t, J = 7.2 Hz, 2H), 4.54 (q, J = 7.1 Hz, 2H), 3.00 (t, J = 7.1 Hz, 2H), 1.37 (t, J = 7.1 Hz, 3H). ^{13}C NMR (101 MHz, DMSO-d_6) δ 172.65, 171.55, 151.00, 142.25, 141.09, 140.30, 129.26, 127.98, 127.91, 126.87, 125.27, 124.20, 122.89, 122.21, 120.65, 120.31, 116.55, 110.20, 110.15, 110.14, 44.47, 37.45, 32.54, 13.85. HRMS calculated m/z for $C_{26}H_{23}N_2O_2S^+$: 427.1480; found 427.1478.

(E)-2-(2-(7-(diethylamino)-2-oxo-2H-chromen-3-yl)vinyl)-3-(3-hydroxypropyl) benzo[d]thiazol-3-ium Bromide (**B1Cou**). Isolated yield= 62%. ^{1}H NMR (400 MHz, DMSO-d_6) δ 8.63 (s, 1H), 8.38 (dd, J = 8.1, 1.2 Hz, 1H), 8.23 (d, J = 8.5 Hz, 1H), 8.05 (q, J = 15.4 Hz, 2H), 7.83 (ddd, J = 8.6, 7.3, 1.3 Hz, 1H), 7.74 (t, J = 7.7 Hz, 1H), 7.58 (d, J = 9.1 Hz, 1H), 6.86 (dd, J = 9.1, 2.4 Hz, 1H), 6.65 (d, J = 2.3 Hz, 1H), 4.81 (t, J = 10.7 Hz, 3H), 3.53 (p, J = 7.1, 6.1 Hz, 6H), 2.04 (p, J = 6.5 Hz, 2H), 1.16 (t, J = 7.0 Hz, 6H).^{13}C NMR (101 MHz, DMSO-d_6) δ 171.67, 159.54, 157.22, 153.30, 148.25, 144.57, 141.43, 131.85, 129.34, 128.01, 127.75, 124.27, 116.40, 112.05, 111.11, 110.89, 108.91, 96.46, 57.51, 46.42, 44.69, 31.15, 12.46. HRMS calculated m/z for $C_{25}H_{27}N_2O_3S^+$: 435.1742; found 435.1741.

(E)-3-(3-amino-3-oxopropyl)-2-(2-(7-(diethylamino)-2-oxo-2H-chromen-3-yl)vinyl)benzo[d]thiazol-3-ium Bromide (**B2Cou**). Isolated yield= 71%. ^{1}H NMR (400 MHz, DMSO-d_6) δ 8.63 (s, 1H), 8.37 (d, J = 8.1 Hz, 1H), 8.23 (d, J = 8.5 Hz, 1H), 8.09 (d, J = 15.4 Hz, 1H), 7.99 (d, J = 15.3 Hz, 1H), 7.82 (t, J = 7.9 Hz, 1H), 7.72 (t, J = 7.7 Hz, 1H), 7.63 – 7.51 (m, 2H), 7.09 (s, 1H), 6.86 (dd, J = 9.2, 2.4 Hz, 1H), 6.66 (d, J = 2.4 Hz, 1H), 4.94 (t, J = 6.8 Hz, 2H), 3.52 (q, J = 7.0 Hz, 4H), 2.79 (t, J = 6.8 Hz, 2H), 1.16 (t, J = 7.0 Hz, 6H). ^{13}C NMR (101 MHz, DMSO-d_6) δ 172.03, 170.55, 159.51, 157.24, 153.31, 148.18, 144.50, 141.21, 131.84, 129.26, 127.99, 127.59, 124.20, 116.66, 112.07, 111.38, 110.90, 108.92, 96.49, 45.17, 44.70, 33.42, 12.47. HRMS calculated m/z for $C_{25}H_{26}N_3O_3S^+$: 448.1695; found 448.1695.

(E)-3-(2-carboxyethyl)-2-(2-(7-(diethylamino)-2-oxo-2H-chromen-3-yl)vinyl)benzo[d]thiazol-3-ium Bromide (**B3Cou**). Isolated yield= 69%. ^{1}H NMR (400 MHz, DMSO-d_6) δ 12.74 (s, 1H), 8.62 (s, 1H), 8.38 (dd, J = 8.1, 1.3 Hz, 1H), 8.27 (d, J = 8.5 Hz, 1H), 8.11 (d, J = 15.4 Hz, 1H), 8.02 (d, J = 15.3 Hz, 1H), 7.83 (ddd, J = 8.6, 7.2, 1.3 Hz, 1H), 7.74 (t, J = 7.7 Hz, 1H), 7.58 (d, J = 9.1 Hz, 1H), 6.88 (dd, J = 9.1, 2.4 Hz, 1H), 6.69 (d, J = 2.4 Hz, 1H), 4.94 (t, J = 7.2 Hz, 2H), 3.55 (q, J = 7.0 Hz, 4H), 2.95 (t, J = 7.2 Hz, 2H), 1.17 (t, J = 7.0 Hz, 6H). ^{13}C NMR (101 MHz, DMSO-d_6) δ 172.20, 171.36, 159.57, 157.25, 153.32, 148.14, 144.55, 141.19, 131.86, 129.31, 127.99, 127.60, 124.21, 116.62, 112.07, 111.30, 110.91, 108.93, 96.49, 44.71, 44.57, 32.38, 12.47. HRMS calculated m/z for $C_{25}H_{25}N_2O_4S^+$: 449.1535; found 449.1545.

4.3. Cell culture

Cell lines of human colon cancer HcT 116 (CCL-247), human cervix cancer HeLa (CCL-2), human skin cancer A375 (CRL-1619), human pancreatic duct cancer PANC-1 (CRL-1469), and human fibroblast HFF-1 (SCRC-1041) were purchased from ATCC. The cell lines were cultured in different complete medium as shown below: HcT 116 was cultured in RPMI 1640 (Gibco) supplemented with 10% FBS (Gibco) and 1% P/S (Gibco). HeLa, A375, PANC-1, and HFF-1 was

cultured in DMEM supplemented with 10% FBS and 1% P/S. The cells were incubated in incubator at 37 °C with 5% CO_2. In all experiments needed for cell collection, the cells were trypsinized by 0.25% trypsin-EDTA (Gibco) and suspended in various buffers for further analysis.

4.4. Enhanced fluorescent response for molecular interaction of the ligand with substrates

The fluorescence interaction experiments were performed with the use of fluorescent 96 well-plates (Corning#3650). In a 96-wells plate, 50 μL 1 μM ligand solutions (10 mM Tris, pH 7.4, 60 mM KCl) were mixed with 50 μL 100 μM oligonucleotide (10 mM Tris, pH 7.4, 60 mM KCl) such that the solution contained 0.5 μM ligand and 50 μM oligonucleotides (10 mM Tris, pH 7.4, 60 mM KCl), and were added into other wells. After standing for 15 mins, the samples were subjected to multimode microplate reader (TECAN) for enhanced fluorescent response measurements.

4.5. UV-Visible titration assay

UV-Visible titration assay was performed with the use of BioDrop Duo+ UV-Visible spectrophotometer (Biochrom) and a 1 cm x 2 mm quartz cuvette. Briefly, 5 μM ligands were dissolved in Tris-HCl buffer (10 mM, pH 7.4, containing 60 mM KCl), and different oligonucleotides (10 mM, pH 7.4, containing 60 mM KCl) were added slowly until the concentration of oligonucleotides reaching 15 μM.

4.6. Circular Dichroism (CD) measurements

4.6.1. CD spectra measurements

The RNA and DNA sequences were characterized with CD for their secondary structures. These RNA and DNA sequences were ordered in powder form (BGI Genomics) and were dissolved in 10 mM Tris buffer (pH 7.4 with or without 60 mM KCl) prepared by diethyl pyrocarbonate (DEPC)-treated water (ThermoFisher Scientific). The RNA and DNA sequences (5 μM) were mixed with

or without ligands (25 μM) and subjected to CD spectra measurement by J-1500 circular dichroism spectrophotometer (JASCO) with the use of 2 mm quartz cuvette under the following conditions: 1 nm bandwidth, 1 nm data pitch, 2 s digital integrated time (D.I.T), 220-700 nm scanned range, 100 nm/min scanning rate and performed at 25 °C.

4.6.2. CD melting temperature measurements

The melting temperature of RNA and DNA sequences (at 5 μM) with or without ligand was measured by J-1500 circular dichroism spectrophotometer with a Peltier-heating unit. The wavelengths with the highest CD peak (obtained from section 4.6.1) were used for measuring the melting temperature. Briefly, the RNA and DNA sequences dissolved in 10 mM Tris-HCl buffer (pH 7.4 with 20 mM KCl) were prepared by DEPC-treated water and were mixed with 5 and 25 μM ligands separately. The measurements were performed under the following conditions with the use of 2 mm quartz cuvette: 1 nm bandwidth, 1 nm data pitch, 2 s D.I.T., temperature range from 25 to 95 °C, 1 °C interval and 2 °C/min gradient. The melting temperature (T_m) was defined by the temperature when half of ellipticity was gone. The different in melting temperature (ΔT_m) of RNA or DNA mixed with or without ligands was defined by the different of their own melting temperature.

4.7. Isothermal Titration Calorimetry (ITC) Measurements

ITC experiments were performed at 25 °C with a MicroCal PEAQ-ITC automated ultrasensitive isothermal titration calorimeter (Malvern Instruments, Ltd). Syringe filled with 100 μM RNA substrates were titrated into the sample cell containing 10 μM **B3C**. The buffer system of both sample cell and syringe were prepared at 25 mM KH_2PO_4 (containing 60mM KCl) and 0.1% DMSO in DEPC-treated water. An initial injection of 0.4 μL of PI2 was performed followed with another 18 injections of 2 μL each. An injection duration of 2 seconds followed by 180 seconds equilibration time was applied. Constant stirring speed was set at a rate of 1000 rpm. Analysis of ITC data was done by MicroCal PEAQ-ITC Analysis software.

4.8. 3-(4,5-dimethylthiazol-2-yl)-2,5-diphenyltetrazolium bromide (MTT) assay

Cell lines of HcT 116, HeLa, A375, PANC-1 and HFF-1 were seeded at a density of 3 x 10^3 cells/well in a 96-well plate (TPP). After overnight incubation, the cells were treated with various concentrations of ligands for 72 hours. After the treatment, the cell viability of different cell lines was determined by MTT assay (ThermoFisher Scientific). Briefly, the cells after treatment with ligands for 72 hours, 10 μL of 5 mg/mL MTT was added to each well. The cells were incubated in an incubator at 37 °C with 5% CO_2 for 3 hours. After incubation, the medium was replaced with 100 μL of DMSO (ThermoFisher Scientific). The optical density (OD) of the plates was measured at 540 nm.

4.9. Confocal microscopy

4.9.1. Live cell imaging of ligands

HeLa cells were seeded on a 15 mm glass bottom culture dish (NEST Biotechnology) at a density of 5 x 10^4 cells/dish. After incubated for overnight, the cells were first stained with 5 μM ligand for 15 mins. The cells were washed with DMEM and then were treated with 2 μM Hoechst 33342 (ThermoFisher Scientific) for 10 min. After washing with medium for three times, the dishes were subjected to TCS SPE confocal microscope (Leica) for confocal imaging. Briefly, Hoechst 33342 and ligands were excited at 405 nm and 488 nm with lasers respectively. The emitted signals were recorded sequentially with a photomultiplier tubes (PMT) detector.

4.9.2. MitoTracker co-staining and live cell imaging

HeLa cells were seeded on a 15 mm glass bottom culture dish at a density of 7.5 x 10^4 cells/dish. After overnight incubation, the cells were first stained with 20 nM MitoTracker™ Deep Red (ThermoFisher Scientific) for 20 mins. Then, the cells were washed with DMEM for three times and were treat with 5 μM ligand for 15 mins. After washing the cells with DMEM for three times, the cells were incubated with 3 μM Hoechst 33342 (ThermoFisher Scientific) for 10 min. After washing with DMEM for three times, the dishes were subjected to TCS SPE confocal microscope

(Leica) for confocal imaging. Briefly, Hoechst 33342, ligands, and MitoTracker™ Deep Red were excited at 405 nm, 488 nm, and 635 nm with lasers, respectively. The emitted signals were recorded sequentially with a PMT detector.

4.9.3. RNase and DNase digestion assay

HeLa cells were seeded on a 15 mm glass bottom culture dish (NEST Biotechnology) at a density of 10 x 10^4 cells/dish. After overnight incubation, the cells were first washed with DMEM for three time. To the washed cells, it was first stained with 5 μM ligand for 15 mins. And then the cells were washed with PBS for three times and fixed with 4% paraformaldehyde for 30 mins at room temperature. The cells after being fixed were washed with PBS for another three times to remove the paraformaldehyde and treated with 200 units/mL RNase or DNase in PBS. The cells were then incubated at 37 °C for 2 hours. After enzyme digestion, the fixed cells were washed with PBS for three times. Then, the cells were stained with 2 μM DAPI (ThermoFisher Scientific) at room temperature for 10 mins. After washing with PBS for three times, the dishes were subjected to TCS SPE confocal microscope (Leica) for confocal imaging. Briefly, DAPI and ligands were excited at 405 nm and 488 nm with lasers respectively. The emitted signals were recorded sequentially with a PMT detector.

4.9.4. BG4 immunofluorescence co-localization assay

BG4 immunofluorescence co-localization assays were performed by applying anti-DNA/RNA G-quadruplex structures, clone BG4 antibody (EMD Millipore Corporation, Cat. # MABE917). Briefly, HeLa cells were seeded on a 15 mm glass bottom culture dish (NEST Biotechnology) at a density of 50 x 10^4 cells/dish. After overnight incubation, the cells were first washed with DMEM for three time. To the washed cells, it was first live stained with 5 μM ligand for 15 mins. And then the cells were washed with PBS for three times and fixed with 4% paraformaldehyde for 30 mins at room temperature. Subsequently, the cells were permeabilized by incubating in 0.3% Triton-X containing PBS for 1 hour in room temperature. After washing with PBS for three times, the cells

were further blocked with 1% BSA (with 0.3% triton-X in PBS). After that, the cells were directly incubated with BG4 antibody (1:750 in PBS containing 1%BSA and 0.3% triton-X) at 4 °C. After overnight incubation, the cells were first washed with ice-cooled PBS for 5 times and were incubated with rabbit anti-FLAG (CST#2368) in 1:1000 dilution (PBS containing 1% BSA and 0.3% triton-X) at room temperature for 2 hours. After secondary antibody incubation, the cells were washed with ice-cold PBS for 3 times. The cells were further incubated with goat anti-rabbit IgG Alexa Fluor 568 (ThermoFisher Scientific) in 1:1000 dilution (PBS containing 1%BSA and 0.3% triton-X100) for another 1.5 hours. After tertiary antibody incubation, the cells were washed with ice-cold PBS for 3 times. Then, the cells were stained with 2 μM DAPI at room temperature for 10 mins. After washing with PBS for three times, the dishes were subjected to TCS SPE confocal microscope (Leica) for confocal imaging. Briefly, DAPI, ligands, and Alexa Fluor 568 were excited at 405 nm, 488 nm, and 561 nm with lasers respectively. The emitted signals were recorded sequentially with a PMT detector.

4.9.5. Ki-67 immunofluorescence staining assay

Ki-67 immunofluorescence staining assays were performed by applying Ki-67 Rabbit Monoclonal Antibody (Beyotime, Cat. # AF1738). Briefly, HeLa cells were seeded on a 15 mm glass bottom culture dish (NEST Biotechnology) at a density of 50 x 10^4 cells/dish. After overnight incubation, the cells were first washed with DMEM for three time. To the washed cells, it was first live stained with 5 μM ligand for 15 mins. And then the cells were washed with PBS for three times and fixed with 4% paraformaldehyde for 30 mins at room temperature. Subsequently, the cells were permeabilized by incubating in 0.3% Triton-X containing PBS for 1 hour in room temperature. After washing with PBS for three times, the cells were further blocked with 1% BSA (with 0.3% triton-X in PBS). After that, the cells were directly incubated with Ki-67 antibody (1:1000 in PBS containing 1% BSA and 0.3% triton-X) at 4 °C. After overnight incubation, the cells were first washed with ice-cooled PBS for 5 times and were incubated with goat anti-rabbit IgG Alexa Fluor 647 (ThermoFisher Scientific) in 1:1000 dilution (PBS containing 1%BSA and 0.3% triton-X100)

for another 1.5 hours. After secondary antibody incubation, the cells were washed with ice-cold PBS for 3 times. Then, the cells were stained with 2 μM DAPI at room temperature for 10 mins. After washing with PBS for three times, the dishes were subjected to TCS SPE confocal microscope (Leica) for confocal imaging. Briefly, DAPI, ligands, and Alexa Fluor 647 were excited at 405 nm, 488 nm, and 635 nm with lasers respectively. The emitted signals were recorded sequentially with a PMT detector.

4.9.6. MitoSOX Red staining imaging

HeLa cells were seeded on a 15 mm glass bottom culture dish at a density 7.5 x 10^4 cells/dish. After overnight incubation, the cells were treated with different concentration of ligand (0, 5, 10, and 20 μM) for 24 hours at 37 °C with 5 % CO_2. The cells were then washed with DMEM for three times, and stained with 5 μM MitoSOX Red (ThermoFisher Scientific) for 10 min. After further washing with DMEM for three times, the cells were stained with 3 μM Hoechst 33342 (ThermoFisher Scientific). Subsequently, cells were washed with DMEM and subjected to TCS SPE confocal microscope (Leica) for confocal imaging. Hoechst 33342, and MitoSOX Red were excited at 405 nm and 488nm with lasers, respectively. The emitted signals were recorded sequentially with a PMT detector for analysis.

4.9.7. CellROX Deep Red staining imaging

HeLa cells were seeded on a 15 mm glass bottom culture dish at a density 7.5 x 10^4 cells/dish. After overnight incubation, the cells were treated with different concentration of ligand (0, 5, 10, and 20 μM) and tert-butyl hydroperoxide (TBHP; 200 μM) for 24 hours at 37 °C with 5 % CO_2. The cells were then washed with DMEM for three times, and stained with 5 μM CellROX Deep Red (ThermoFisher Scientific) for 30 min at 37 °C with 5 % CO_2. After further washing with DMEM for three times, the cells were stained with 3 μM Hoechst 33342 (ThermoFisher Scientific). Subsequently, cells were washed with DMEM and subjected to TCS SPE confocal microscope (Leica) for confocal imaging. Hoechst 33342 and CellROX Deep Red were excited at 405 nm and

635 nm with lasers, respectively. The emitted signals were recorded sequentially with a PMT detector for analysis.

4.9.8. TMRE staining imaging

HeLa cells were seeded on a 15 mm glass bottom culture dish at a density 7.5 x 10^4 cells/dish. After overnight incubation, the cells were treated with different concentration of ligand (0, 5, 10, and 20 μM) for 24 hours at 37 °C with 5 % CO_2. The cells were then washed with DMEM for three times, and stained with 1x TMRE (Beyotime) for 30 min. After further washing with DMEM for three times, the cells were stained with 3 μM Hoechst 33342 (ThermoFisher Scientific). Subsequently, cells were washed with DMEM and subjected to TCS SPE confocal microscope (Leica) for confocal imaging. Hoechst 33342, and TMRE were excited at 405 nm and 561 nm with lasers, respectively. The emitted signals were recorded sequentially with a PMT detector for analysis.

4.10. Flow cytometry

4.10.1. Apoptosis analysis

The apoptosis analysis was performed by Alexa Fluor 647 conjugated Annexin V (ThermoFisher Scientific). HeLa cells were seeded at a density of 10 x 10^4 cells/well in a 6-wells plate. After overnight incubation, the cells were treated with ligands at different concentration for 24 hours. After treatment, the cells were collected by trypsinization with 0.25% trypsin with EDTA and suspended in PBS. The cells were then stained with Alexa Fluor 647 conjugated Annexin V with Annexin V-PE Apoptosis Detection Kit (Beyotime) according to the manufacturer's instructions but replacing Annexin V-PE with Alexa Fluor 647 conjugated Annexin V. The stained cells were then subjected to flow cytometry (BD Accuri C6 flow cytometer) for apoptotic analysis.

4.10.2. Cell cycle analysis

The cell cycle analysis was performed by Cell Cycle and Apoptosis Analysis Kit (Beyotime). HeLa cells were seeded at a density of 20 x 10^4 cells/well in a 6-wells plate. After overnight incubation,

the cells were treated with ligands at different concentration for 24 hours. After the treatment, the cells were collected by trypsinization with 0.25% trypsin with EDTA and suspended in ice-cooled PBS. After centrifugation at 1500rpm for 5 mins to remove the supernatant, 1mL ice-cooled 70% Ethanol (in PBS) were added, mixed well, and incubated at 4 °C for 2 hours. After fixation, the cells were centrifuged at 3000 rpm for 5 min to remove supernatant. The cells were then stained with propidium iodide (PI) according to the manufacturer's instructions. The stained cells were subjected to flow cytometry (BD Accuri C6 flow cytometer) for cell cycle analysis.

4.11. Quantitative Real time RCR (qRT-PCR)

4.11.1. Total RNA extraction

HeLa cells were seeded on a 10 cm culture dish at a density of 100 x 10^4 cells/dish. After overnight incubation, the cells were treated with the ligand at different concentration for 48 hours. After the treatment, the cells were washed with PBS for three times. Then, 1 mL of Trizol solution (Beyotime) were added to the treated cells. The cells were mixed well with Trizol solution by pipetting up-and-down. The mixture was then incubated at 4 °C for 10 mins. After digestion, the mixture was transferred to a RNase-free 1.5 mL tube and 200 µL chloroform were added. The mixture was then mixed well by shaking vigorously until 2 portions were observed. The mixture was allowed to incubate at 4 °C for 15 mins. After incubation, the mixture was centrifuged at 12000 rpm for 15 mins at 4 °C. The upper transparent portion was then transferred into another RNase-free 1.5 mL tube and mixed with 500 µL isopropanol to precipitate the RNA. The mixture was mixed by flicking and was incubated at 4 °C for 10 mins. The supernatant was then removed by centrifuging at 12000 rpm for 10 mins at 4 °C. To the settled RNA pallet, 1 mL 70% ethanol (in DEPC water) was added and mixed well. The mixture was centrifuged again at 7500 rpm for 10 mins at 4 °C to remove the supernatant. 20-40 µL DEPC water were added to dissolve the extracted RNA. After quantifying the concentration by BioDrop Duo+ UV-Vis spectrophotometer (Biochrom), the RNA was stored at -80 °C before use.

4.11.2. qRT-PCR

The total RNA was diluted to 0.5 μg/μL. The qRT-PCR mixtures were done with BeyoFast™ SYBR Green One-Step qRT-PCR Kit (Beyotime) according to the manufacturer's instructions in which 2 μL 0.5 μg/μL RNA solution, 2 μL of 3 uM forward and reverse primer mixture solution, and low ROX were used in each PCR reaction. The RNA mixtures were then subjected to QuantStudio™ 5 Real-time PCR system (Applied Biosystems). The conditions of qRT-PCR were listed as follows: one cycle of 50 °C for 30 mins, followed by one cycle of 90 °C for 2 mins, followed with 40 cycles of 95 °C for 15 seconds, 60 °C for 30 seconds, and 72 °C for 30 seconds. All experiments were run in triplicate and the gene expression level was normalized with housekeeping gene GAPDH.

4.12. Western Blot

4.12.1. Protein extraction

HeLa cells were seeded on a 10 cm culture dish at a density of 100 x 10^4 cells/dish. After overnight incubation, the cells were treated with ligands at different concentration for 48 hours. After treatment, the cells were washed with PBS for three times, trypsinized, centrifuged, and resuspended in PBS to remove trace amount of trypsin. After that, centrifugation was performed again to remove supernatant and the cells were lyzed at 4 °C in RIPA buffer (Beyotime) supplemented with protease and phosphatase inhibitors (Beyotime) with sonication of 20 cycles of 15s sonication and 15s resting. Subsequently, the lysate was allowed to further incubate with RIPA buffer at 4 °C for 30 mins under rolling. The lysate was then centrifuged at 12000 rpm for 10 mins at 4 °C. The supernatant was transferred to another new 1.5 mL tube and the concentration of proteins was determined by Detergent Compatible Bradford Protein Assay Kit (Beyotime) according to the manufacturer's instructions. The proteins were then subjected to a heat plate for denaturing at 95 °C for 10 mins. Before loading of proteins, the proteins were aliquoted and stored in -80 °C.

4.12.2. Sodium dodecyl sulfate-polyacrylamide (SDS-PAGE) Gel preparation

The glasses were first wiped with ethanol solution. Then, the casting equipment was assembled such that the short plate was placed in front of the 1.0 mm spacer plates. Add water into the spacer to ensure that there is no leakage. The 12% (8%) separating gel was prepared by mixing 1.65 mL (2.3 mL) Milli-Q water, 2 mL (1.35 mL) 30% Acrylamide/Bis solution (Bio-rad), 1.25 mL 1.5M Tris-HCl (pH 8.8) (Beyotime), 100 μL 10% SDS (Beyotime), 100 μL 10% APS (dissolved in Milli-Q water) (Sigma-Aldrich), and 4 μL TEMED (Bio-rad). After removing the water from spacer, 4.7 mL separating gel solution was added into the spacer with 95% ethanol on top as cover and the unpolymerized gel was allowed to polymerize around 30-45 mins. After polymerization, the 95% ethanol was poured out and trace of it was removed with tissue paper. The stacking gel was prepared by mixing 1.05 mL Milli-Q water, 0.25 mL 30% Acrylamide/Bis solution, 0.19 mL 1.0M Tris-HCl (pH 6.8), 15 μL 10% SDS, 15 μL 10% APS, and 1.5 μL TEMED. Then, the stacking gel solution was added on top of the polymerized separating gel as soon as prepared to the top of the spacer. A 10-wells comb was inserted into the stacking gel and then the gel was allowed to polymerize for around 30-45 mins. After polymerization, the comb was removed vertically. The gel was then wrapped by plastic wrap filled with small volume of SDS-PAGE running buffer (Bio-Rad; 25 mM Tris, 192 mM glycine, 0.1% SDS, pH 8.3) and was store in 4 °C before use.

4.12.3. SDS-PAGE gel electrophoresis

For the protein samples, equal amounts of proteins (20 μg of proteins were used for most of the Western blotting experiments; 5 μg of proteins were used for PARP-1 blotting; and 40 μg of proteins were used for cleaved caspase 3 blotting) were mixed with 4x Laemmli sample buffer (Bio-Rad) (added with reducing agent β-mercaptoethanol) and boiled for 10 mins at 95 °C. Subsequently, the samples were loaded on the SDS-PAGE (prepared in section 2.8.2). The samples were first stacked by electrophoresis at 60 V for 30 mins in running buffer (Bio-Rad; 25 mM Tris, 192 mM glycine, 0.1% SDS, pH 8.3). After stacking, the samples were separated by electrophoresis at 150 V for 1-1.5 hours in the same running buffer

4.12.4. Immunoblotting

Upon completion of SDS-PAGE gel electrophoresis, the gel was separated from the spacer and immersed into Western Transfer Buffer (Beyotime). The 0.2 μm PVDF membrane (Beyotime) was first activated with Soaking and Activation Buffer for PVDF Membrane (Beyotime) for 5 mins and was rinsed with Western Transfer Buffer (Beyotime) for 2 times. The transfer stack was assembled from bottom to high as follow: black side of cassette-2 foam pads-filter paper-gel-activated PVDF membrane-filter paper-2 foam pads-transparent side of cassette. After placed the transfer stack to the tank, cooling unit and transfer buffer were put into the chamber. The proteins were transferred from gel to PVDF membrane at a constant voltage of 150 V for 1-2 hours. To prevent the overheat during protein transfer, ice was added to surround the tank within a foam box. Upon completion of protein transfer, the PVDF membrane was took out and rinsed in TBST (20 mM Tris, pH 7.5, 150 mM NaCl, and 0.1% Tween 20). Subsequently, the PVDF membrane was cut according to the molecular weight of target proteins. The PVDF membranes were then rinsed in TBST for 10 min for three times and blocked with 5% skim milk (Beyotime) (in TBST) for 2 hours in room temperature. After blocking, membranes were incubated with the primary antibodies (diluted in 5% BSA containing TBST) at 4 °C overnight. Primary antibodies used were listed as follow: TRF2 (Abcam, ab108997), NRAS (Abcam, ab300431), gamma H2A.X (phospho S139) (Abcam, ab22551), phospho-p53 (Ser15) (ThermoFisher, MA5-15229), PARP-1 (CST#9532), cleaved Caspase-3 (CST#9664),and beta Actin (Abcam, ab8226). The concentrations of primary antibodies were prepared based on the recommendation of the manufacturer. After incubation and repeated washing with TBST at room temperature for 5 mins three times, membranes were incubated with Goat anti-Rabbit IgG (H+L), horseradish peroxidase (HRP)-conjugated secondary antibody (ThermoFisher Scientific #65-6120) or Goat anti-Mouse IgG (H+L), horseradish peroxidase (HRP)-conjugated secondary antibody (ThermoFisher Scientific #62-6520) for 2 hours. After incubation, membranes were extensively washed with TBST for three times and subjected to chemiluminescence detection using BeyoECL Star (Beyotime) according to the manufacturer's instructions under ChemiDoc MP Integrated Imaging System (Bio-rad).

4.13. β-Galactosidase (SA-β-gal) staining of cell senescence

HeLa cells were seeded at a density of 20 x 10^4 cells/well in a 6-wells plate. After overnight incubation, the cells were treated with the ligand at different concentration (0, 5, 10, and 20 μM) and 3 μM BRACO-19 as a positive control. Then, the HeLa cells were incubated for 3 and 6 days. The medium containing different concentrations of ligands and BRACO-19 was changed every 3 days. After incubation, Then, the medium was discarded, and the cells were washed with PBS for 3 times. The cells were then performed the SA-β-gal staining with Senescence β-Galactosidase Staining Kit (Beyotime) according to the manufacturer's instructions. After staining, the cells were first rinsed with 70% ethanol (in PBS) followed by two PBS washing. The cells were then subjected to Primovert Inverted Microscope (Zeiss) for imaging.

4.14. Statistical test

Statistical analysis was done by one-way ANOVA with Tukey as statistical hypothesis test using GraphPad Prism. All bioassays were repeated at least three times ($N \geq 3$, mean ± S.D.); (*) $P < 0.05$, (**) $P < 0.01$ and (***) $P < 0.001$, significantly different from each data set; ns, not significantly different from each data set.

Chapter 5. Conclusion

In the present study, eighteen new fluorescent G4-ligands were synthesized and characterized. A series of assays was performed to investigate their selectivity, cytotoxicity, the cellular localization of ligands and the influence on cellular activity against cancers by targeting *NRAS* mRNA G4s.

In term of the criteria to design the functional fluorescent ligands targeting RNA G4s, it was found that increasing the overall polarity of the ligands may benefit the interaction between the ligands and RNA G4s. Among all the side groups, it was also found that carboxylic side group may have higher selectivity to RNA G4s. This may be due to the low selectivity of carboxylic group to double-stranded DNA. This phenomenon can be explained by the repulsion force between the negatively charged carboxylic ion and the negative charged triphosphate groups surrounded groove of double-stranded DNA. As it may lower the driving force to drive the ligands into the double-stranded DNA rich nucleus, ligands may stay in the cytoplasm to interact with the RNA G4s.

Among the ligands, **B3C** was identified to show a high selectivity toward RNA G4s than DNA G4s and dsDNA. The ligand also exhibited a low IC_{50} against human cervix cancer HeLa cells (6.5 μM) while a relatively high IC_{50} against non-cancer human cell line, HFF1 (>50 μM). The results indicate that this new RNA G4-ligand shows a certain degree of cytotoxicity selectivity. Moreover, the binding studies including UV-Vis titration, CD melting study and ITC analysis reveal that **B3C** may induce and stabilize the RNA G4-structure upon interaction. The binding affinity ranged from 4.54 to 40.7 μM toward different RNA G4-substrates was obtained. Furthermore, confocal cell imaging studies including live cell imaging, enzymatic digestion assays and BG4 co-localization assays showed that **B3C** was primarily localized in cytoplasm but not nucleus and it most likely interacted with the cellular RNA G4s to generate strong emissive interaction signals and the interaction probably induced anticancer activity against a panel of human cancer cells.

The anticancer mechanism of **B3C** targeting NRAS mRNA G4s in HeLa cells was investigated. The result obtained from western blot and qRT-PCR showed that **B3C** inhibited the translation of NRAS protein while the ligand showed no significant effects on gene transcription because the ligand was RNA selective and primarily located in cytoplasm. Moreover, the DNA damage marker (γ-H2AX), S phase arresting, and apoptosis were significantly induced in a dose-dependent manner by **B3C** in HeLa cells. In addition, SA-β-gal assays and Ki-67 immunofluorescent imaging assays were conduced to study the possible pathway of cell growth inhibition with the ligand. It was found that **B3C** showed no significant effect on inducing senescence but suppressed the cellular proliferation. This finding is in a alignment witih the function of NRAS that is a signal transduction for cell proliferation. It is reported that the expression of RAS protein in cancer cells may abrogate the DNA damage repair (DDR) by suppressing the phosphorylation of p53 despite the existing of chromosomal instability. In order to study the mechanism on the upregulation of γ-H2AX caused by **B3C**, confocal imaging was performed to evaluate the formation of ROS that may be caused by **B3C**. The result showed that the treatment of **B3C** may not induce ROS in HeLa cells. On the other hand, the expression of phosphorylated p53 was studied through western blot, and the result showed that more p53 were phosphorylated after **B3C** treatment. The phos-p53 may then activate the DDR. Therefore, the upregulation of γ-H2AX in the HeLa cells treated with **B3C** is most likely attributed to the restoring of DDR pathway via downregulating the expression of NRAS by the ligand, **B3C**, that targets *NRAS* mRNA G4s. The activated DDR prolong the S phase in cell cycle in order to get more time to repair the damaged DNA in the cells. This thus causes S phase arresting and inhibits the cell proliferation. Ultimately, apoptosis is induced. The present study demonstrated the use of a novel fluorescent ligand to selectively target the cellular *NRAS* mRNA G4s with strong affinity and followed to induce anticancer effects. The finding provides experimental evidence for an anticancer pathway via the re-activation of DDR against RAS-driven cancers. Our results may also provide significant insight into the molecular design of potent and specific anticancer drugs targeting RNA G4-structures.

Nonetheless, the bioavailability of **B3C** such as water solubility could be further improved because this may restrict the application. Secondly, the binding affinity of the ligand targeting RNA G4s could be further enhanced in order to achieve higher anticancer potency. Some functional group such as pyrrolidine, piperidine, piperazine, and morpholine could be adapted for structural modification of the ligand as some studies have reported that these groups may increase the binding affinity to G4-structures.[23, 30, 48, 111] Moreover, despite **B3C** was found effective against several cancer cell lines, its *in vivo* efficacy need to be further investigated. Therefore, the future study of the project would be focused on the optimization of the ligand to increase its water solubility and binding affinity to RNA G4-structure. Furthermore, cellular based assays such as dual luciferase assays and RNA immunoprecipitation could be performed to further verify the targeting sequence and the mechanism of translational inhibition. Last but not least, *in vivo* experiment such as animal study may be applied to access the efficacy of the ligand against RAS-driven cancers.

Appendix

List of Contents

Figure S19. UV-vis, fluorescent excitation and fluorescent emission spectra of **B3C**.

Figure S20. Fluorescent titration spectra of **B3C** to *NRAS* RNA-G4 substrate and the fitted binding curve of **B3C** with *NRAS* RNA G4 substrate.

1. List of Supporting Table

Table S1. Sequences of oligonucleotides used in the present study.

Abbreviation	Sequence (5' to 3')	Origin [a]
Telo21	GGGTTAGGGTTAGGGTTAGGG	Telomere DNA G4
22AG	AGGGTTAGGGTTAGGGTTAGGG	Telomere DNA G4
Pu27	TGGGGAGGGTGGGGAGGGTGGGGAAGG	Promotor DNA G4
c-KIT	CGGGCGGGCGCGAGGGAGGGG	Promotor DNA G4
Ds26	CAATCGGATCGAATTCGATCCGATTG GTTAGCCTAGCTTAAGCTAGGCTAAC	Double-stranded DNA
Da21	AAAAAAAAAAAAAAAAAAAA	Single-stranded DNA
TERRA	GGGUUAGGGUUAGGGUUAGGG	Telomere RNA G4
TRF2	CGGGAGGGCGGGGAGGGC	5'-UTR mRNA G4
NRAS	AGGGAGGGGCGGGUCUGGG	5'-UTR mRNA G4
KRAS	GGCGGCGGCAGUGGCGGCGG	5'-UTR mRNA G4
VEGF	GGAGGAGGGGGAGGAGGA	5'-UTR mRNA G4
HP	CAGUACAGAUCUGUACUG	RNA Hairpin

[a] The structure was confirmed by circular dichroism (Section 4.6.1)

Table S2. Sequences of primers used in the present study.

Primer	Sequence (5' to 3')
TERRA-Forward	AAAGCGGGAAACGAAAAGC
TERRA-Reverse	GCCTTGCCTTGGGAGAATCT
TRF2-Forward	ACTCCAGCCTTGACCCACTC
TRF2-Reverse	TCCCAAAGTACCCAAAGGC
NRAS-Forward	CAGAGGCAGTGGAGCTTGA
NRAS-Reverse	GCTTTTCCCAACACCACCT
GAPDH-Forward	GGGAAACTGTGGCGTGAT
GAPDH-Reverse	GAGTGGGTGTCGCTGTTGA

Table S3. Spectroscopic data of ligands

Ligand	Absorbance (nm)	λ_{ex} (nm)	λ_{em} (nm)	Stokes Shift (nm)
B1S	422	418	560	142
B2S	423	426	561	135
B3S	421	427	561	134
B1N	516	530	593	63
B2N	526	544	597	53
B3N	517	531	594	63
B1I2C	450	464	535	71
B2I2C	449	463	550	87
B3I2C	449	461	543	82
B1I3C	455	460	510	50
B2I3C	459	463	516	53
B3I3C	455	459	516	57
B1C	458	473	591	118
B2C	465	472	584	122
B3C	459	470	587	117
B1Cou	530	560	641	81
B2Cou	544	575	646	71
B3Cou	534	575	650	75

2. List of Supporting Figures and Graphs

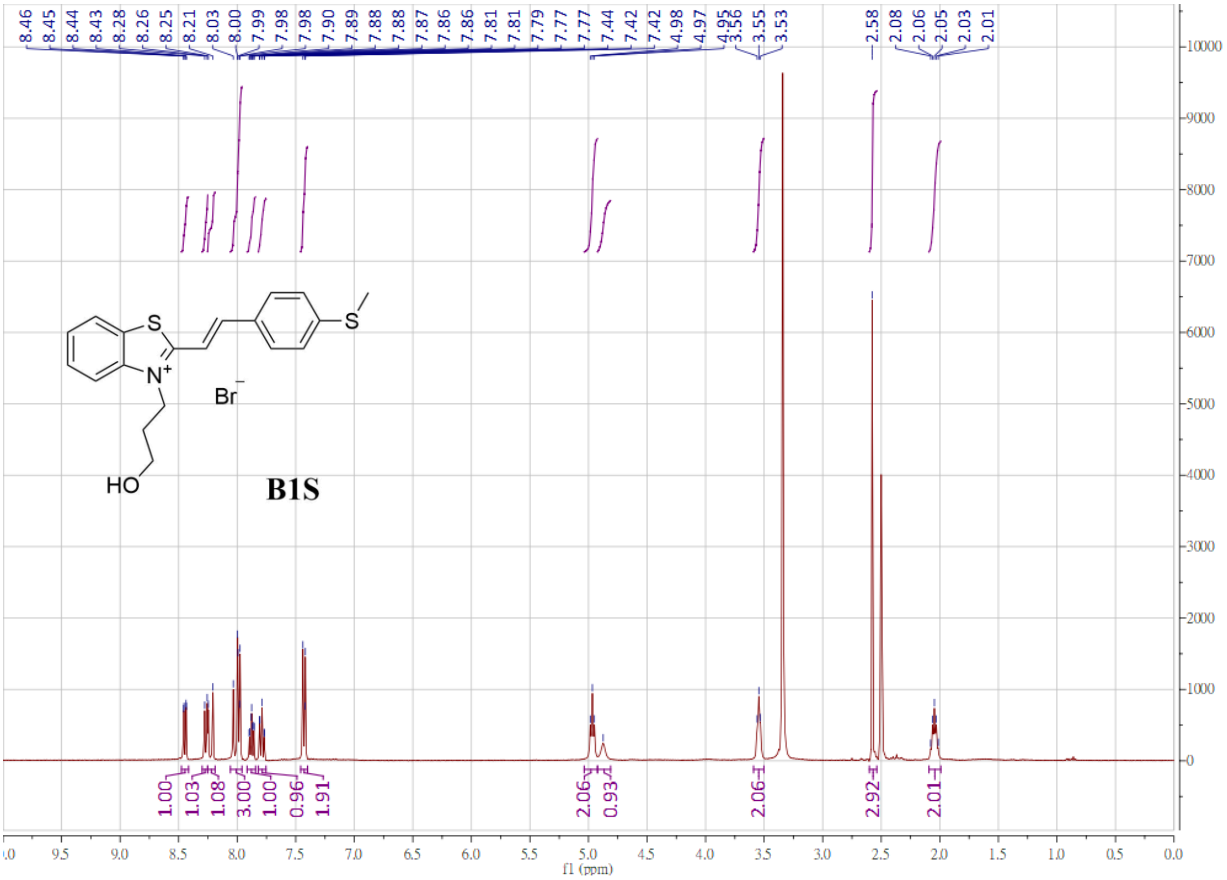

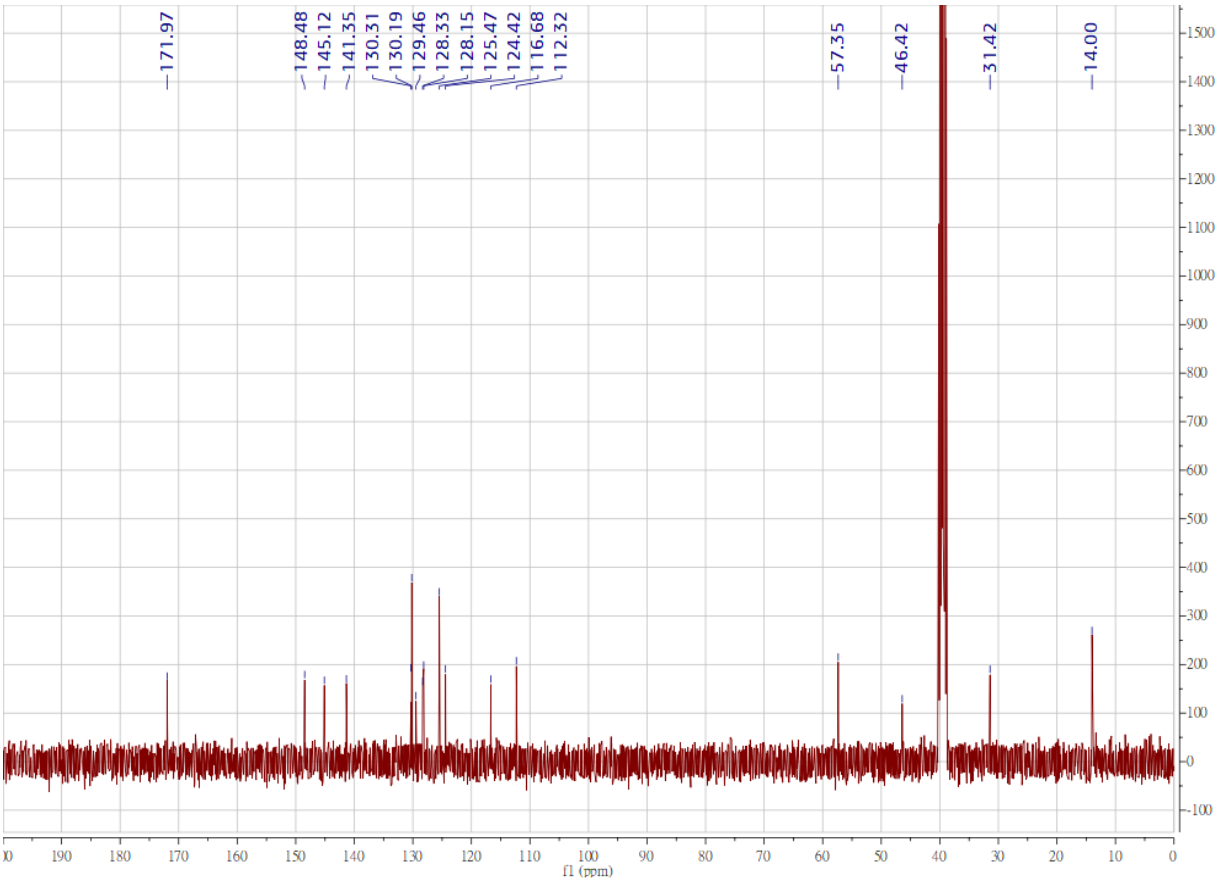

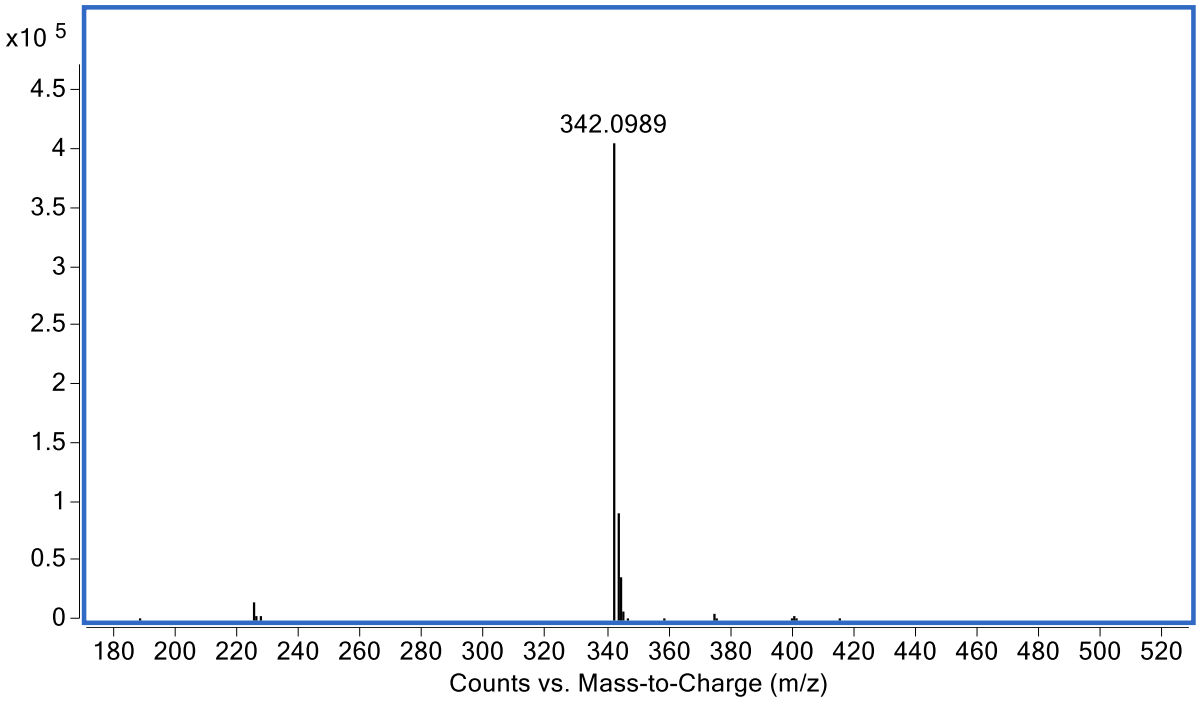

Figure S1. ^{1}H NMR, ^{13}C NMR and HRMS of **B1S**.

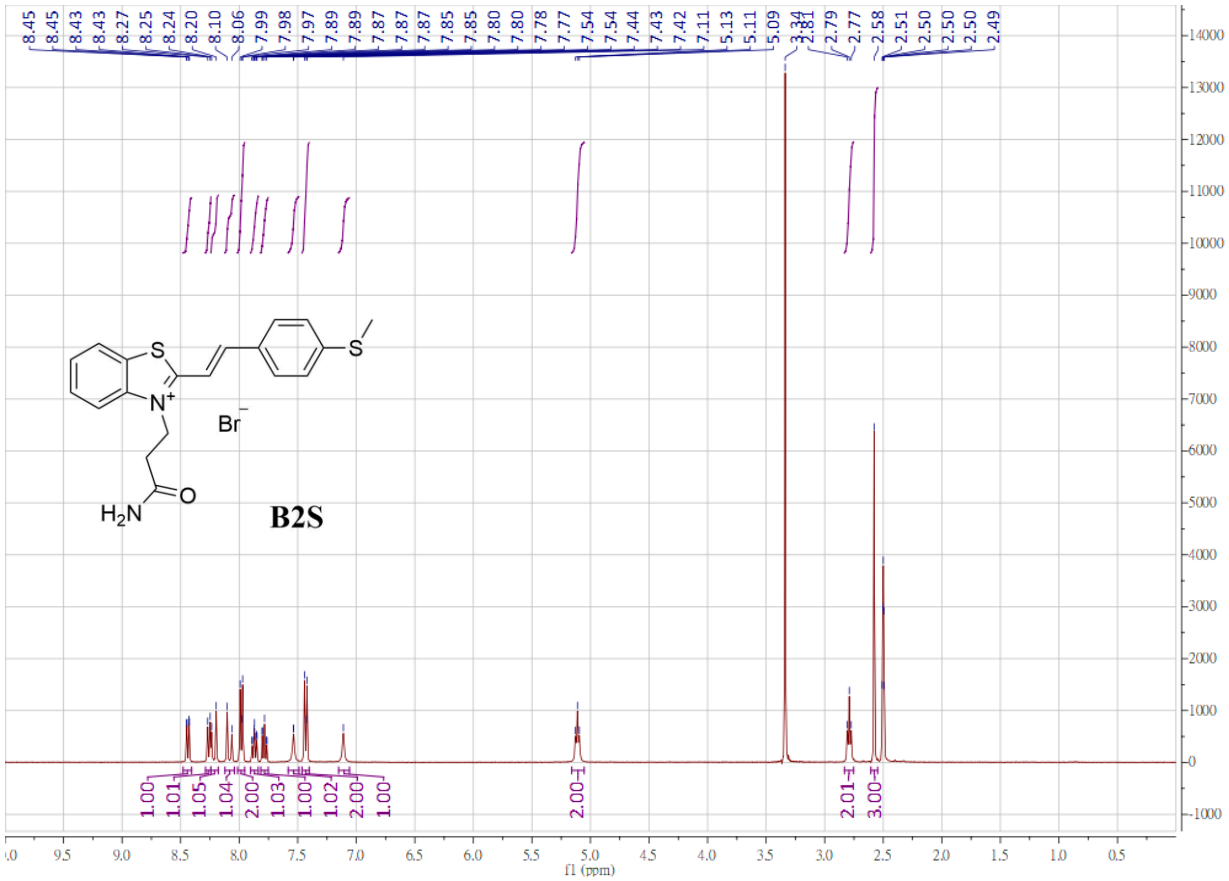
B2S
f1 (ppm)

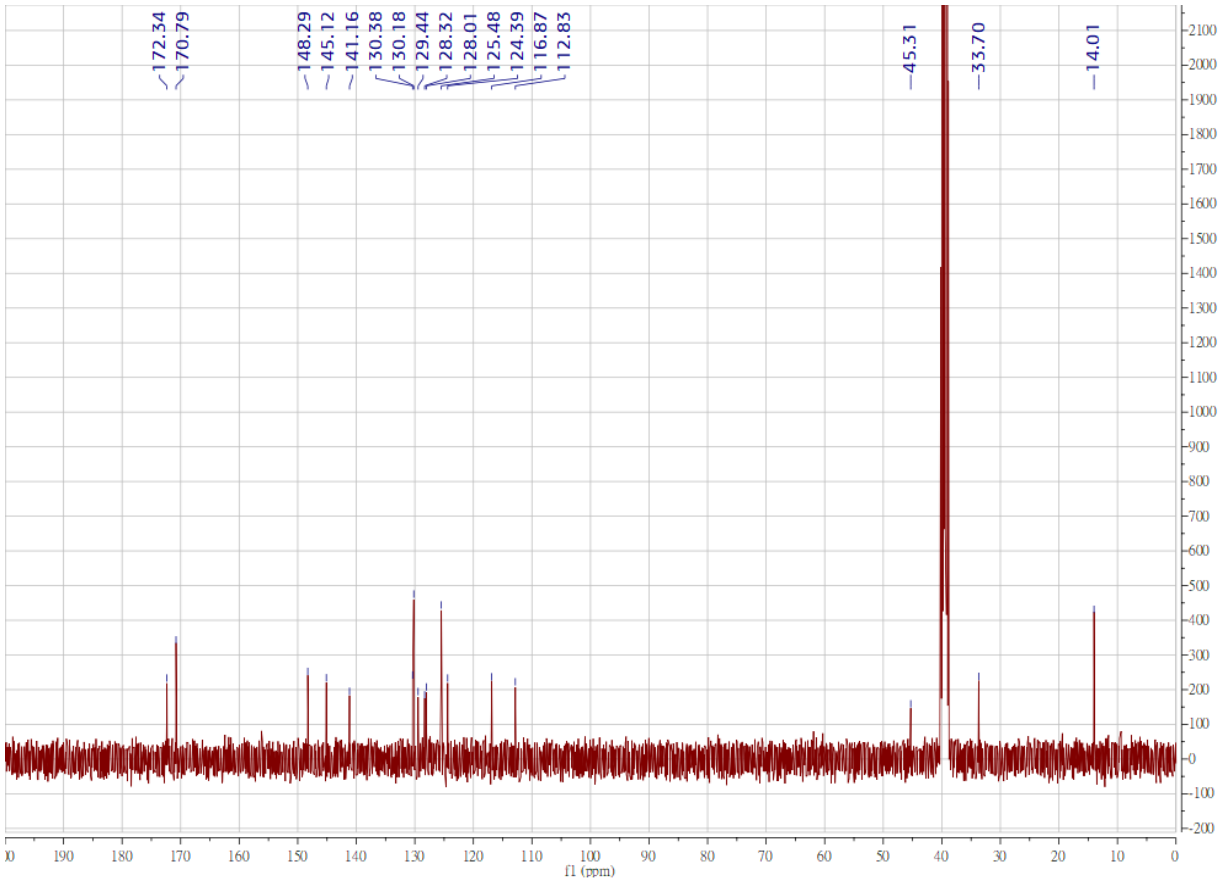
f1 (ppm)

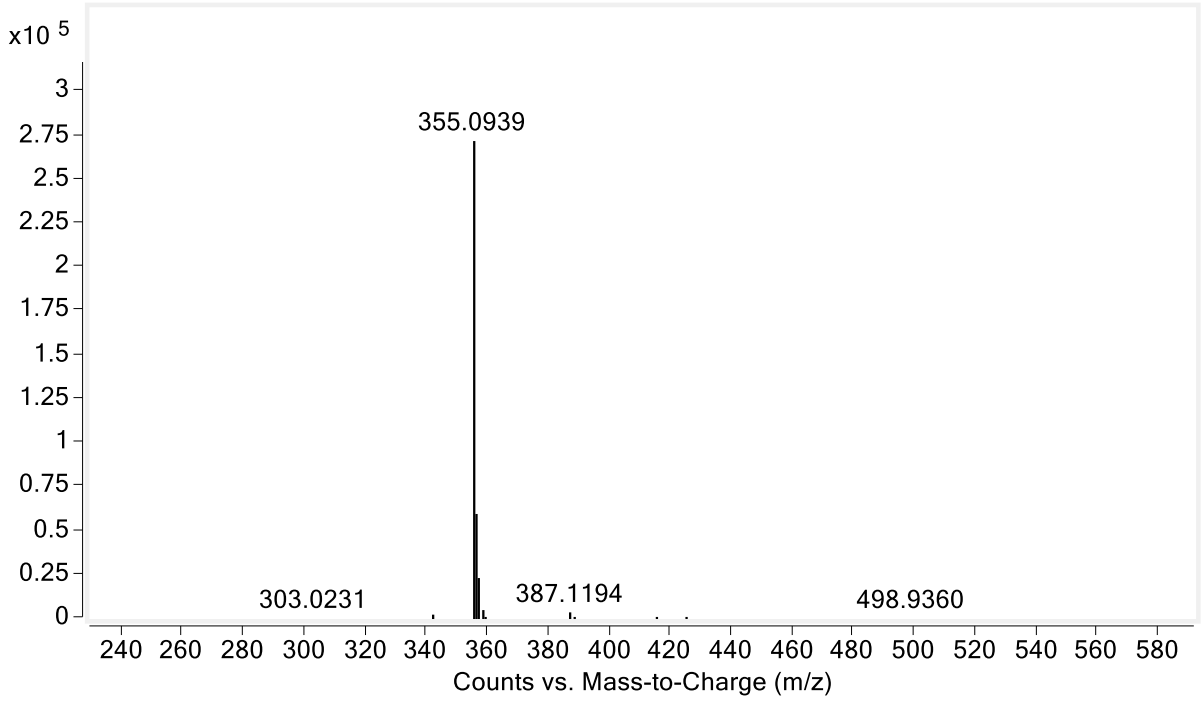

Figure S2. ^{1}H NMR, ^{13}C NMR and HRMS of **B2S**.

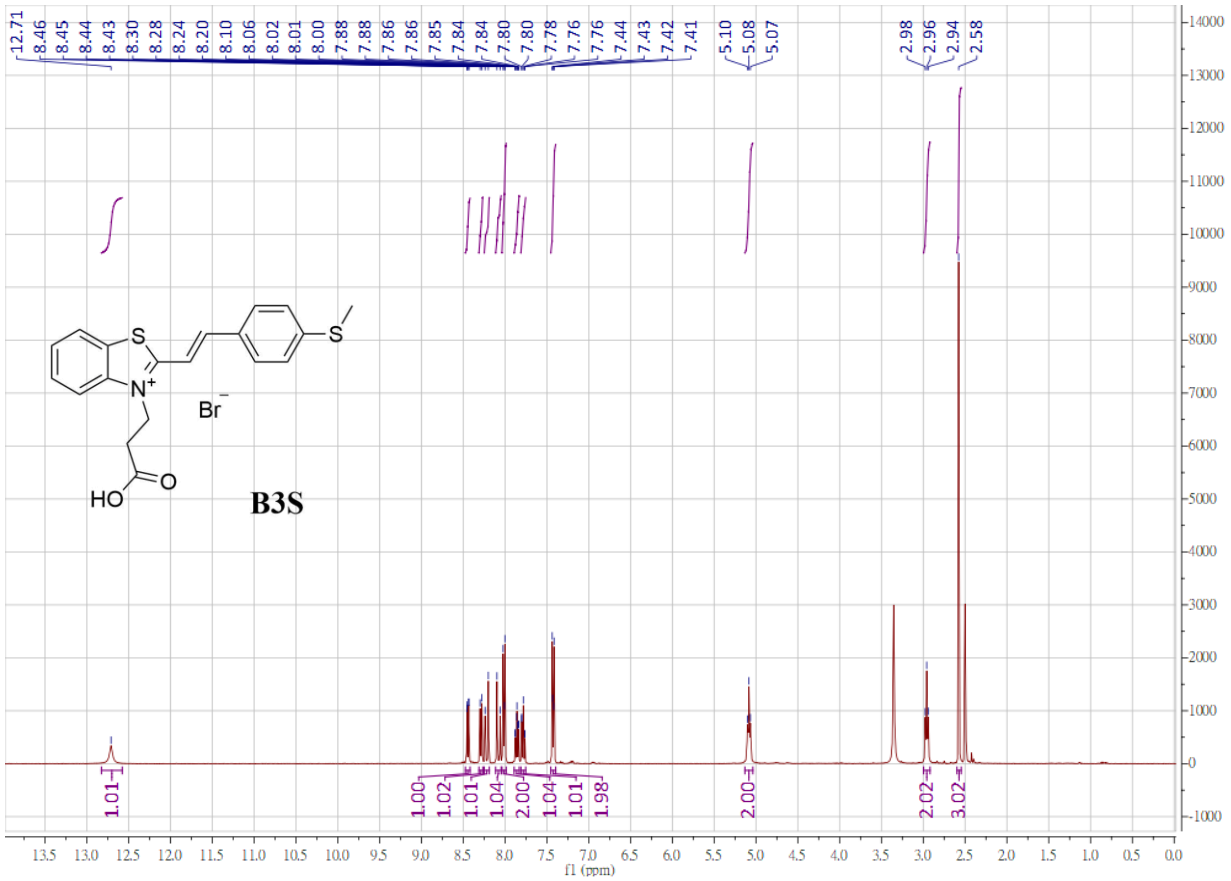
12.71
8.46
8.45
8.44
8.43
8.30
8.28
8.24
8.20
8.10
8.06
8.02
8.01
8.00
7.88
7.88
7.86
7.86
7.85
7.84
7.84
7.80
7.80
7.78
7.76
7.76
7.44
7.43
7.42
7.41
5.10
5.08
5.07
2.98
2.96
2.94
2.58
S
S
N+
Br−
HO
O
B3S
1.01
1.00
1.02
1.01
1.04
2.00
1.04
1.01
1.98
2.00
2.02
3.02
f1 (ppm)

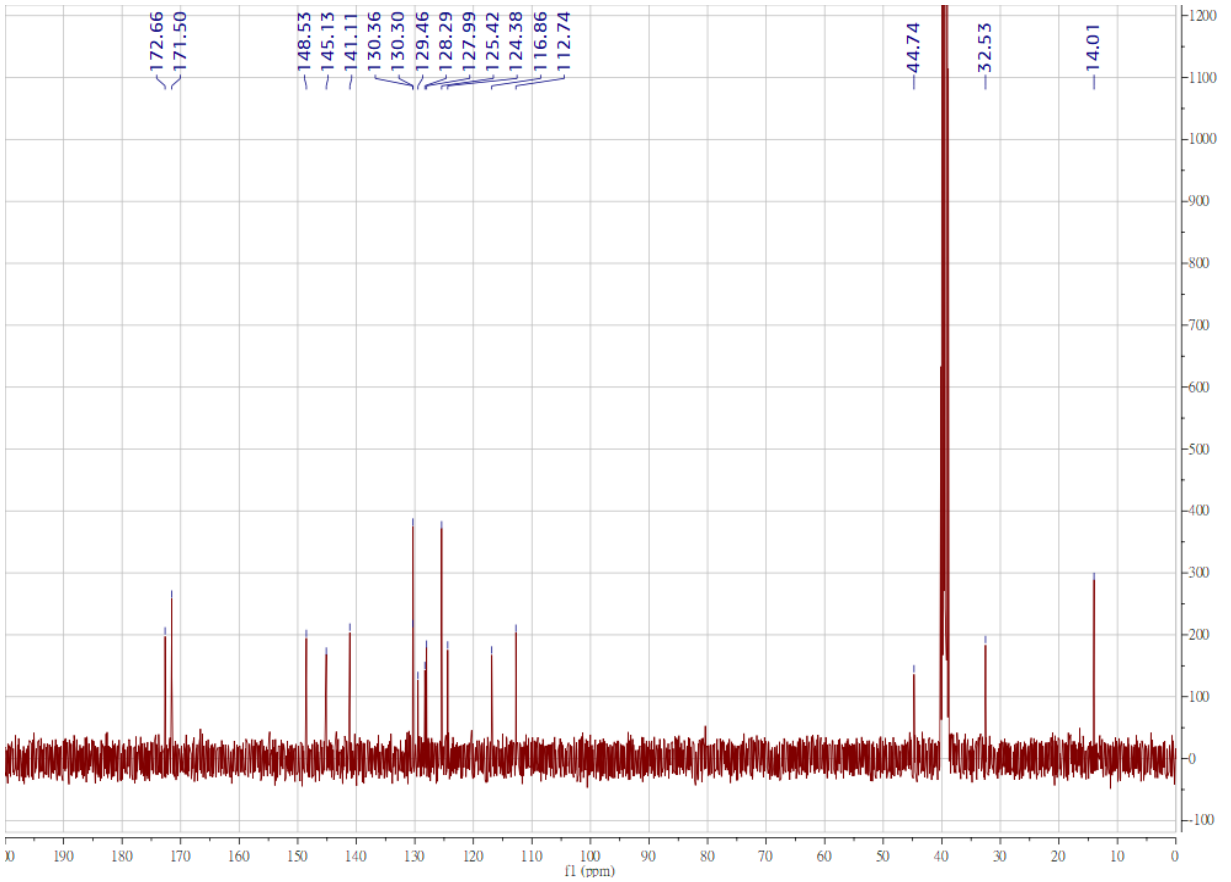
172.66
171.50
148.53
145.13
141.11
130.36
130.30
129.46
128.29
127.99
125.42
124.38
116.86
112.74
44.74
32.53
14.01
f1 (ppm)

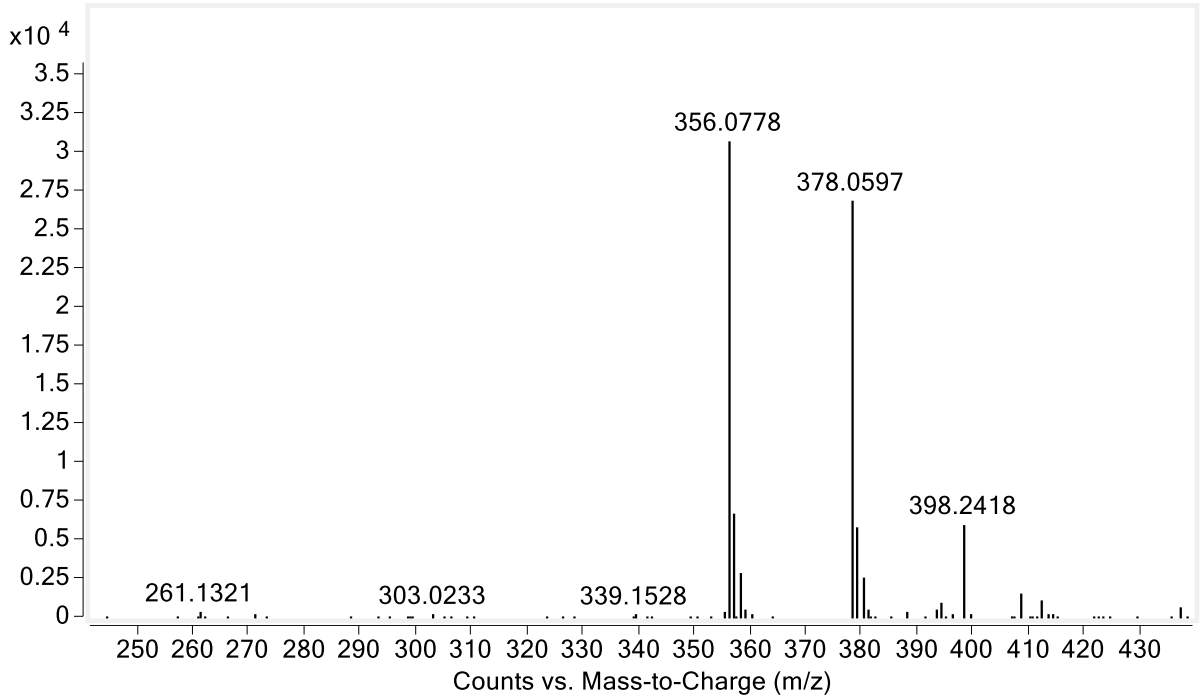

Figure S3. ^{1}H NMR, ^{13}C NMR and HRM, of **B3S**.

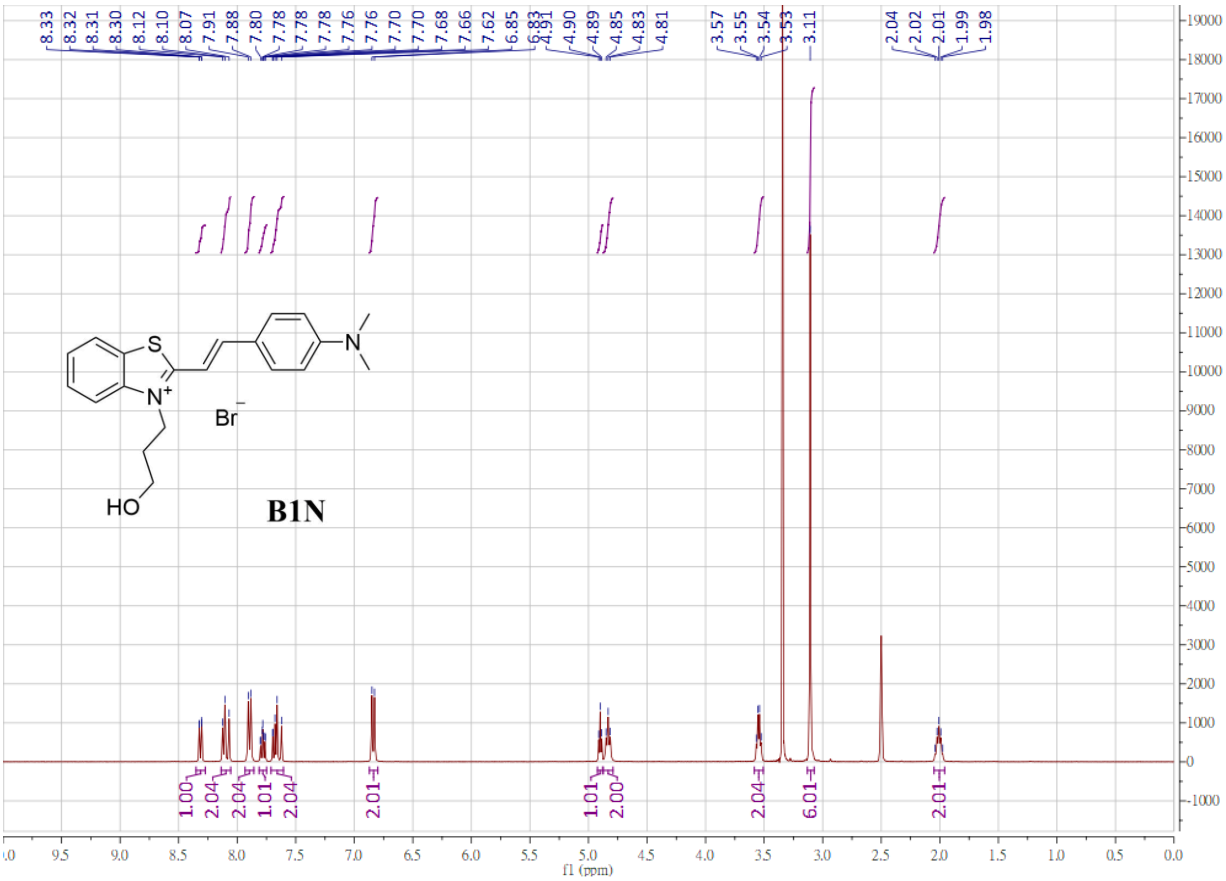
8.33
8.32
8.31
8.30
8.12
8.10
8.07
7.91
7.88
7.80
7.78
7.78
7.78
7.76
7.76
7.70
7.70
7.68
7.66
7.62
6.85
6.83
4.91
4.90
4.89
4.85
4.83
4.81
3.57
3.55
3.54
3.53
3.11
2.04
2.02
2.01
1.99
1.98
S
N+
Br−
N
HO
B1N
1.00
2.04
2.04
1.01
2.04
2.01
1.01
2.00
2.04
6.01
2.01
f1 (ppm)

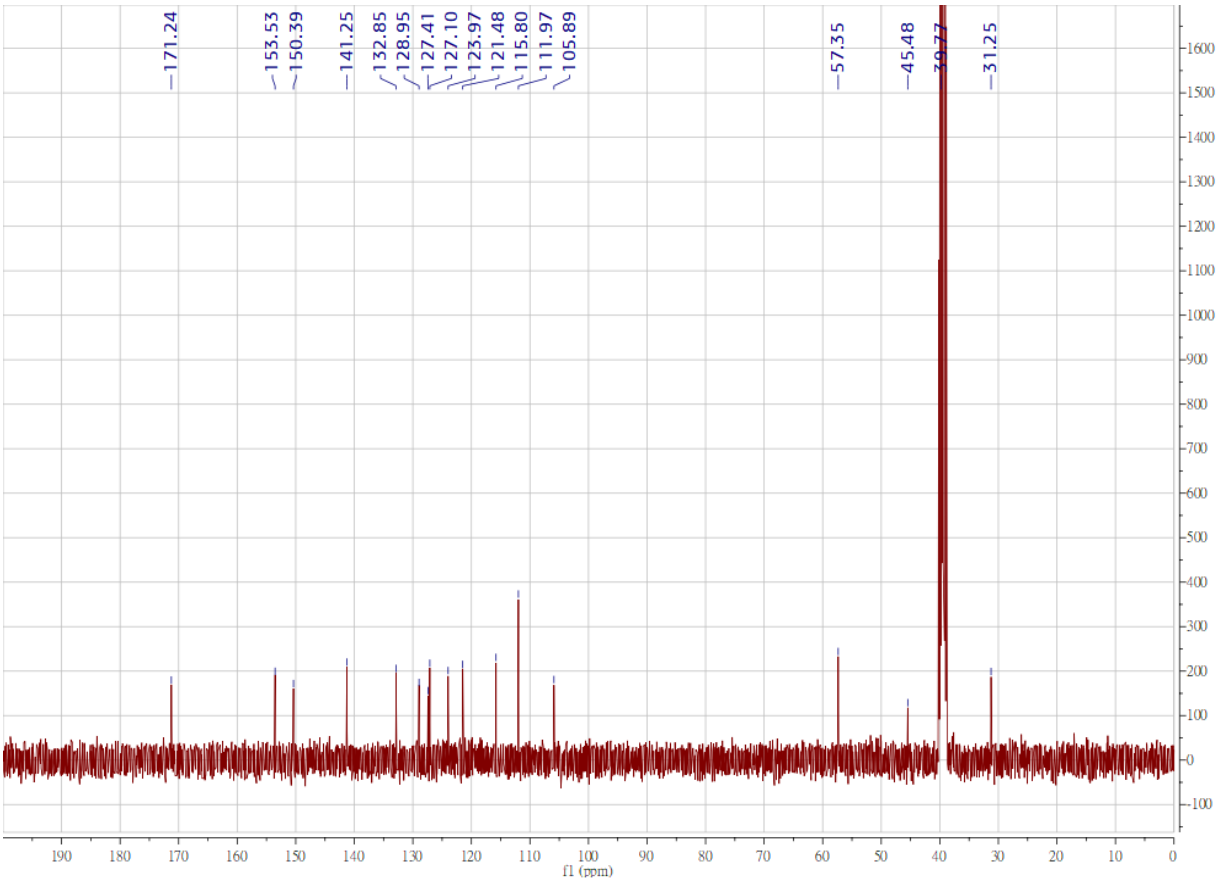
171.24
153.53
150.39
141.25
132.85
128.95
127.41
127.10
123.97
121.48
115.80
111.97
105.89
57.35
45.48
39.77
31.25
f1 (ppm)

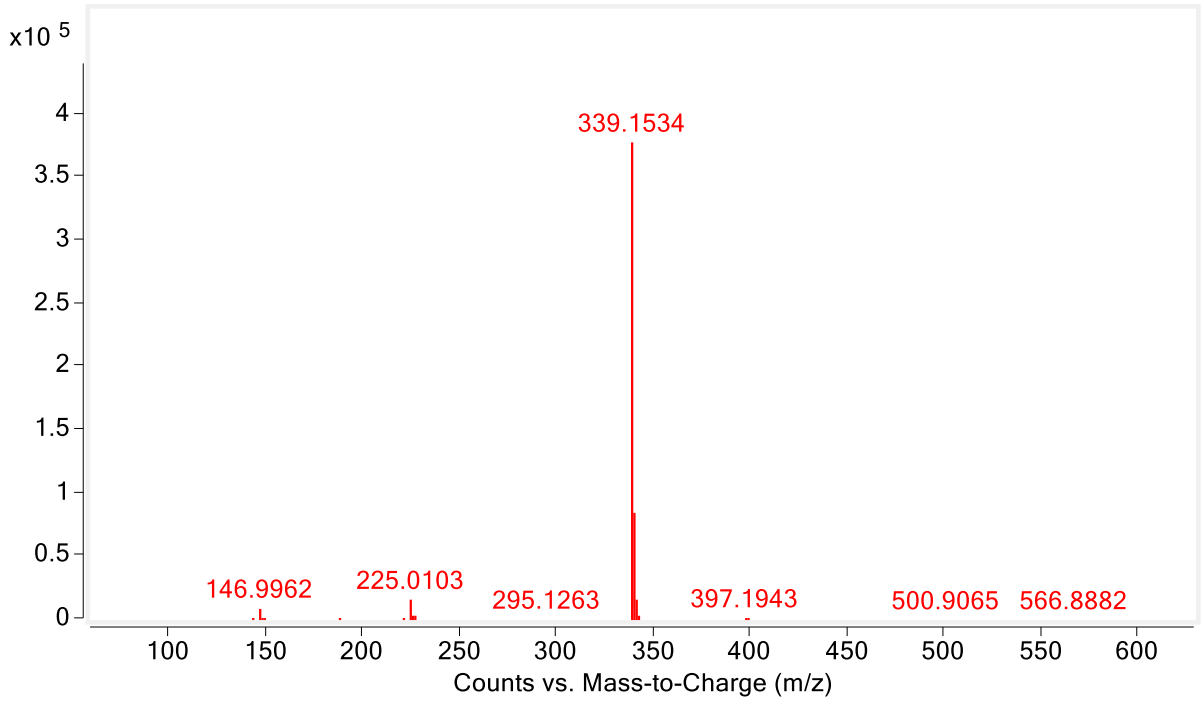

Figure S4. ^{1}H NMR, ^{13}C NMR and HRMS of **B1N**.

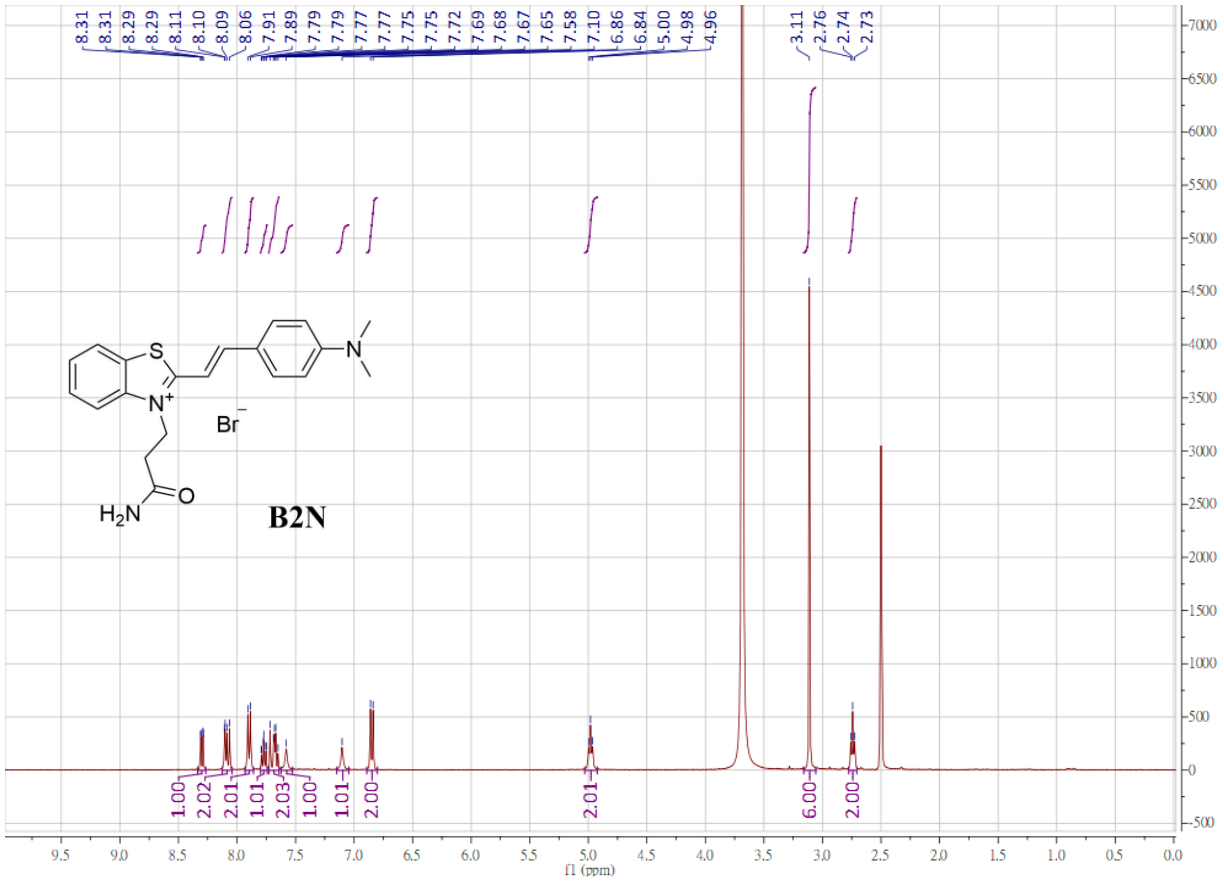
8.31
8.31
8.29
8.29
8.11
8.10
8.09
8.06
7.91
7.89
7.79
7.79
7.77
7.77
7.75
7.75
7.72
7.69
7.68
7.67
7.65
7.58
7.10
6.86
6.84
5.00
4.98
4.96
3.11
2.76
2.74
2.73
S
N+
Br−
N
O
H2N
B2N
1.00
2.02
2.01
1.01
2.03
1.00
1.01
2.00
2.01
6.00
2.00
f1 (ppm)

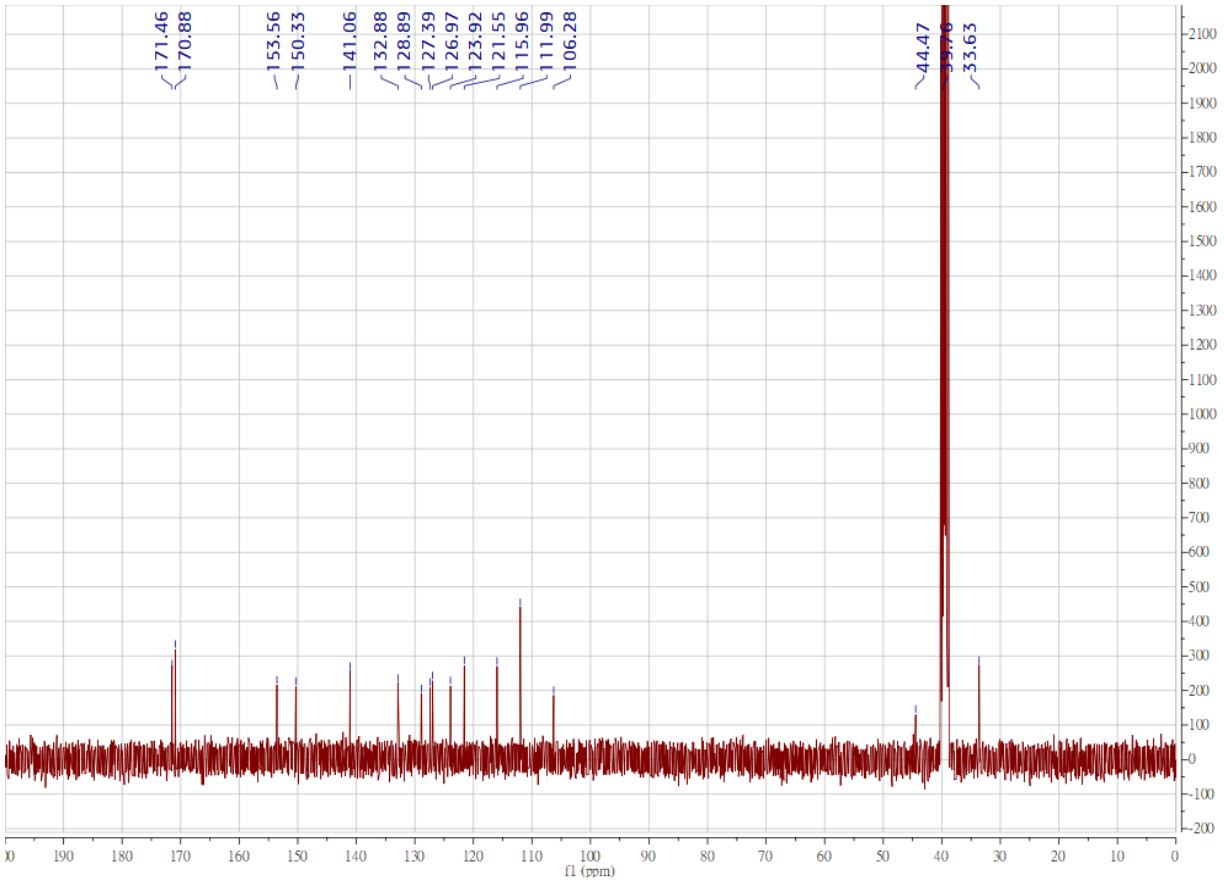
171.46
170.88
153.56
150.33
141.06
132.88
128.89
127.39
126.97
123.92
121.55
115.96
111.99
106.28
44.47
39.76
33.63
f1 (ppm)

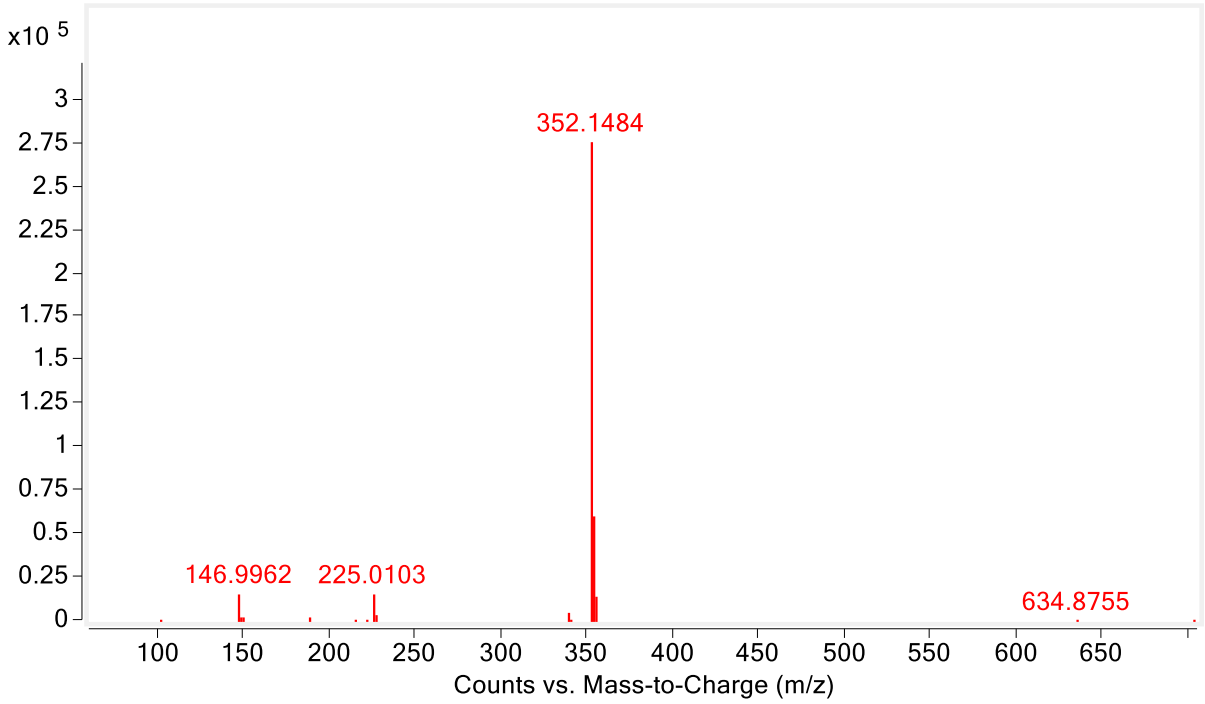

Figure S5. ^{1}H NMR, ^{13}C NMR and HRMS of **B2N**.

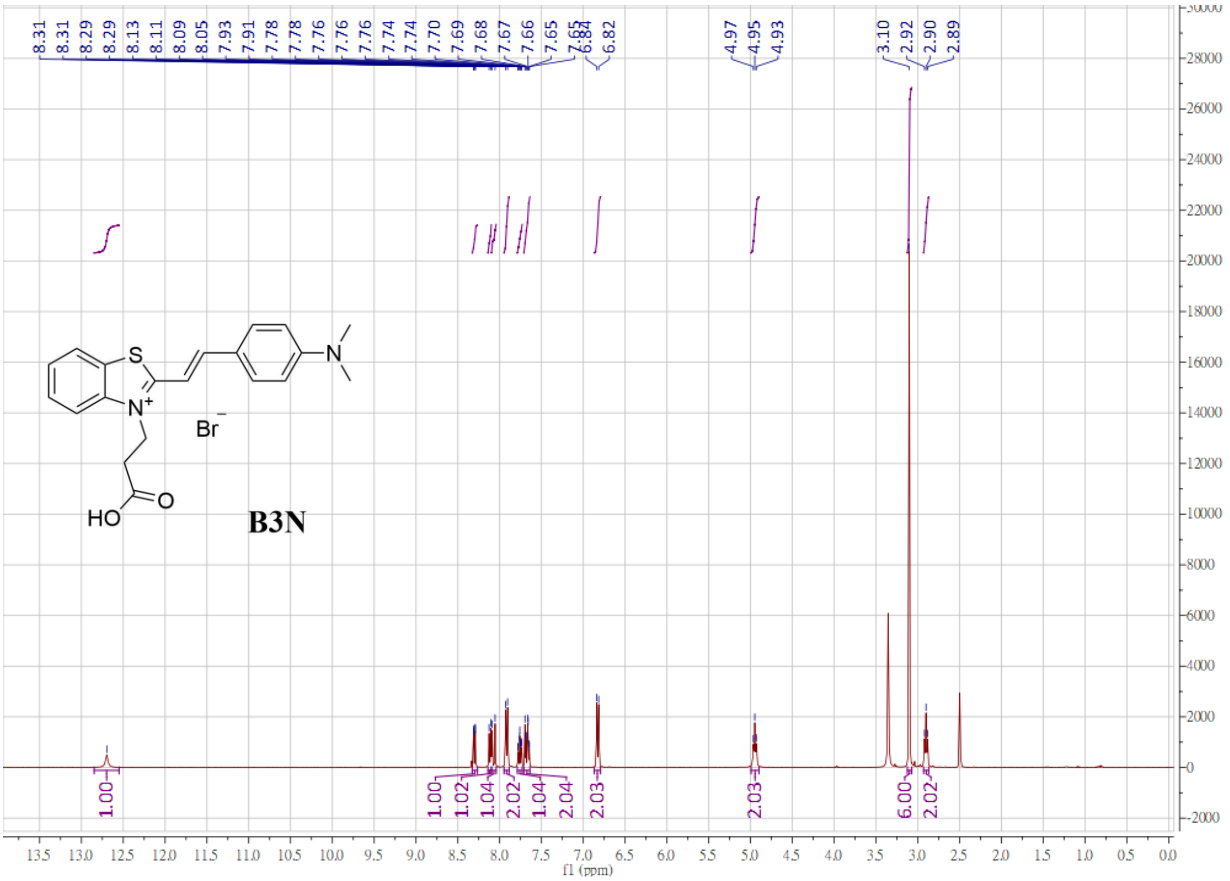
8.31
8.31
8.29
8.29
8.13
8.11
8.09
8.05
7.93
7.91
7.78
7.78
7.76
7.76
7.74
7.74
7.70
7.69
7.68
7.67
7.66
7.65
6.84
6.82
4.97
4.95
4.93
3.10
2.92
2.90
2.89
S
N
N+
Br−
HO
O
B3N
1.00
1.00
1.02
1.04
2.02
1.04
2.04
2.03
2.03
6.00
2.02
f1 (ppm)

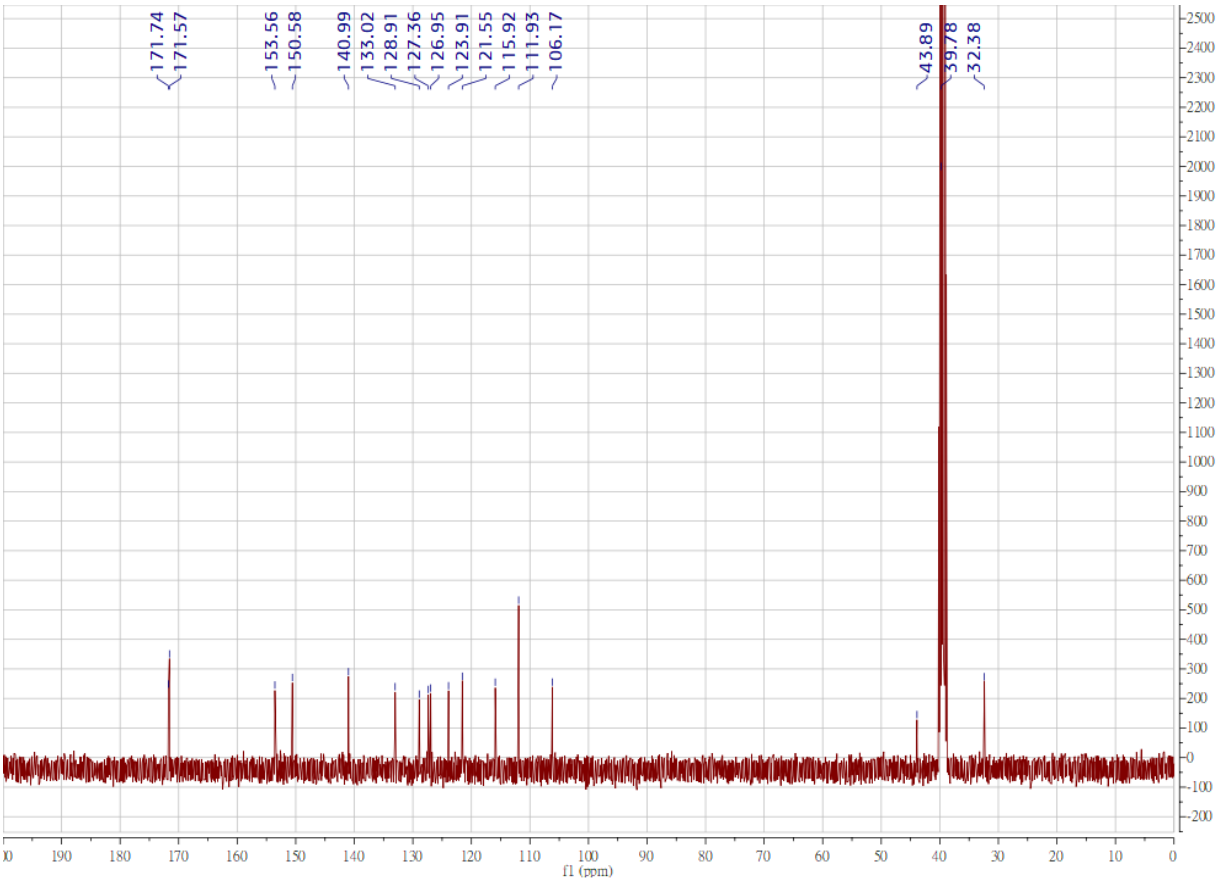
171.74
171.57
153.56
150.58
140.99
133.02
128.91
127.36
126.95
123.91
121.55
115.92
111.93
106.17
43.89
39.78
32.38
f1 (ppm)

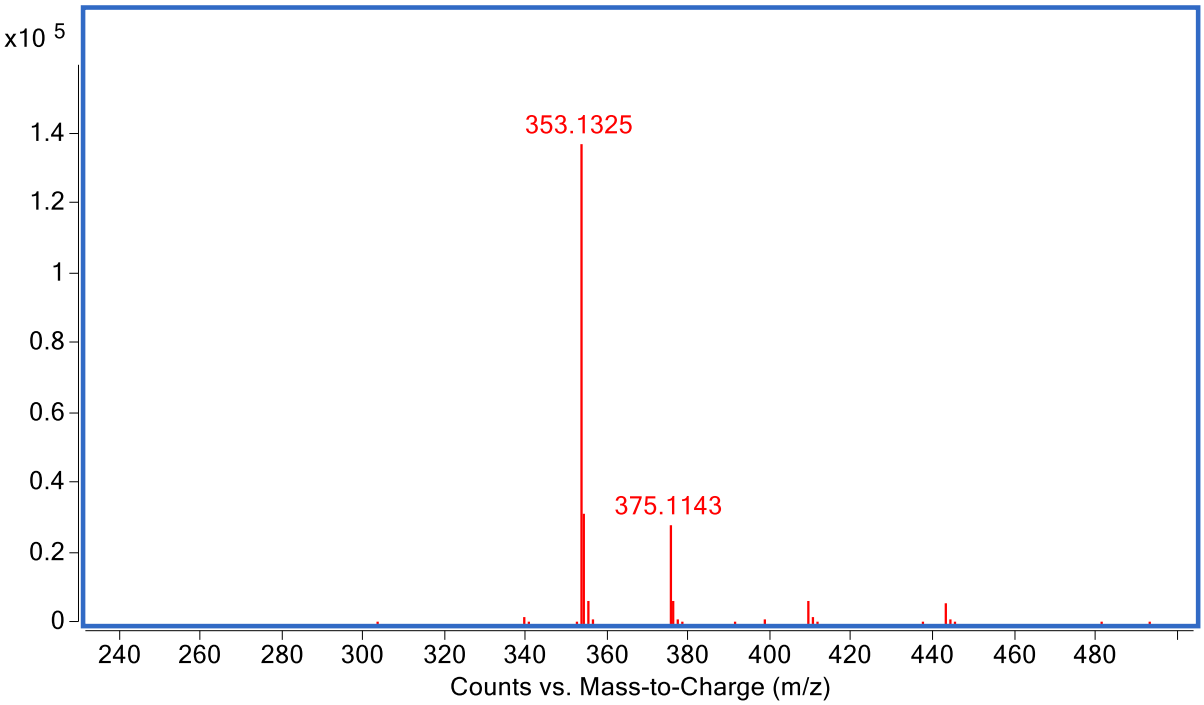

Figure S6. ^{1}H NMR, ^{13}C NMR and HRMS of **B3N**.

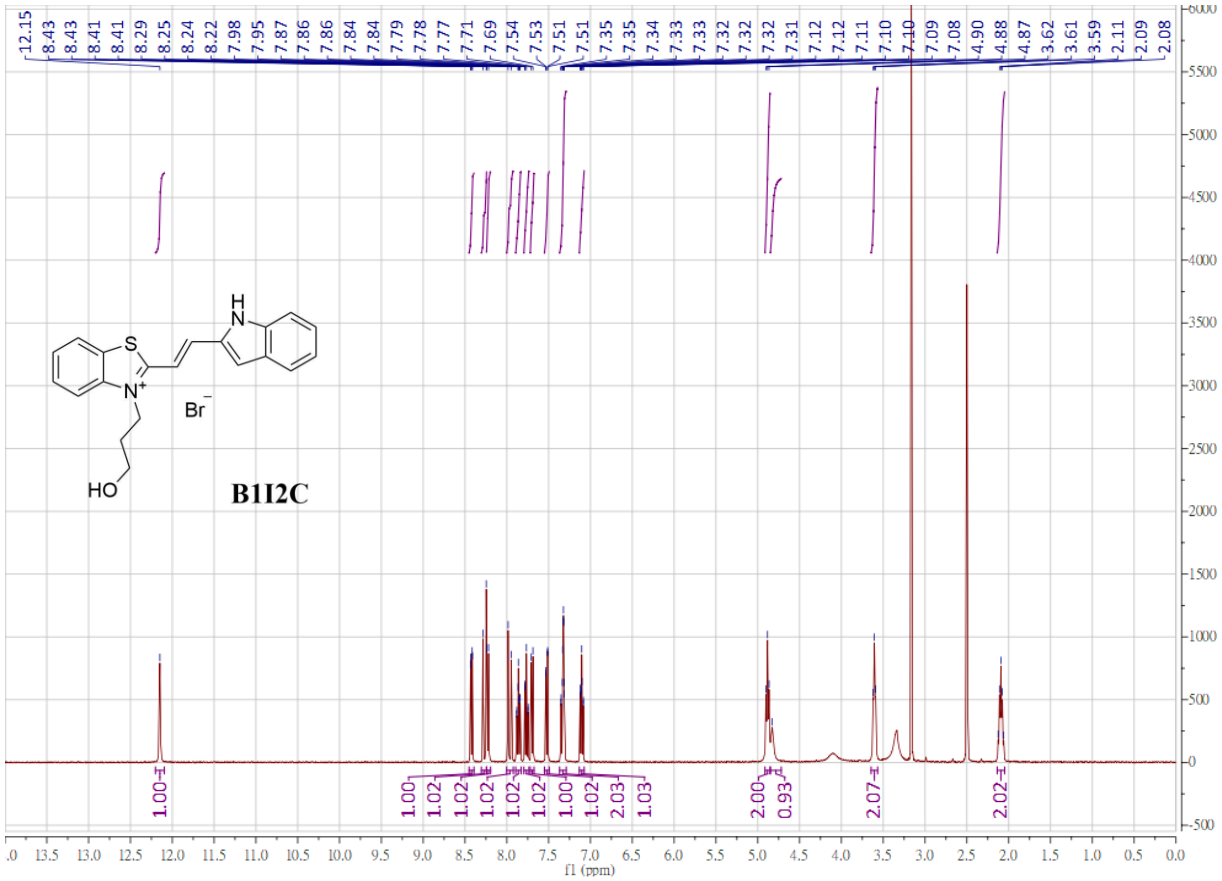
B1I2C
Br
HO
f1 (ppm)

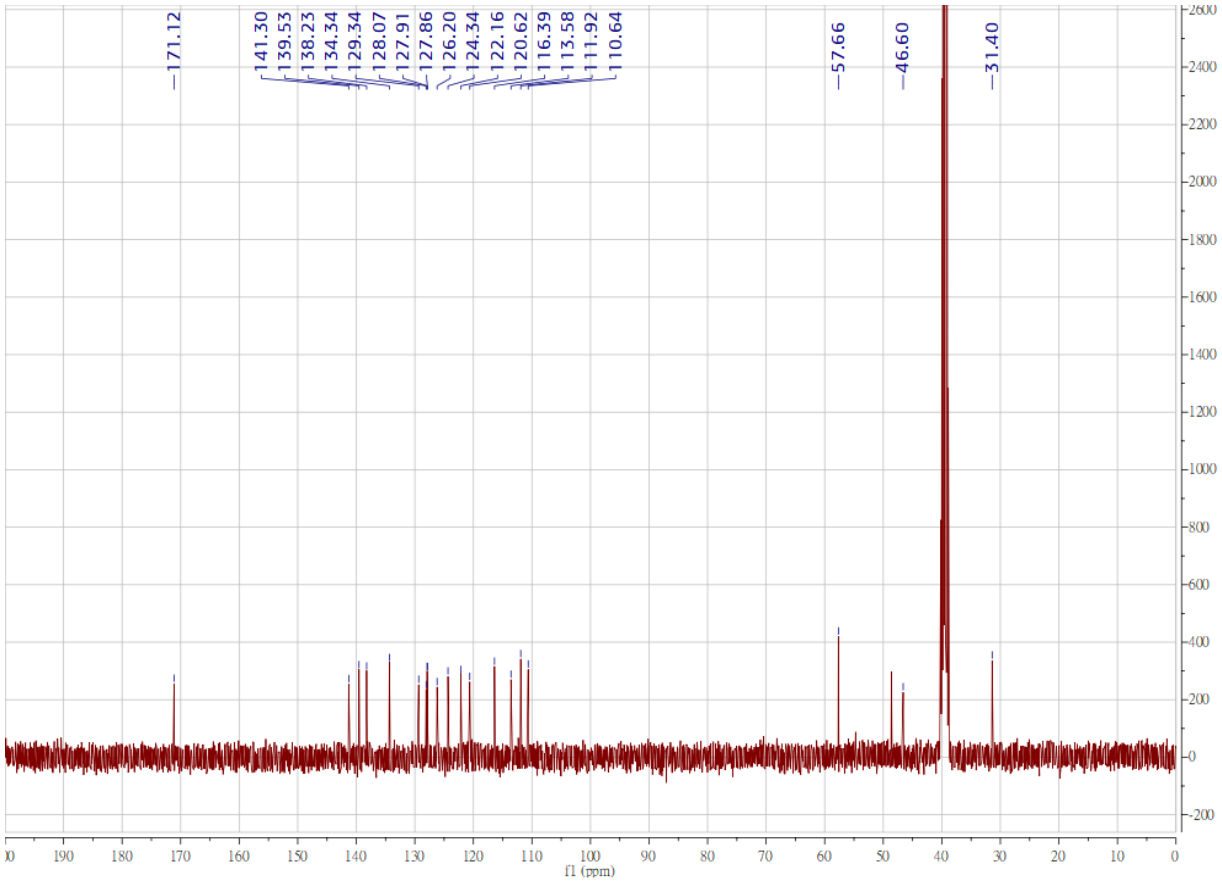
f1 (ppm)

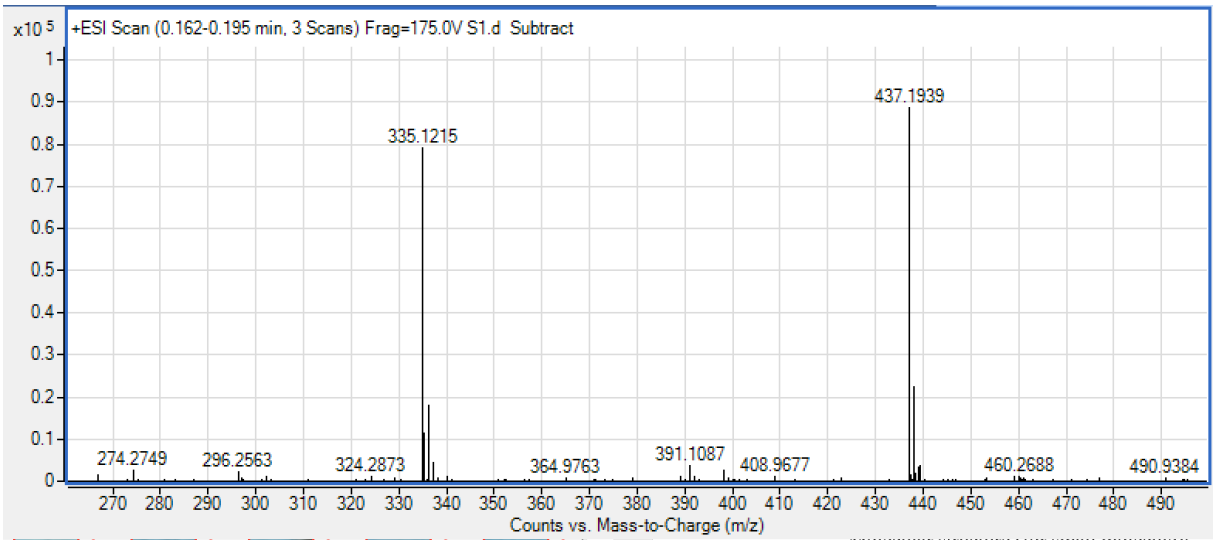

Figure S7. ^{1}H NMR, ^{13}C NMR and HRMS of **B1I2C**.

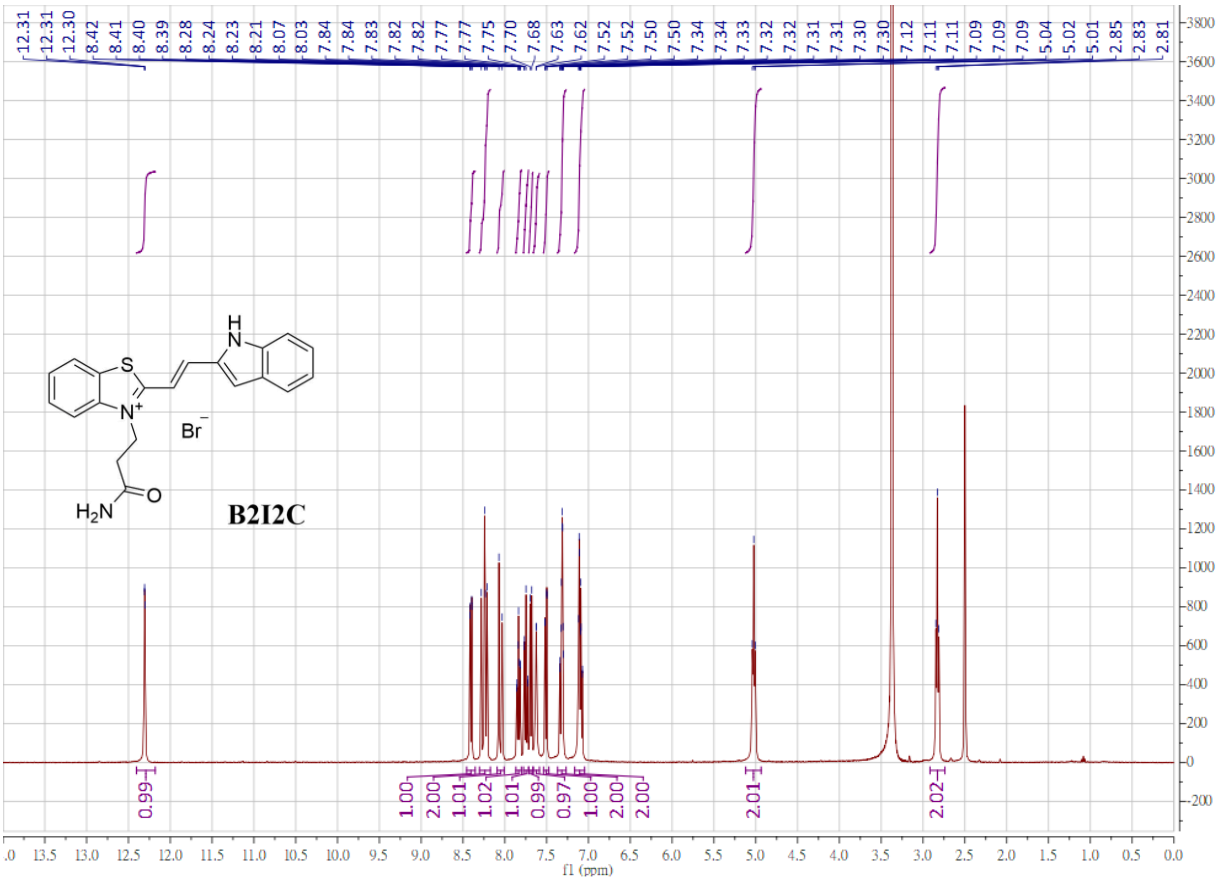
B2I2C

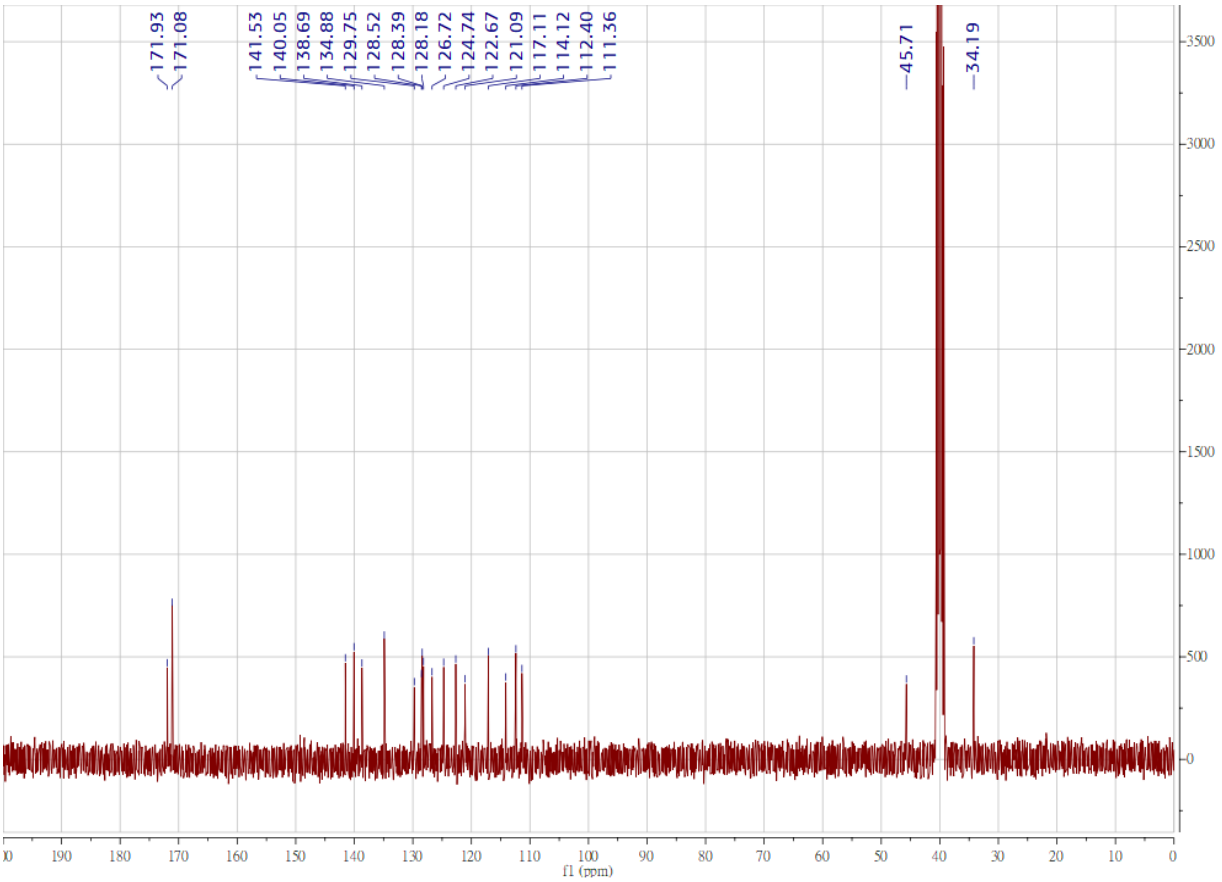

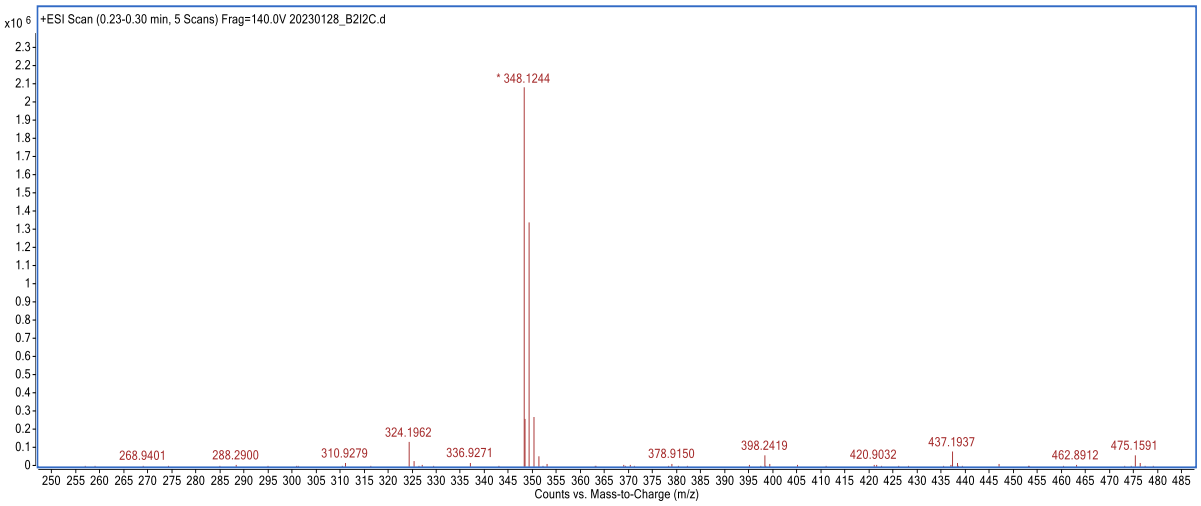

Figure S8. ^{1}H NMR, ^{13}C NMR and HRMS of **B2I2C**.

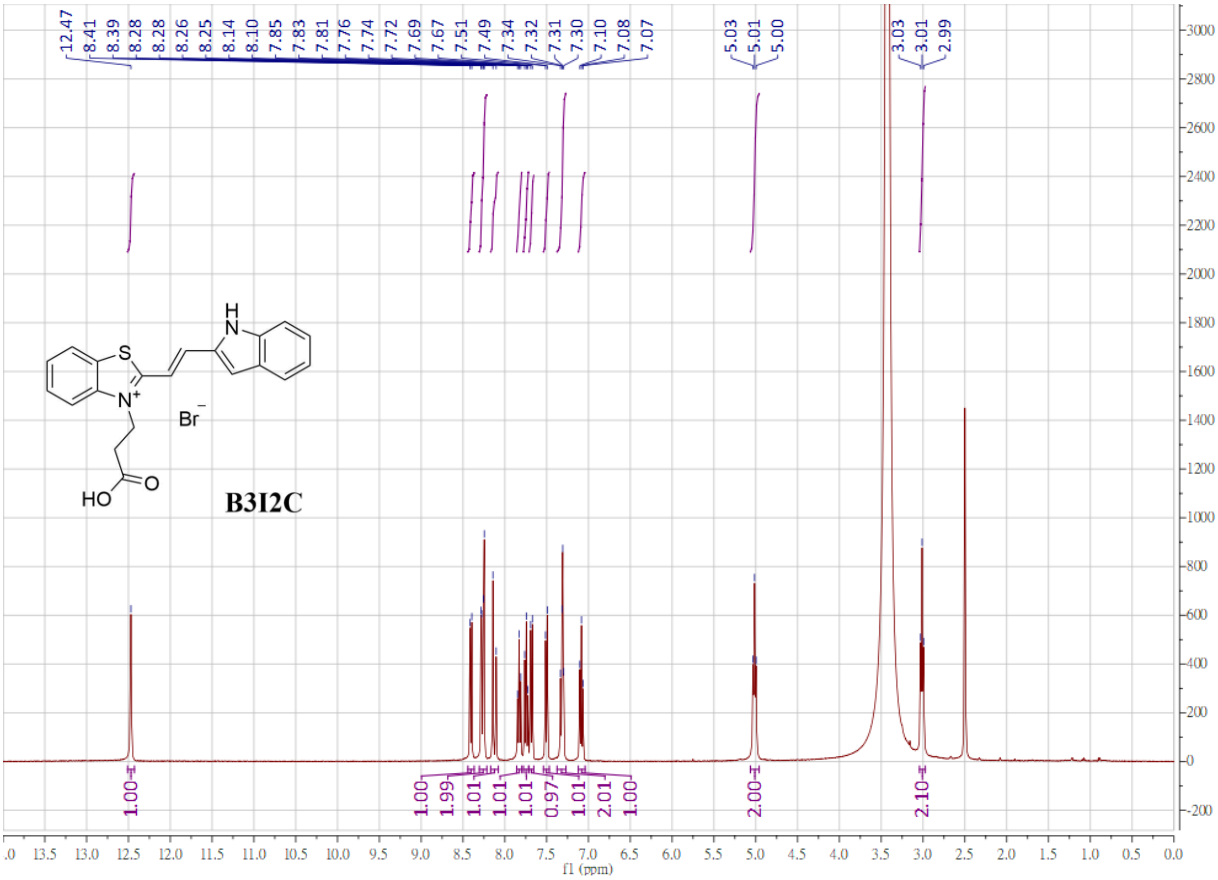
12.47
8.41
8.39
8.28
8.28
8.26
8.25
8.14
8.10
7.85
7.83
7.81
7.76
7.74
7.72
7.69
7.67
7.51
7.49
7.34
7.32
7.31
7.30
7.10
7.08
7.07
5.03
5.01
5.00
3.03
3.01
2.99
1.00
1.00
1.99
1.01
1.01
1.01
0.97
1.01
2.01
1.00
2.00
2.10
f1 (ppm)
B3I2C

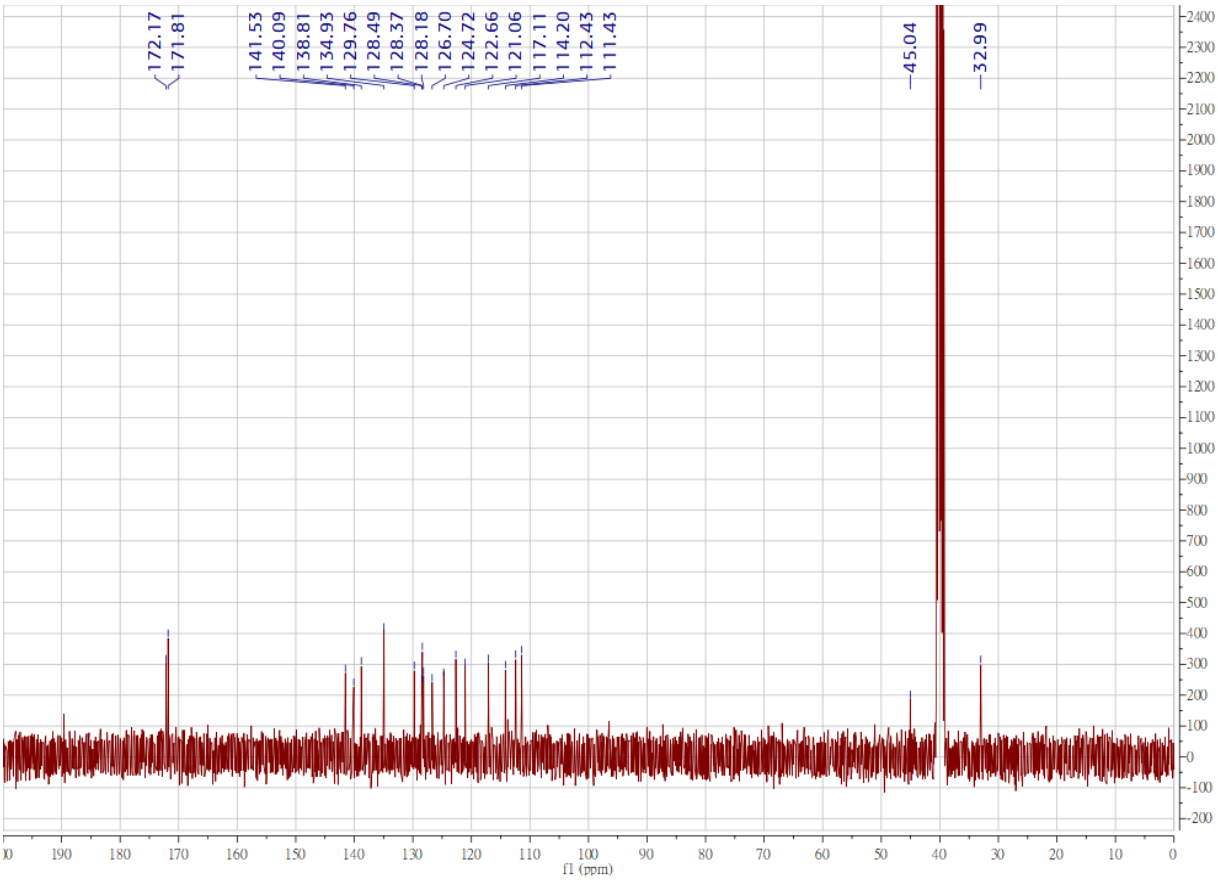
172.17
171.81
141.53
140.09
138.81
134.93
129.76
128.49
128.37
128.18
126.70
124.72
122.66
121.06
117.11
114.20
112.43
111.43
45.04
32.99
f1 (ppm)

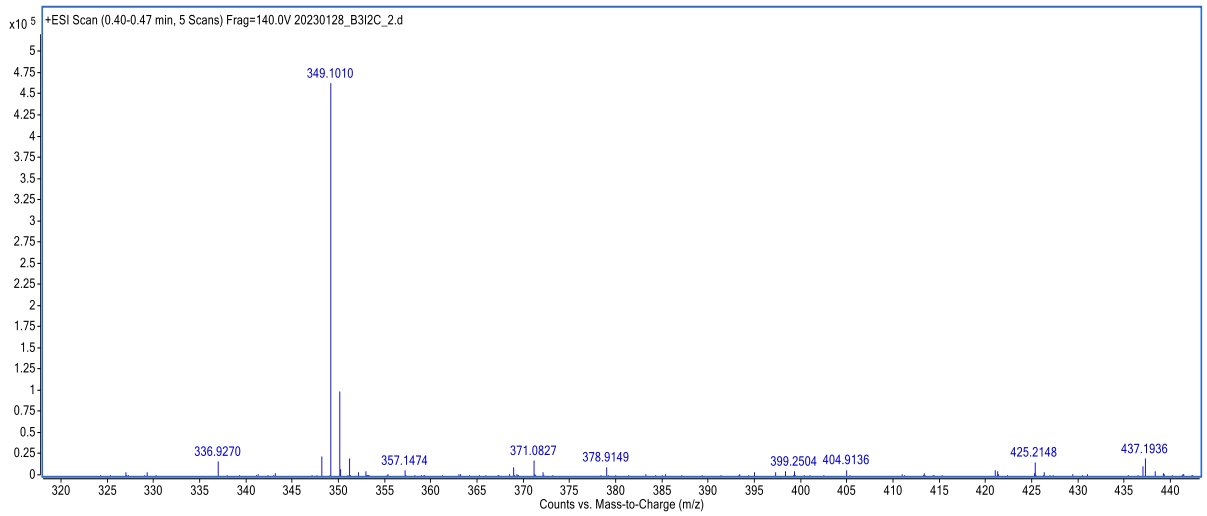

Figure S9. ^{1}H NMR, ^{13}C NMR and HRMS of **B3I2C**.

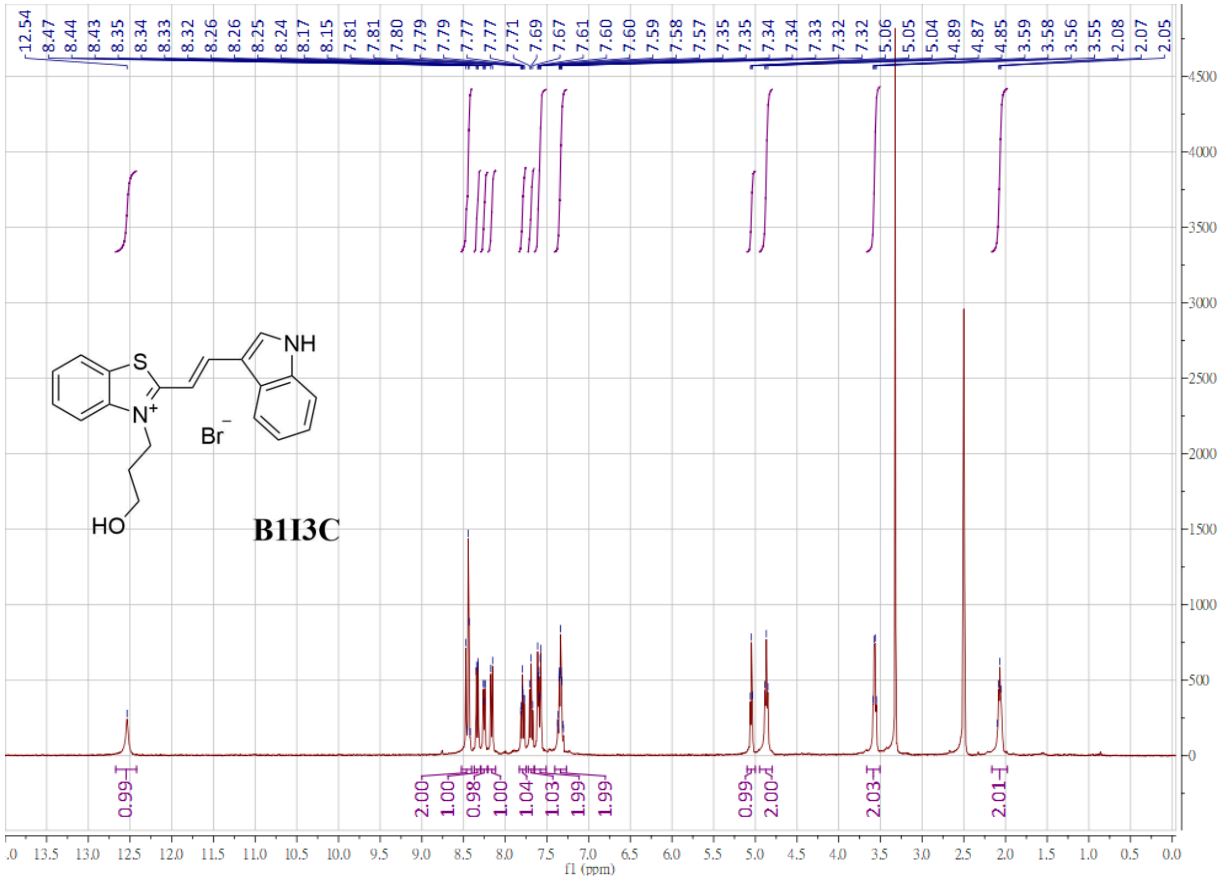
12.54
8.47
8.44
8.43
8.35
8.34
8.33
8.32
8.26
8.26
8.25
8.24
8.17
8.15
7.81
7.81
7.80
7.79
7.79
7.77
7.77
7.71
7.69
7.67
7.61
7.60
7.60
7.59
7.58
7.57
7.35
7.35
7.34
7.34
7.33
7.32
5.06
5.05
5.04
4.89
4.87
4.85
3.59
3.58
3.56
3.55
2.08
2.07
2.05
S
NH
N+
Br−
HO
B1I3C
0.99
2.00
1.00
0.98
1.00
1.04
1.03
1.99
1.99
0.99
2.00
2.03
2.01
f1 (ppm)

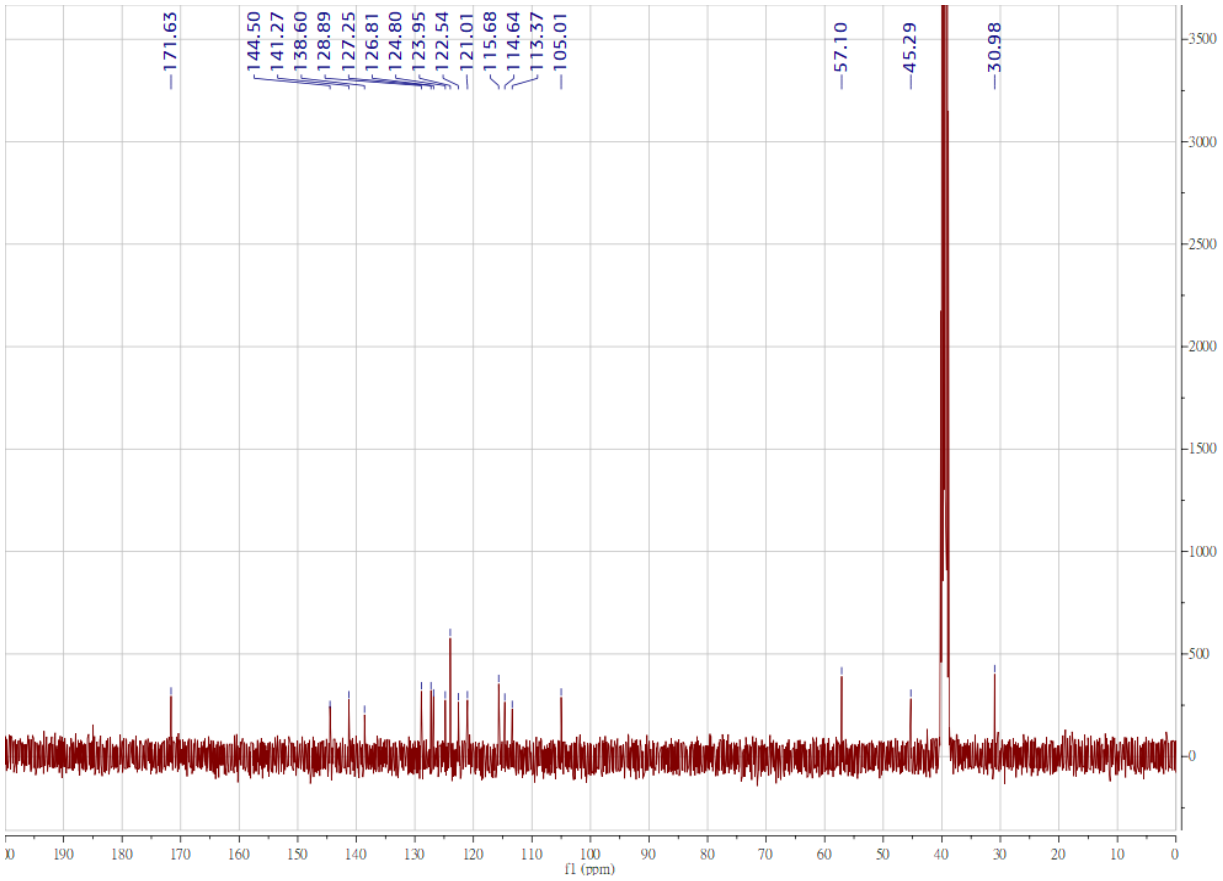
171.63
144.50
141.27
138.60
128.89
127.25
126.81
124.80
123.95
122.54
121.01
115.68
114.64
113.37
105.01
57.10
45.29
30.98
f1 (ppm)

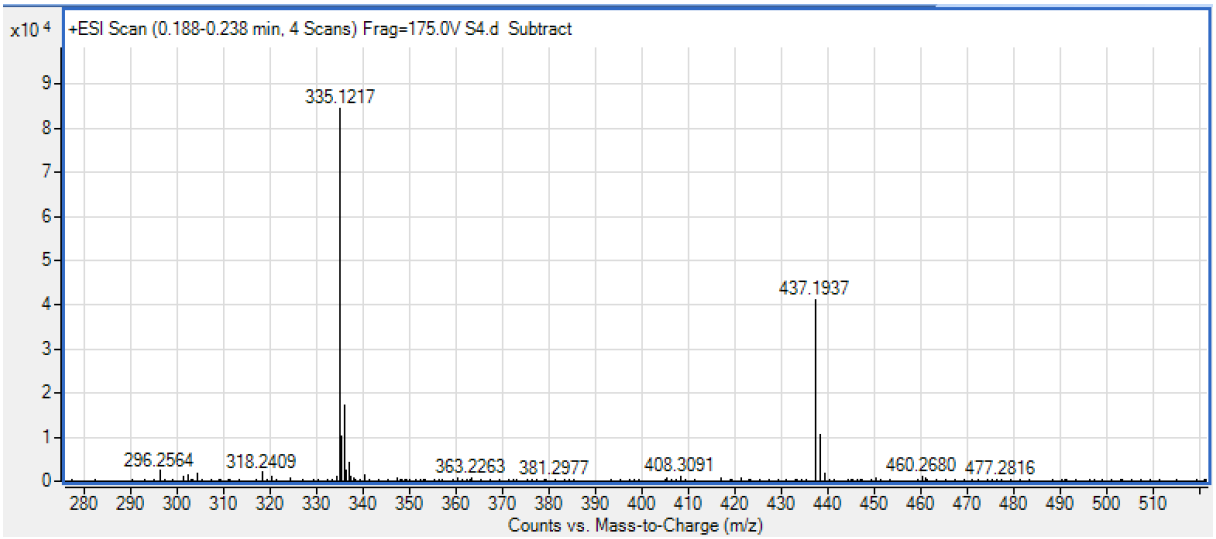

Figure S10. ^{1}H NMR, ^{13}C NMR and HRMS of **B1I3C**.

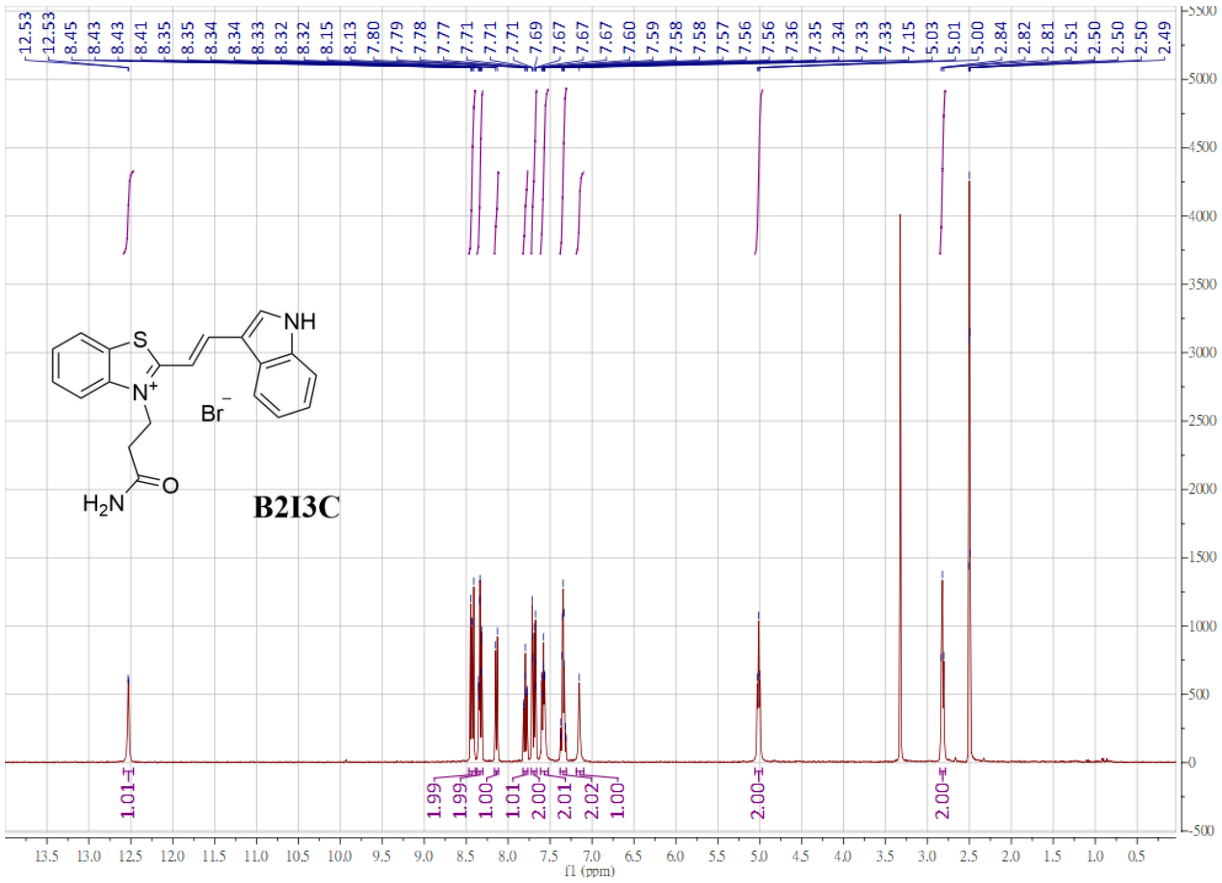
B2I3C

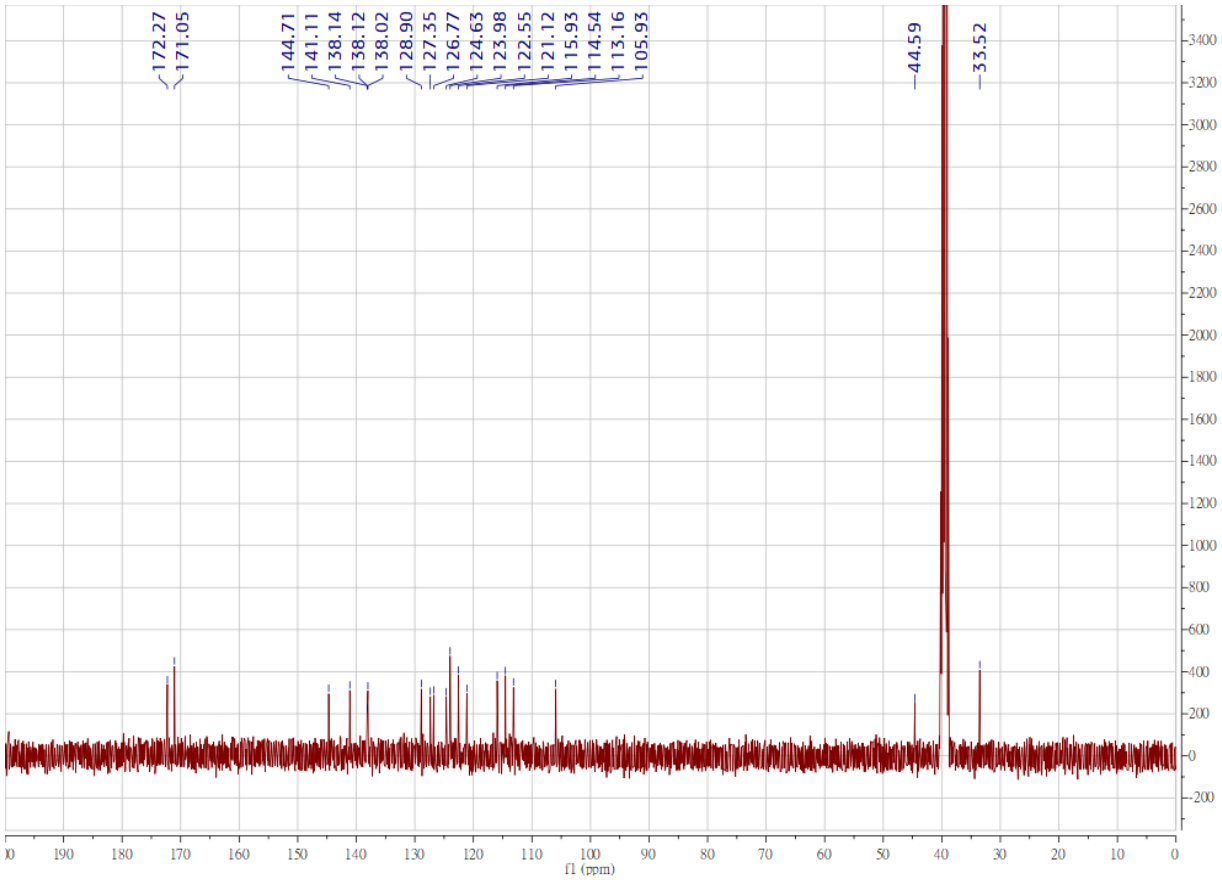

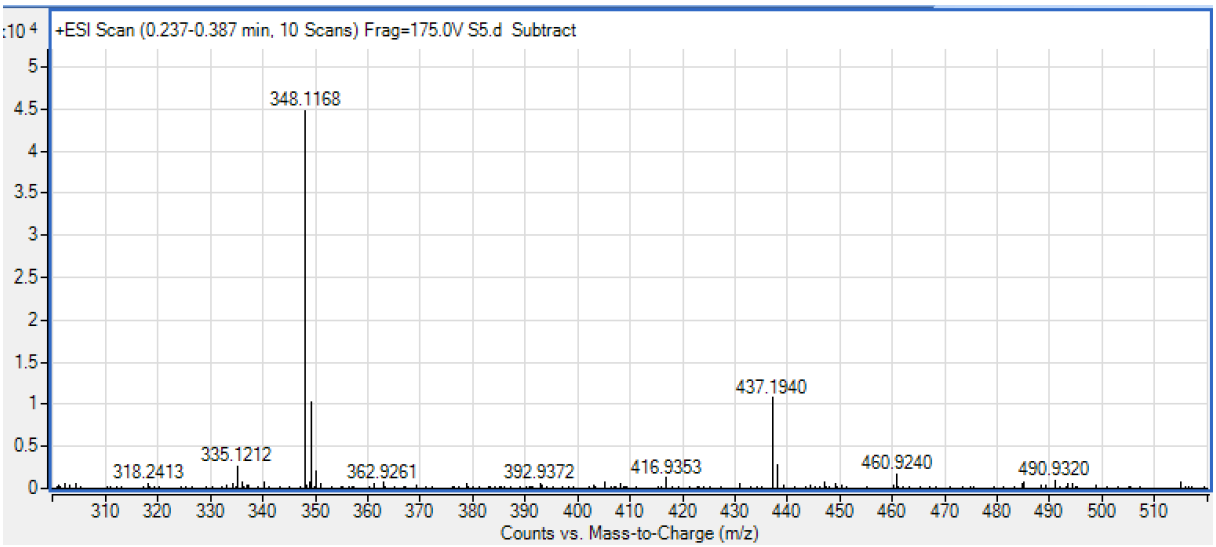

Figure S11. ^{1}H NMR, ^{13}C NMR and HRMS of **B2I3C**.

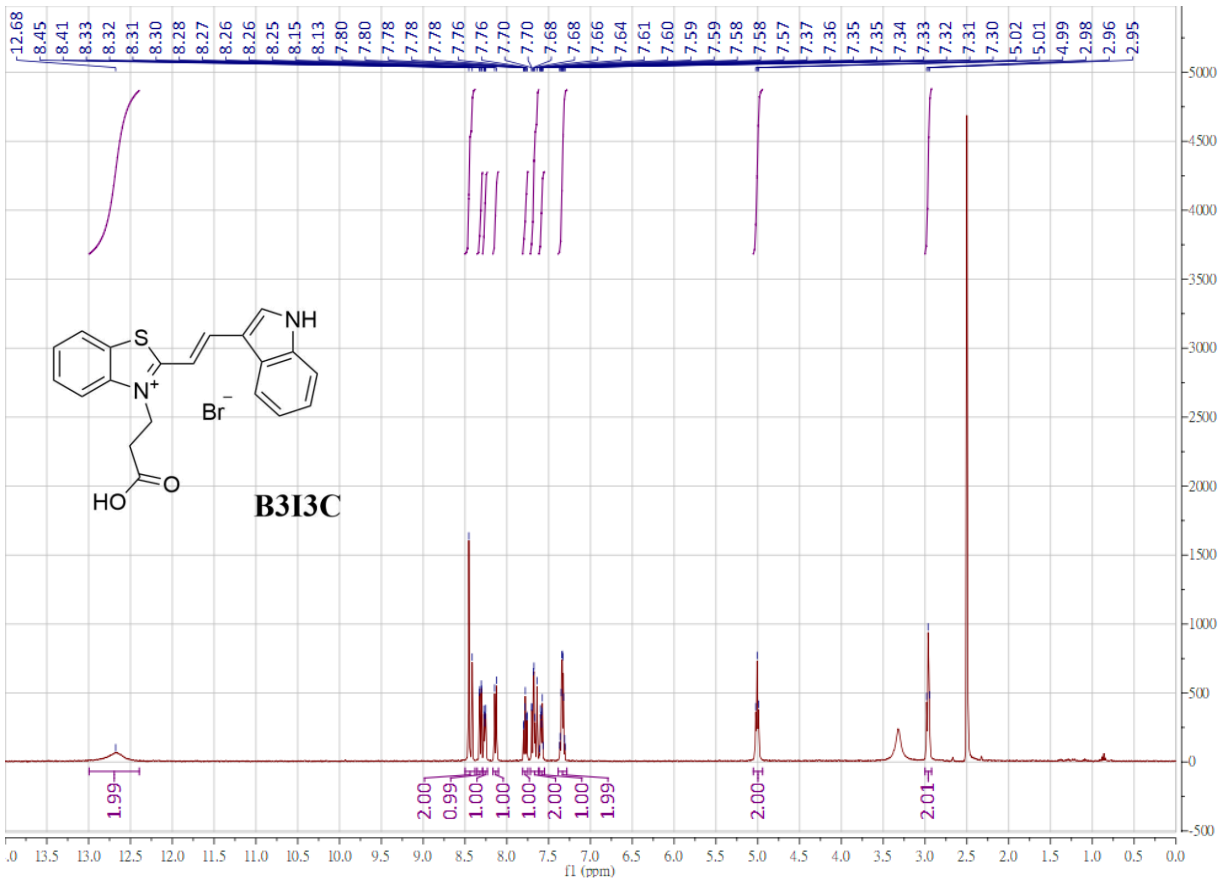
12.68
8.45
8.41
8.33
8.32
8.31
8.30
8.28
8.27
8.26
8.26
8.25
8.15
8.13
7.80
7.80
7.78
7.78
7.78
7.76
7.76
7.70
7.70
7.68
7.68
7.66
7.64
7.61
7.60
7.59
7.59
7.58
7.58
7.57
7.37
7.36
7.35
7.35
7.34
7.33
7.32
7.31
7.30
5.02
5.01
4.99
2.98
2.96
2.95
S
NH
N+
Br-
HO
O
B3I3C
1.99
2.00
0.99
1.00
1.00
1.00
2.00
1.00
1.99
2.00
2.01
f1 (ppm)

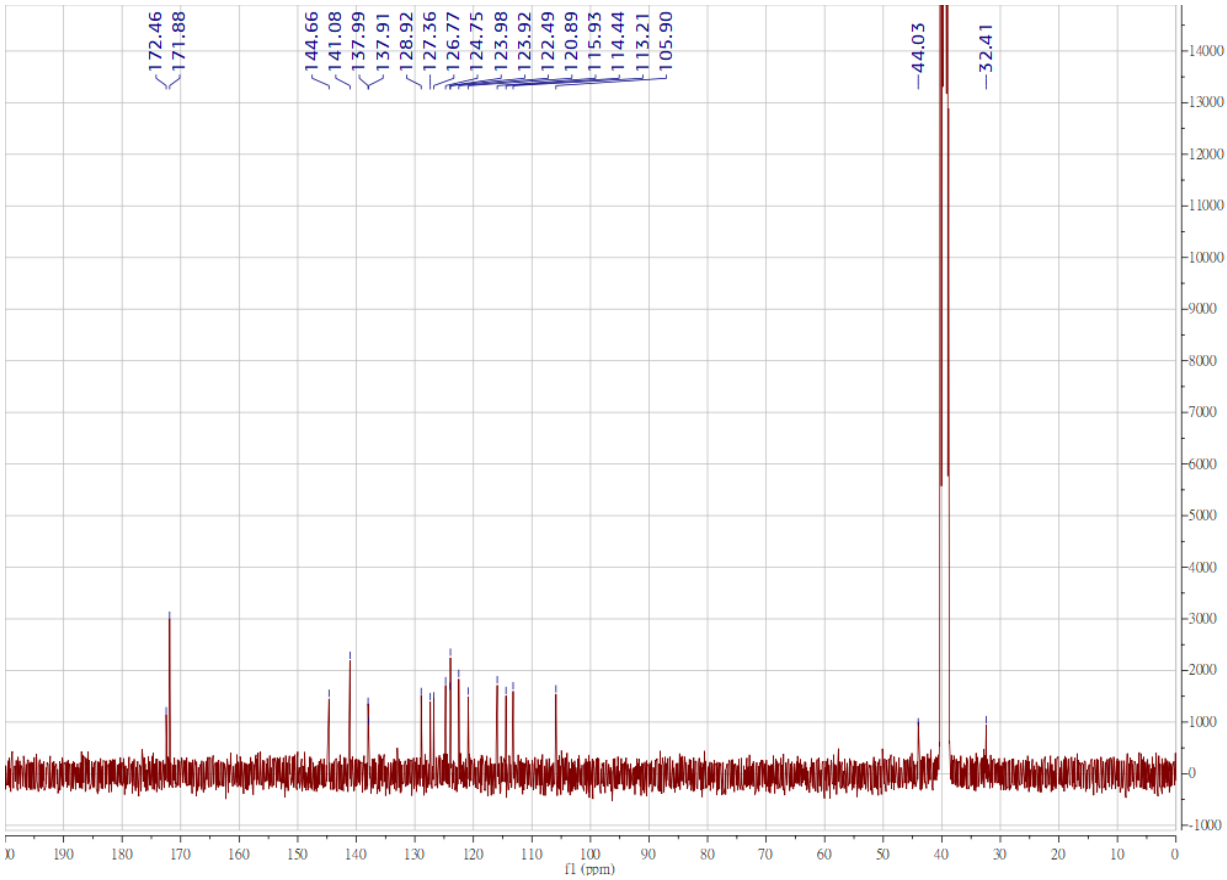
172.46
171.88
144.66
141.08
137.99
137.91
128.92
127.36
126.77
124.75
123.98
123.92
122.49
120.89
115.93
114.44
113.21
105.90
44.03
32.41
f1 (ppm)

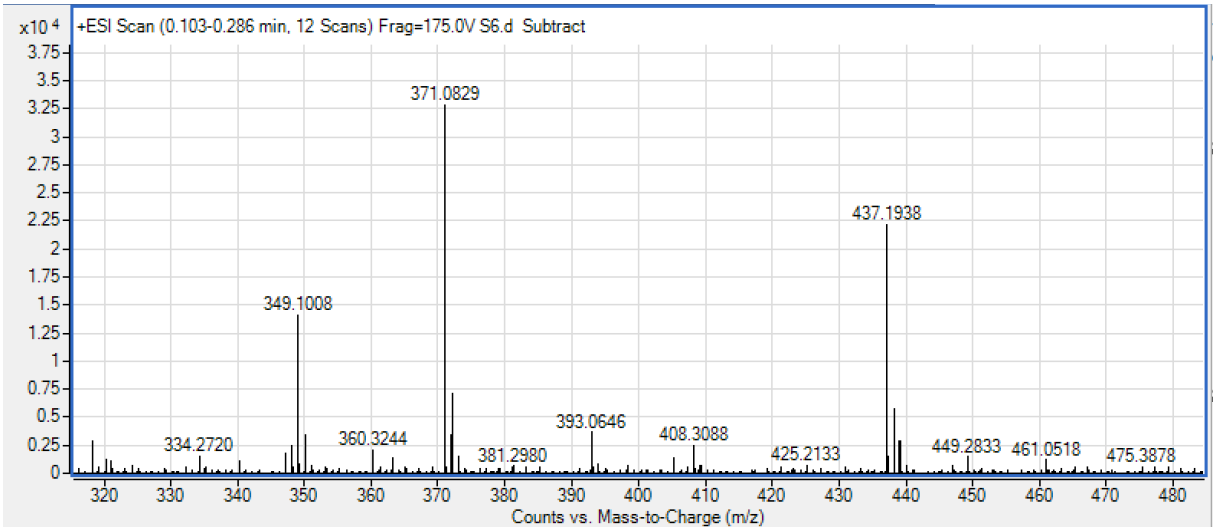

Figure S12. ^{1}H NMR, ^{13}C NMR and HRMS of **B3I3C**.

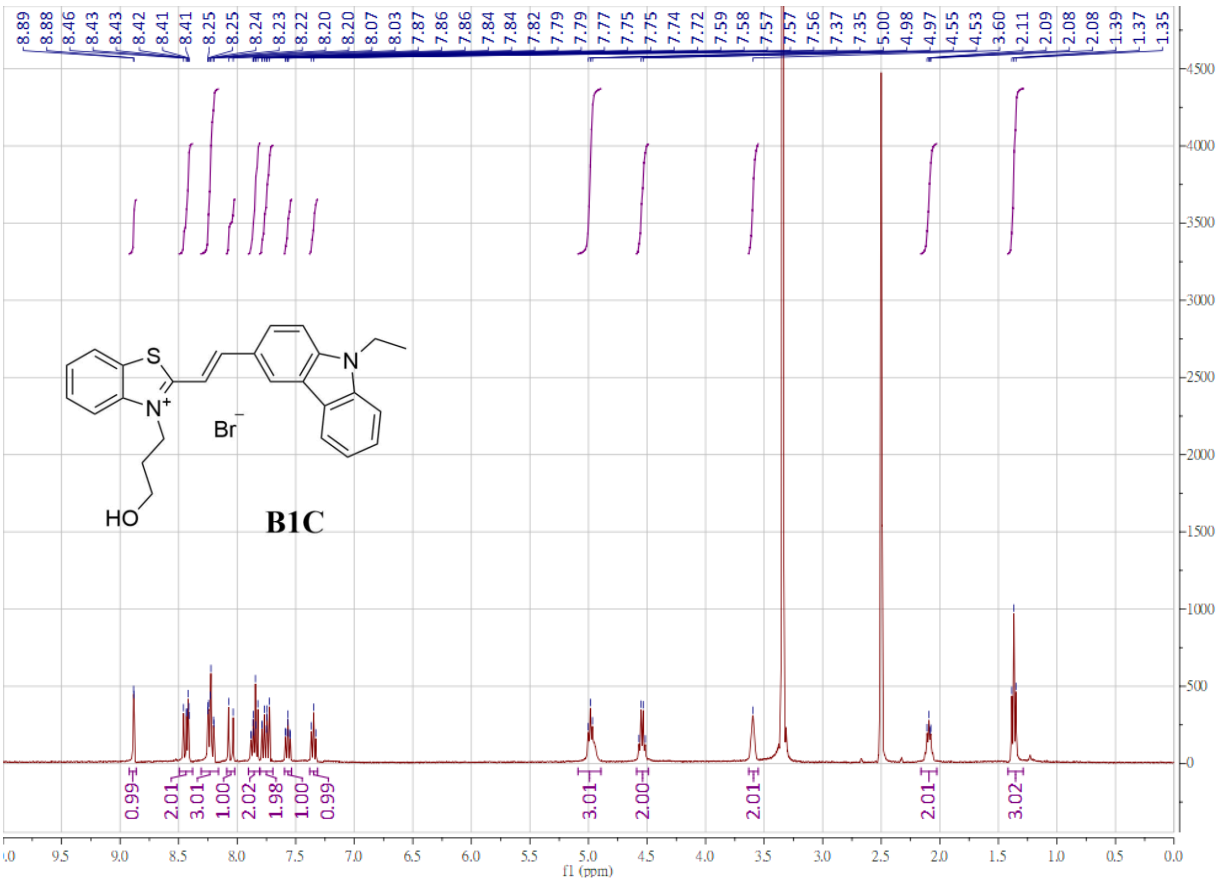
B1C
f1 (ppm)


f1 (ppm)

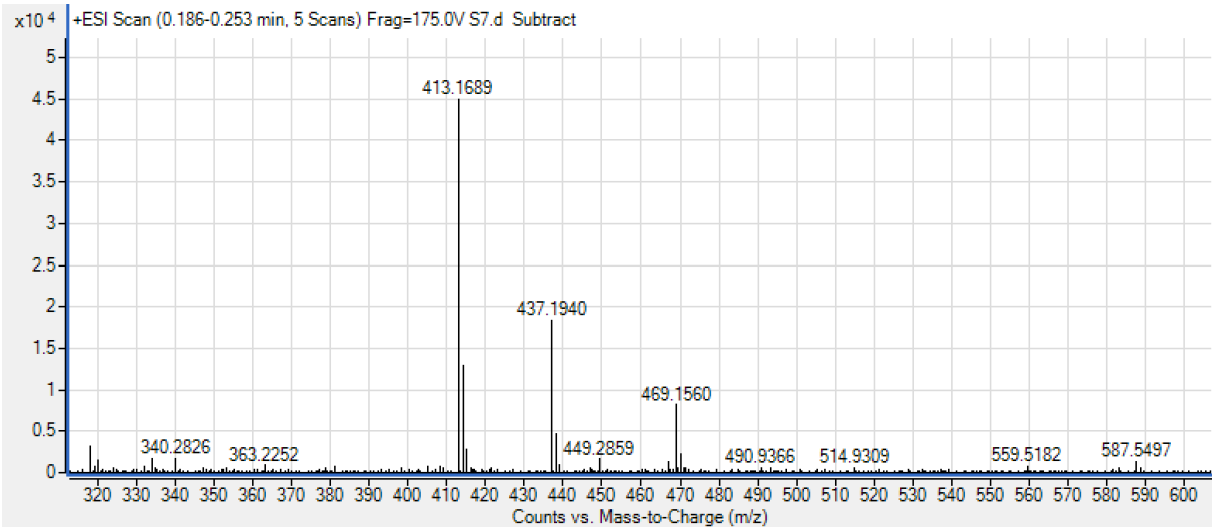

Figure S13. ^{1}H NMR, ^{13}C NMR and HRMS of **B1C.**

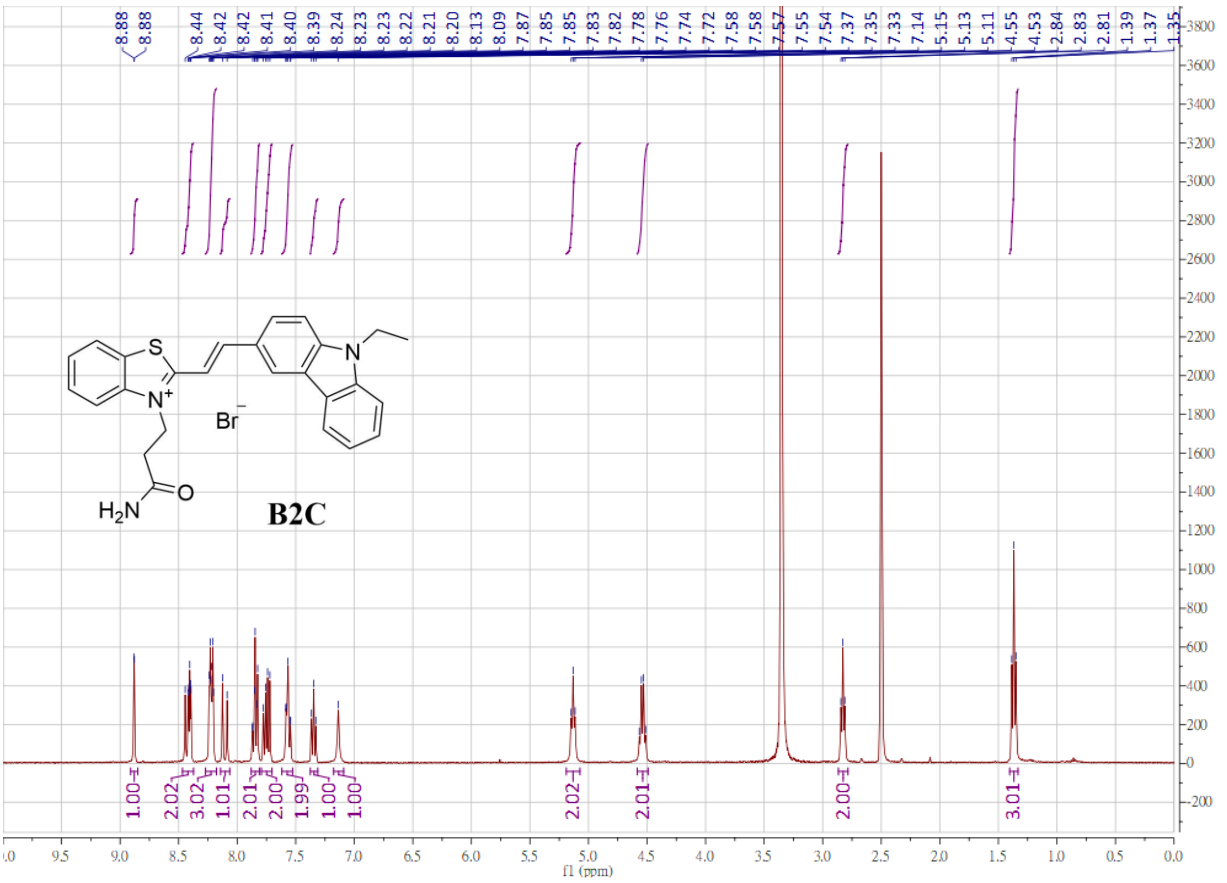
8.88
8.88
8.44
8.42
8.42
8.41
8.40
8.39
8.24
8.23
8.23
8.22
8.21
8.20
8.13
8.09
7.87
7.85
7.85
7.83
7.82
7.78
7.76
7.74
7.72
7.58
7.58
7.57
7.55
7.54
7.37
7.35
7.33
7.14
5.15
5.13
5.11
4.55
4.53
2.84
2.83
2.81
1.39
1.37
1.35
S
N+
Br−
N
O
H2N
B2C
1.00
2.02
3.02
1.01
2.01
2.00
1.99
1.00
1.00
2.02
2.01
2.00
3.01
f1 (ppm)

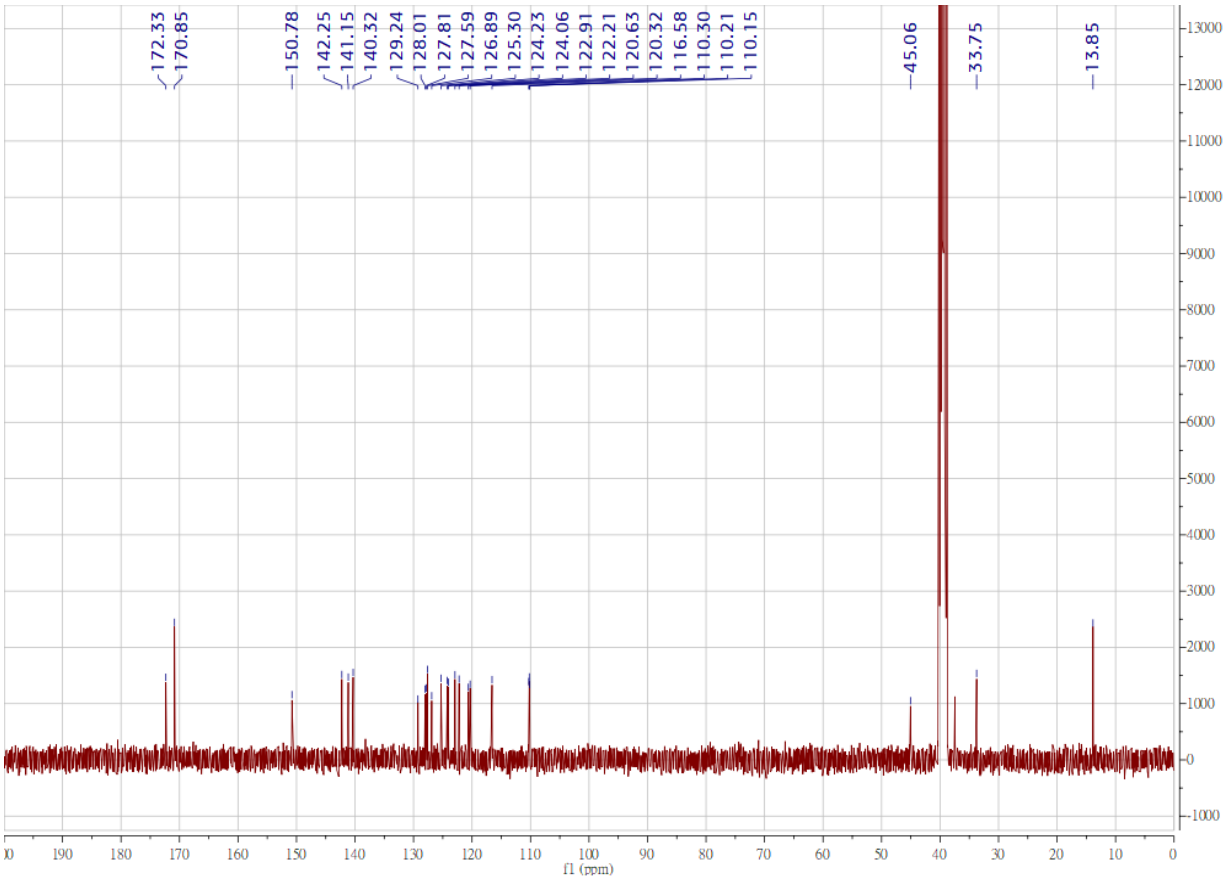
172.33
170.85
150.78
142.25
141.15
140.32
129.24
128.01
127.81
127.59
126.89
125.30
124.23
124.06
122.91
122.21
120.63
120.32
116.58
110.30
110.21
110.15
45.06
33.75
13.85
f1 (ppm)

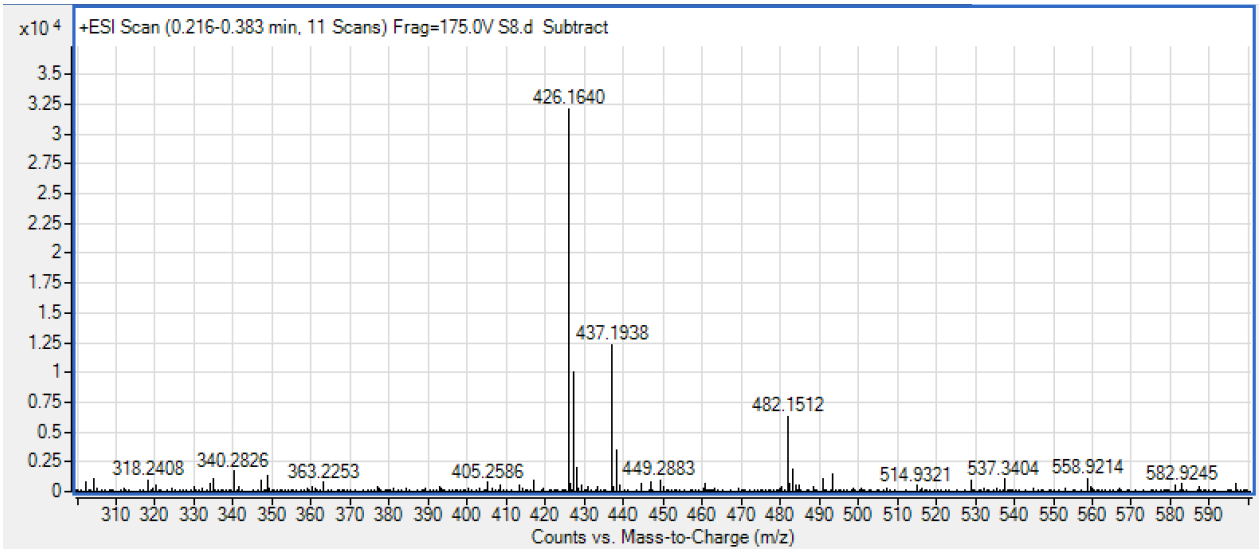

Figure S14. ^{1}H NMR, ^{13}C NMR and HRMS of **B2C**.

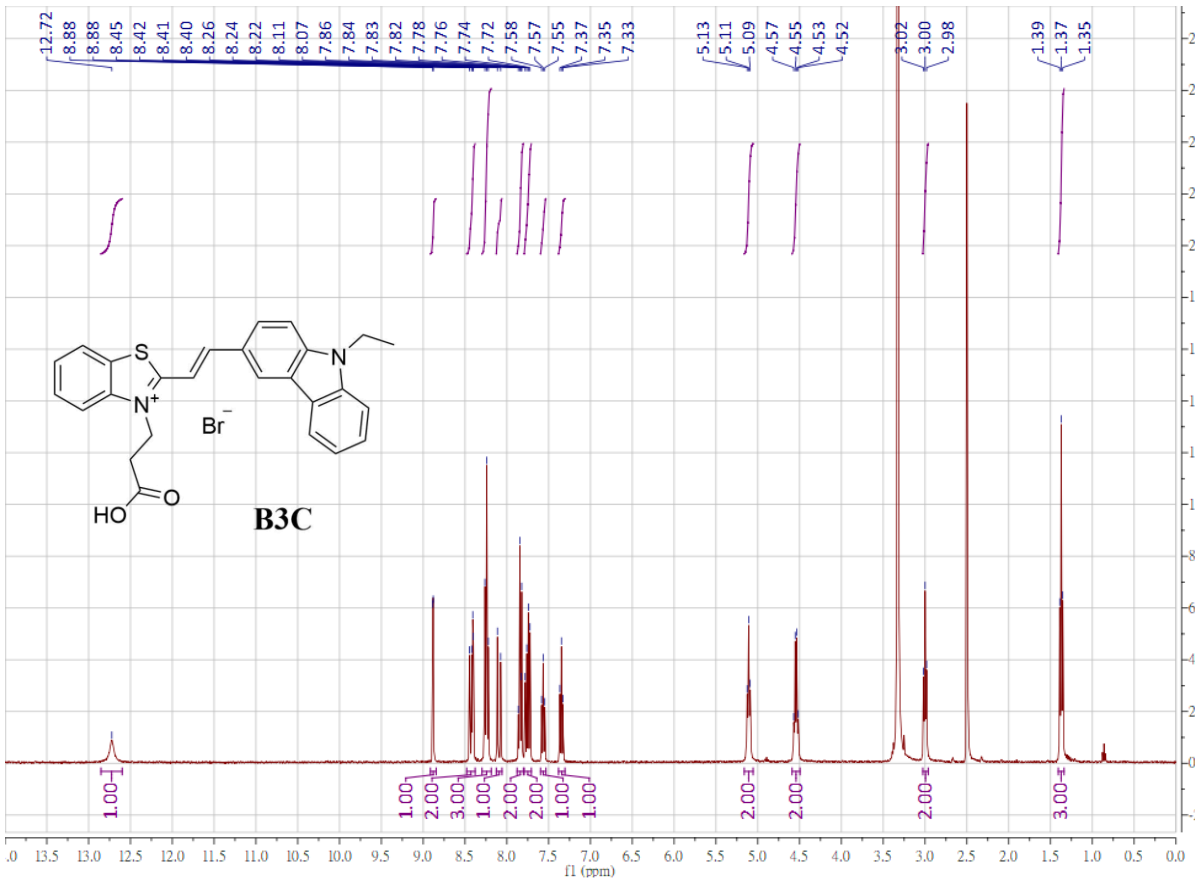
12.72
8.88
8.88
8.45
8.42
8.41
8.40
8.26
8.24
8.22
8.11
8.07
7.86
7.84
7.83
7.82
7.78
7.76
7.74
7.72
7.58
7.57
7.55
7.37
7.35
7.33
5.13
5.11
5.09
4.57
4.55
4.53
4.52
3.02
3.00
2.98
1.39
1.37
1.35
S
N
N+
Br−
HO
O
B3C
1.00
1.00
2.00
3.00
1.00
2.00
2.00
1.00
1.00
2.00
2.00
2.00
3.00
f1 (ppm)


172.65
171.55
151.00
142.25
141.09
140.30
129.26
127.98
127.91
127.57
126.87
125.27
124.20
122.89
122.21
120.65
120.31
116.55
110.20
110.15
110.14
44.47
37.45
32.54
13.85
f1 (ppm)

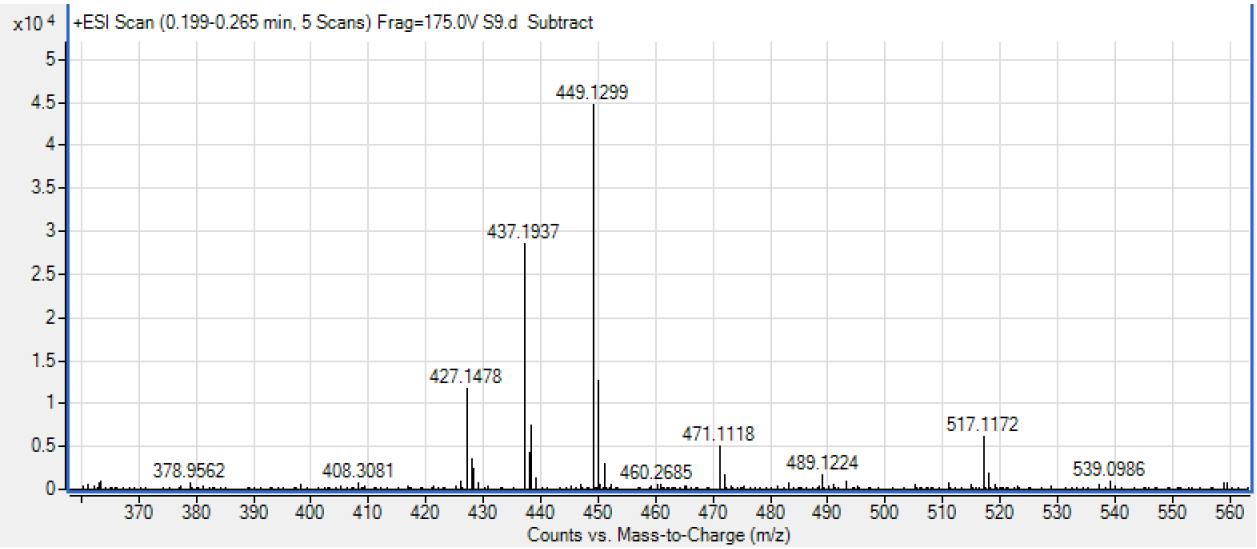

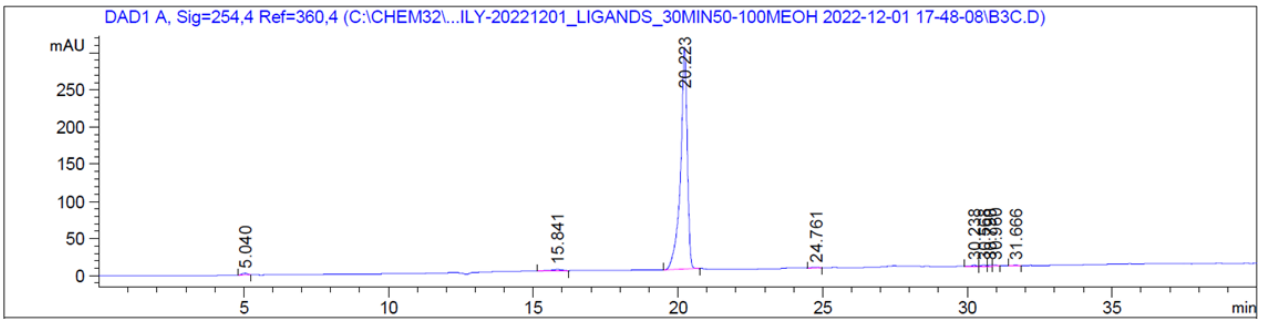

==========

Area Percent Report

==========

Sorted By : Signal
Multiplier : 1.0000
Dilution : 1.0000
Do not use Multiplier & Dilution Factor with ISTDs
Signal 1: DAD1 A, Sig=254,4 Ref=360,4

Peak #	RetTime [min]	Type	Width [min]	Area [mAU*s]	Height [mAU]	Area %
1	5.040	BB	0.2175	31.71553	2.31990	0.6322
2	15.841	BB	0.3517	48.03683	1.87017	0.9575
3	20.223	BB	0.2341	4862.02979	298.40802	96.9155
4	24.761	BB	0.2055	15.58688	1.09890	0.3107
5	30.238	BB	0.1381	11.40798	1.25453	0.2274
6	30.568	BV	0.1450	14.68199	1.54256	0.2927
7	30.790	VV	0.1287	10.78080	1.24844	0.2149
8	30.960	VB	0.1274	12.30385	1.47313	0.2453
9	31.666	BB	0.1509	10.23013	1.03888	0.2039
Totals :				5016.77378	310.25452	

Figure S15. ^{1}H NMR, ^{13}C NMR, HRMS and HPLC of **B3C**.

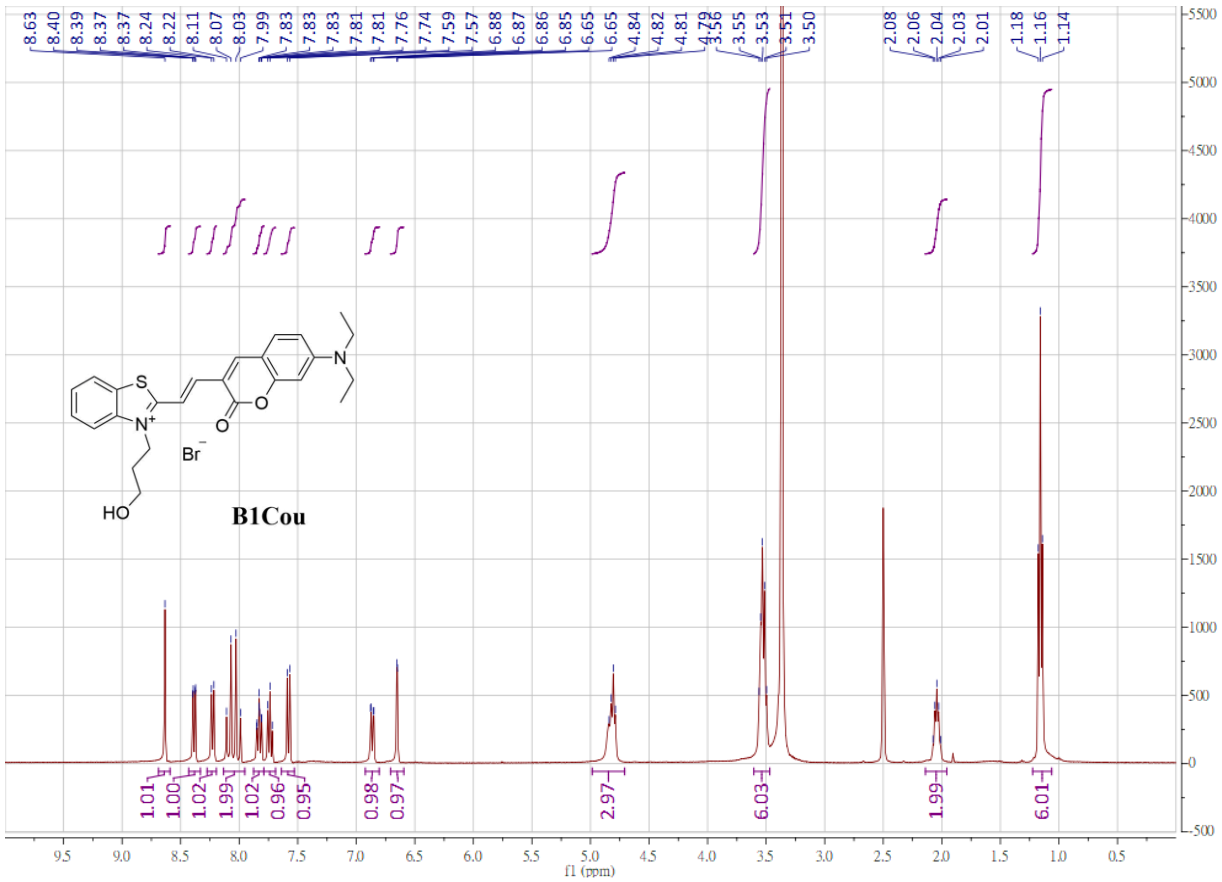
8.63
8.40
8.39
8.37
8.37
8.24
8.22
8.11
8.07
8.03
7.99
7.83
7.83
7.83
7.81
7.81
7.76
7.74
7.59
7.57
6.88
6.87
6.86
6.85
6.65
6.65
4.84
4.82
4.81
4.79
3.56
3.55
3.53
3.51
3.50
2.08
2.06
2.04
2.03
2.01
1.18
1.16
1.14
S
N+
Br−
O
O
N
HO
B1Cou
1.01
1.00
1.02
1.99
1.02
0.96
0.95
0.98
0.97
2.97
6.03
1.99
6.01
f1 (ppm)

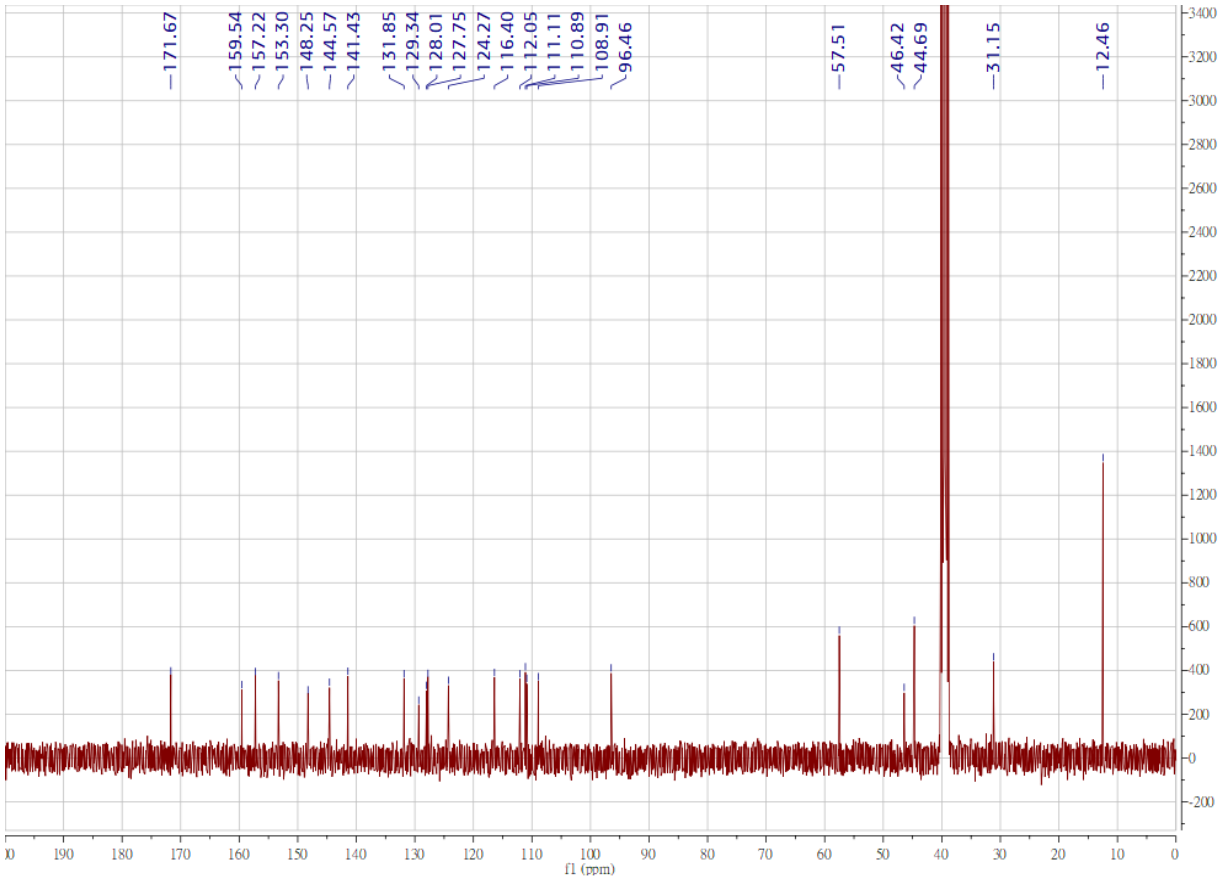
171.67
159.54
157.22
153.30
148.25
144.57
141.43
131.85
129.34
128.01
127.75
124.27
116.40
112.05
111.11
110.89
108.91
96.46
57.51
46.42
44.69
31.15
12.46
f1 (ppm)

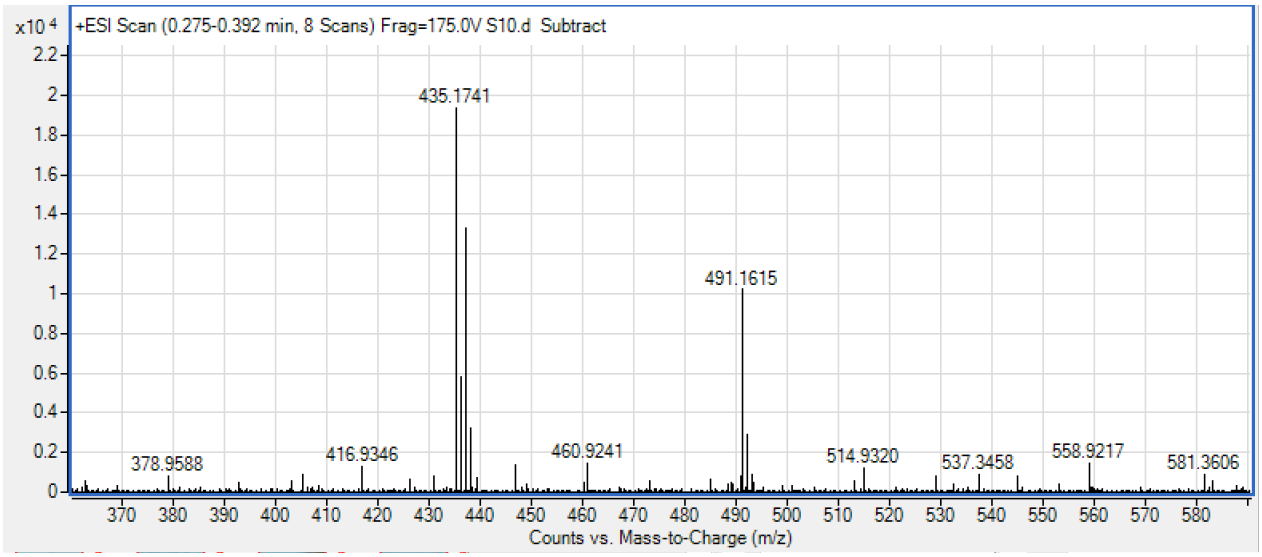

Figure S16. ^{1}H NMR, ^{13}C NMR and HRMS of **B1Cou**.

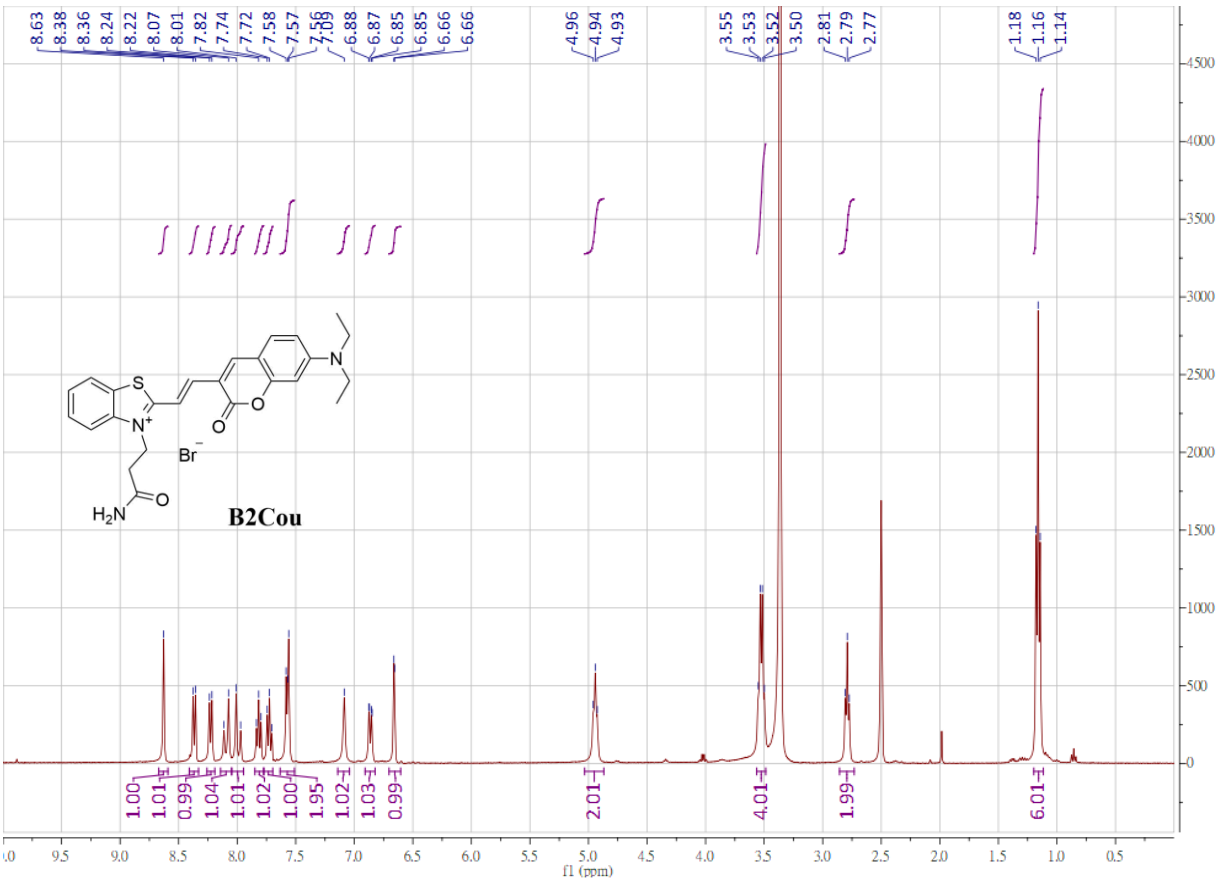
8.63
8.38
8.36
8.24
8.22
8.07
8.01
7.82
7.74
7.72
7.58
7.57
7.56
7.09
6.88
6.87
6.85
6.85
6.66
6.66
4.96
4.94
4.93
3.55
3.53
3.52
3.50
2.81
2.79
2.77
1.18
1.16
1.14
1.00
1.01
0.99
1.04
1.01
1.02
1.00
1.95
1.02
1.03
0.99
2.01
4.01
1.99
6.01
f1 (ppm)
B2Cou

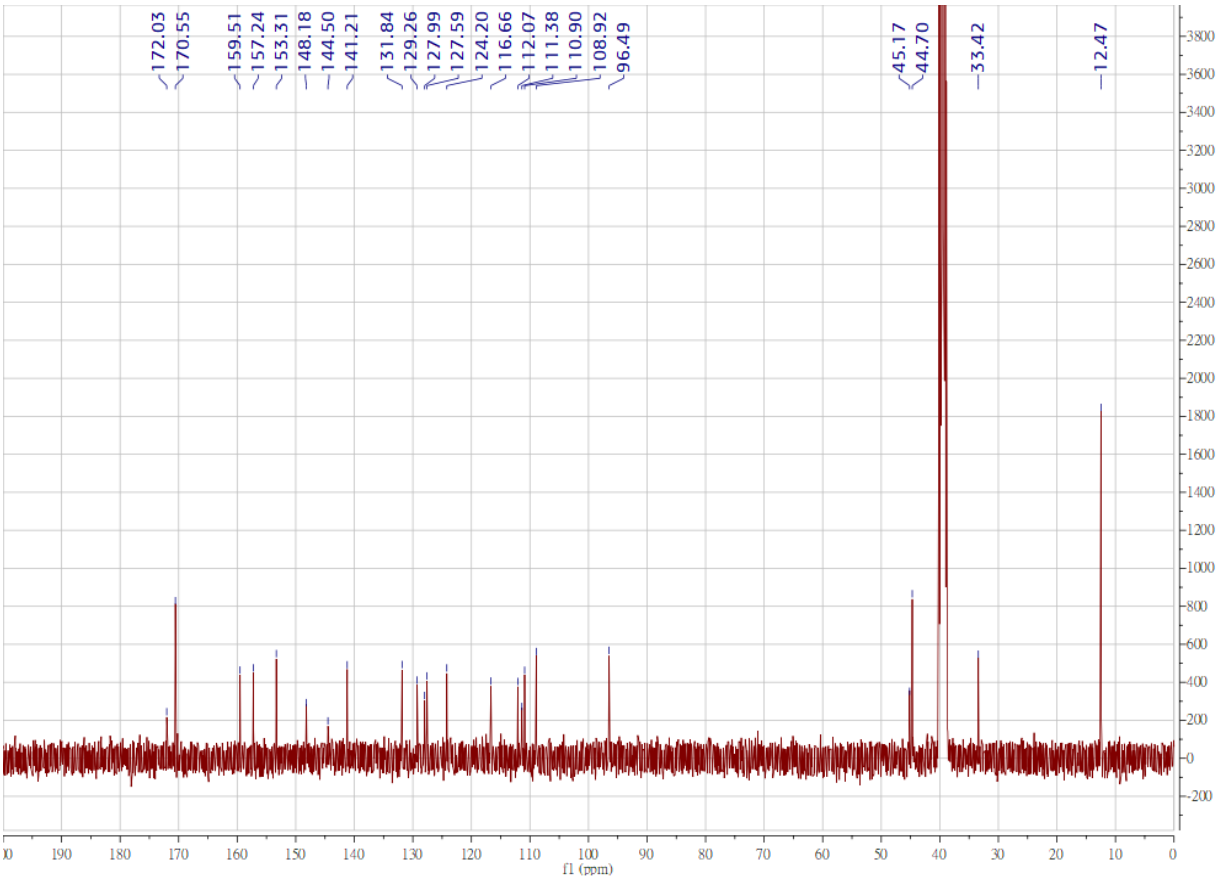
172.03
170.55
159.51
157.24
153.31
148.18
144.50
141.21
131.84
129.26
127.99
127.59
124.20
116.66
112.07
111.38
110.90
108.92
96.49
45.17
44.70
33.42
12.47
f1 (ppm)

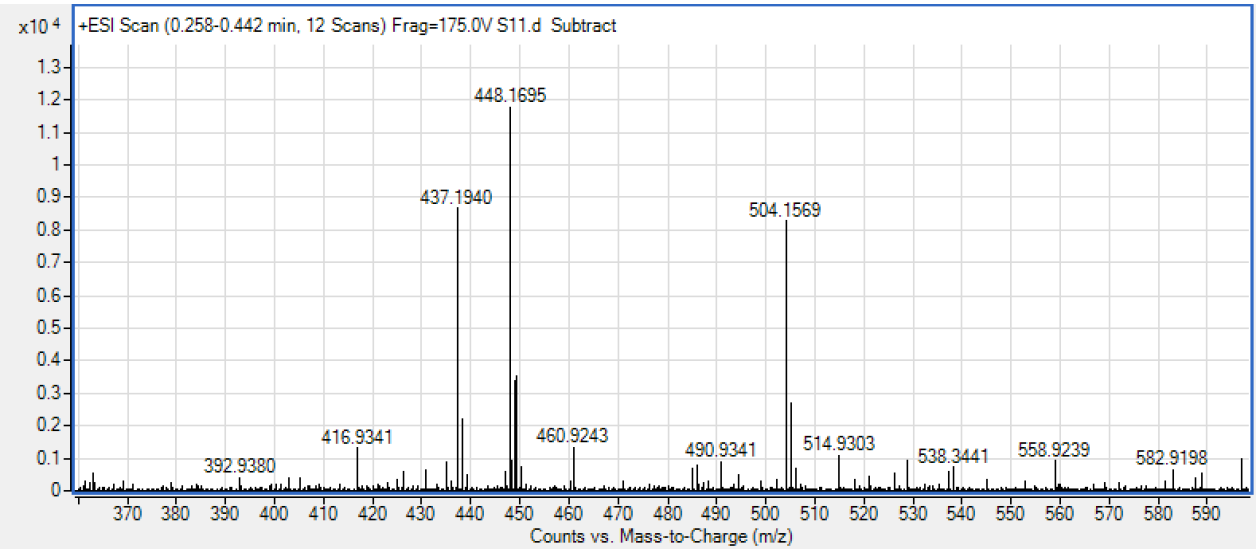

Figure S17. ^{1}H NMR, ^{13}C NMR, HRMS of **B2Cou**.

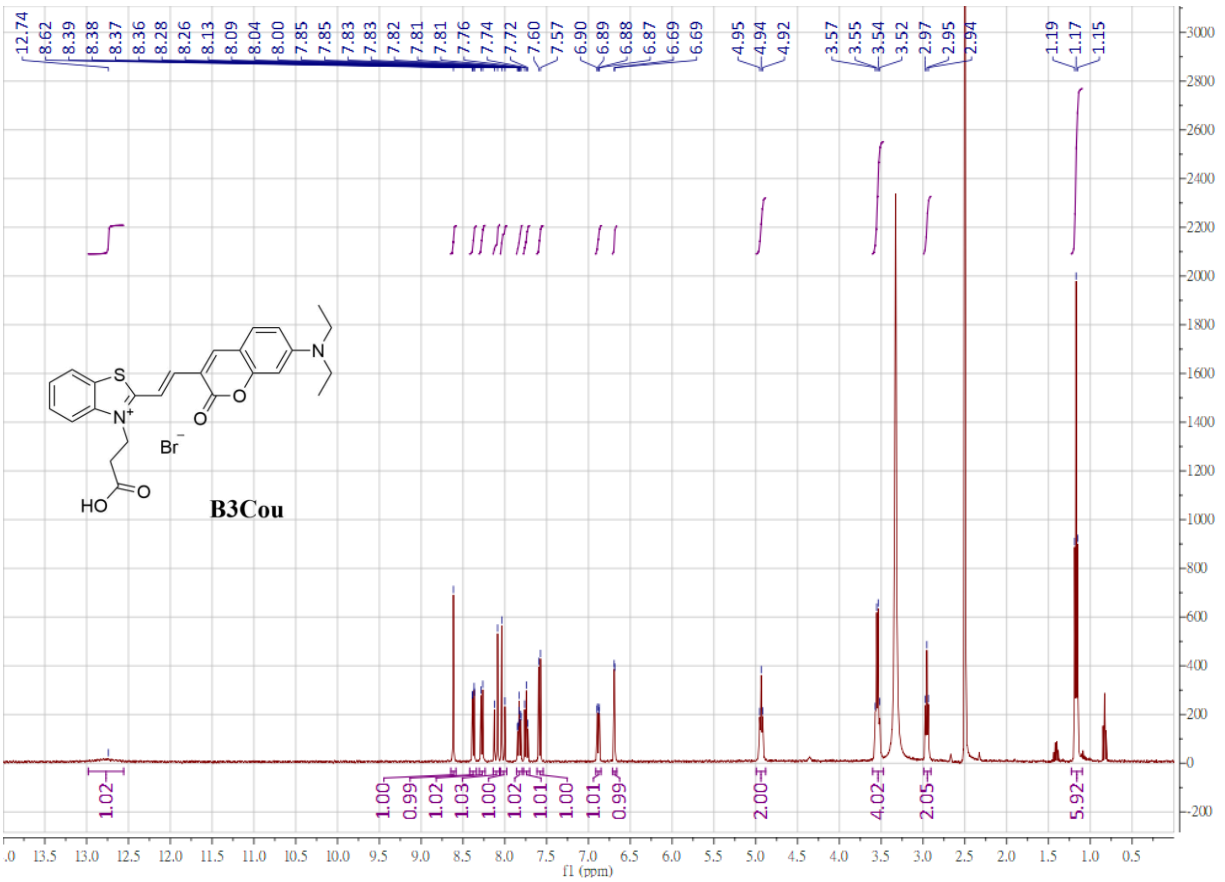
12.74
8.62
8.39
8.38
8.37
8.36
8.28
8.26
8.13
8.09
8.04
8.00
7.85
7.85
7.83
7.83
7.82
7.81
7.81
7.76
7.74
7.72
7.60
7.57
6.90
6.89
6.88
6.87
6.69
6.69
4.95
4.94
4.92
3.57
3.55
3.54
3.52
2.97
2.95
2.94
1.19
1.17
1.15
1.02
1.00
0.99
1.02
1.03
1.00
1.02
1.01
1.00
1.01
0.99
2.00
4.02
2.05
5.92
f1 (ppm)
B3Cou

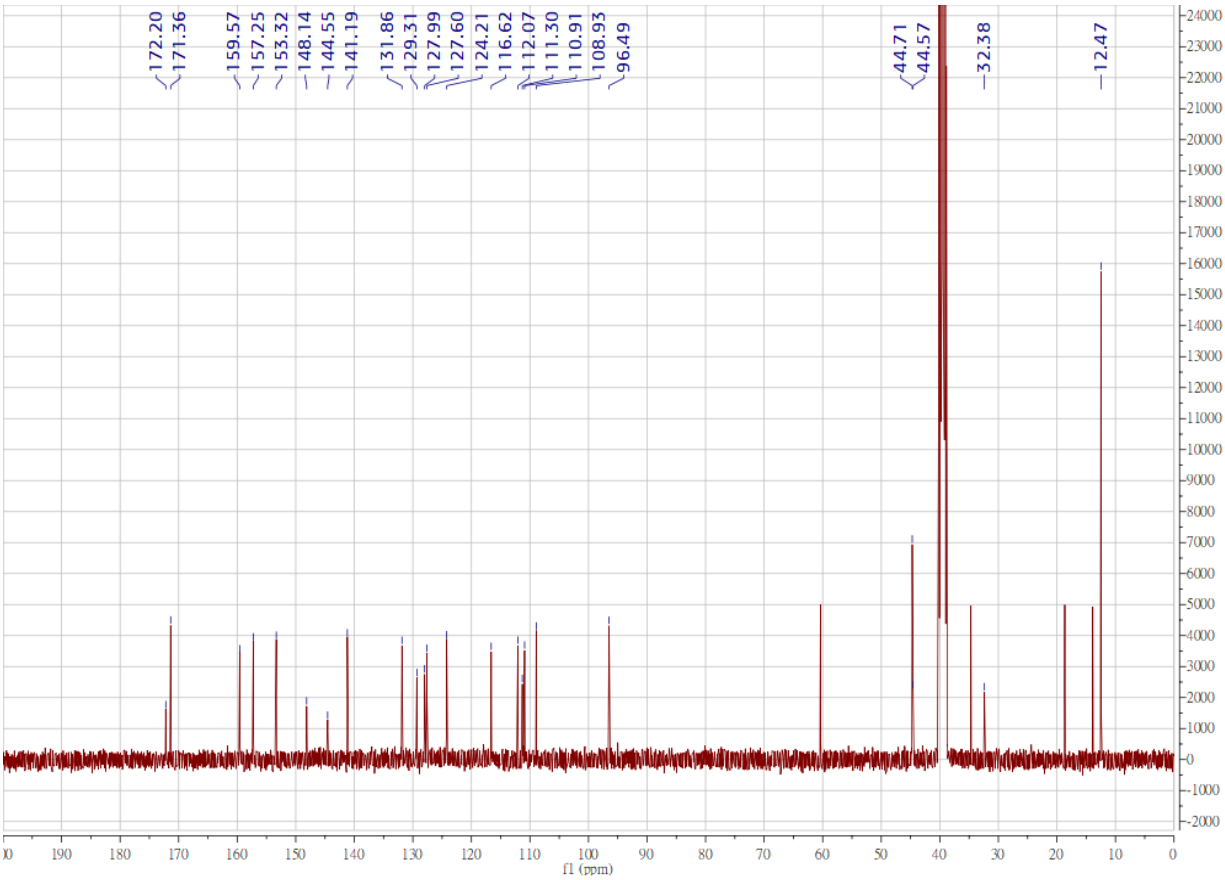
172.20
171.36
159.57
157.25
153.32
148.14
144.55
141.19
131.86
129.31
127.99
127.60
124.21
116.62
112.07
111.30
110.91
108.93
96.49
44.71
44.57
32.38
12.47
f1 (ppm)

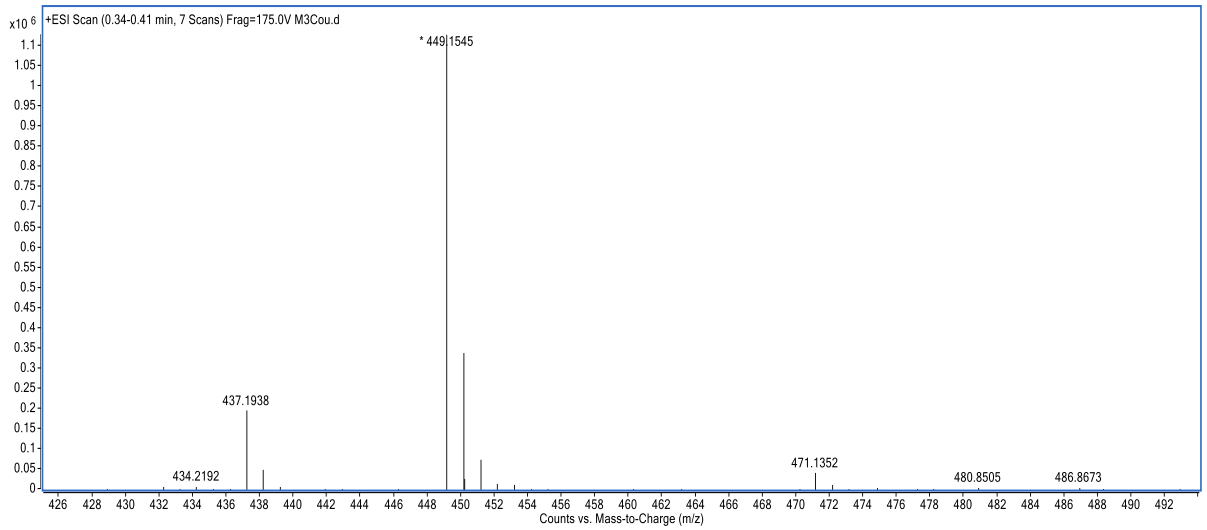

Figure S18. ^{1}H NMR, ^{13}C NMR and HRMS of **B3Cou**.

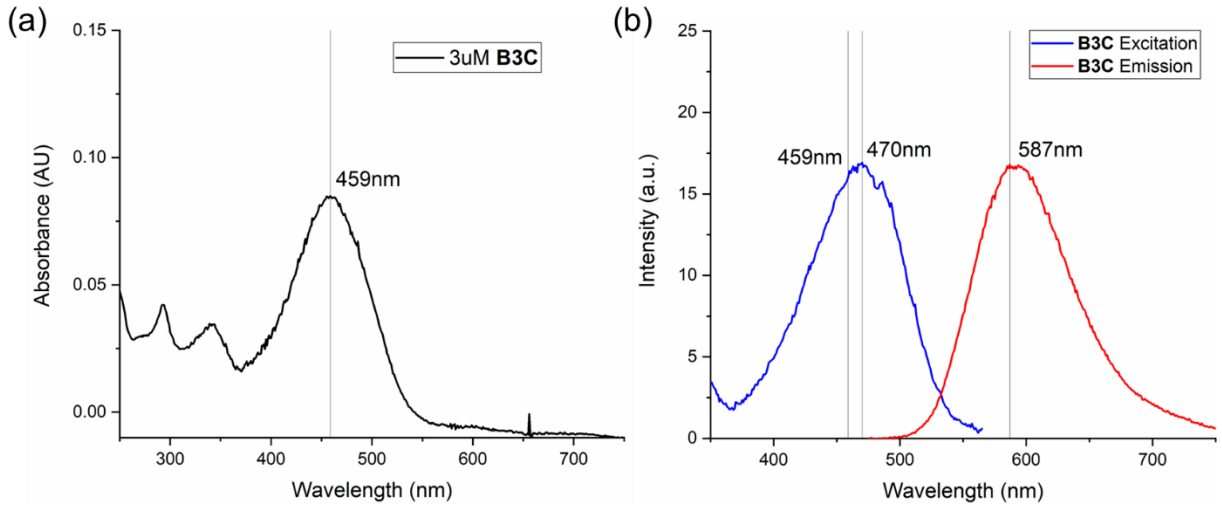

Figure S19. (a) UV-vis spectrum of **B3C** (3 μM) dissolved in Milli-Q water (with 1% DMSO). (b) Fluorescent excitation and emission spectra of **B3C** dissolved in Milli-Q water (with 1% DMSO).

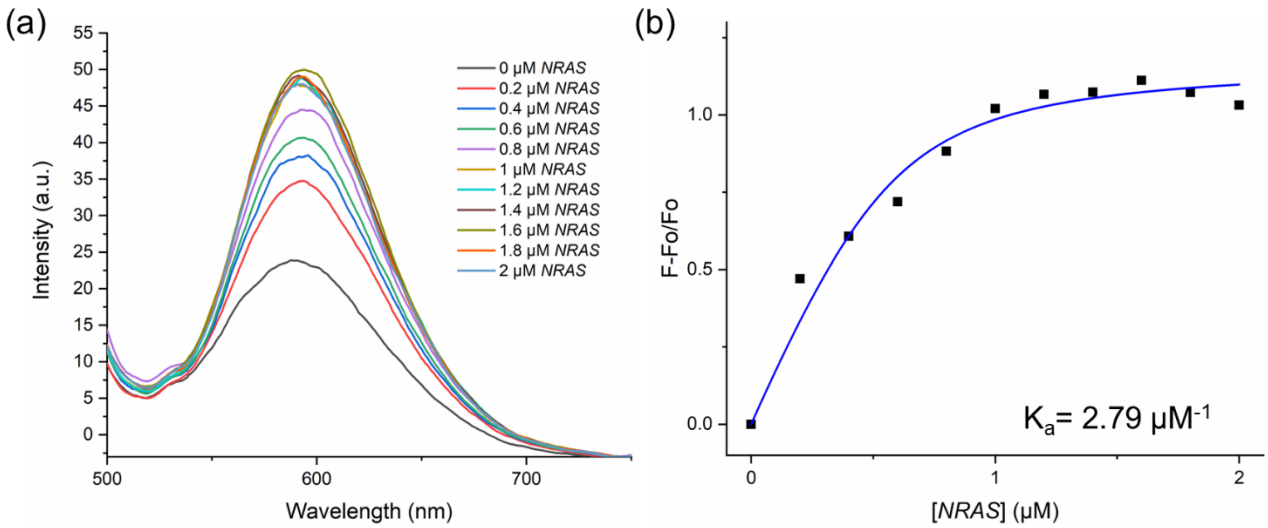

Figure S20. (a) Fluorescent titration spectra of **B3C** (1 μM) with *NRAS* RNA-G4 (0-2 μM) in a tris-HCl buffer (10 mM, pH 7.4) containing 60 mM KCl. (b) Fitted binding curve (blue curve) of **B3C** with *NRAS* to estimate the binding constant (K_a). F_0 represents the fluorescence intensity without *NRAS* and F represents the fluorescence intensity (emission at 593 nm) after adding *NRAS*. Titration conditions: **B3C** (1 μM) with *NRAS* in a Tris-HCl buffer (10 mM, pH 7.4) containing 60 mM KCl at room temperature.

Reference

[1] B. Alberts, A. Johnson, J. Lewis, D. Morgan, M.C. Raff, K. Roberts, P. Walter, J. Wilson, T. Hunt, Molecular biology of the cell, Sixth edition. ed., Garland Science, New York, NY, 2015.

[2] D. Varshney, J. Spiegel, K. Zyner, D. Tannahill, S. Balasubramanian, The regulation and functions of DNA and RNA G-quadruplexes, Nat Rev Mol Cell Biol 21(8) (2020) 459-474. https://doi.org/10.1038/s41580-020-0236-x.

[3] V. Sanchez-Martin, C. Lopez-Pujante, M. Soriano-Rodriguez, J.A. Garcia-Salcedo, An Updated Focus on Quadruplex Structures as Potential Therapeutic Targets in Cancer, Int J Mol Sci 21(23) (2020). https://doi.org/10.3390/ijms21238900.

[4] G.W. Collie, G.N. Parkinson, The application of DNA and RNA G-quadruplexes to therapeutic medicines, Chem Soc Rev 40(12) (2011) 5867-92. https://doi.org/10.1039/c1cs15067g.

[5] D. Sen, W. Gilbert, Formation of parallel four-stranded complexes by guanine-rich motifs in DNA and its implications for meiosis, Nature (London) 334(6180) (1988) 364-366. https://doi.org/10.1038/334364a0.

[6] V.S. Chambers, G. Marsico, J.M. Boutell, M. Di Antonio, G.P. Smith, S. Balasubramanian, High-throughput sequencing of DNA G-quadruplex structures in the human genome, Nature biotechnology 33(8) (2015) 877-881. https://doi.org/10.1038/nbt.3295.

[7] R. Hänsel-Hertsch, J. Spiegel, G. Marsico, D. Tannahill, S. Balasubramanian, Genome-wide mapping of endogenous G-quadruplex DNA structures by chromatin immunoprecipitation and high-throughput sequencing, Nature protocols 13(3) (2018) 551-564. https://doi.org/10.1038/nprot.2017.150.

[8] J. Kim, C. Cheong, P.B. Moore, Tetramerization of an RNA oligonucleotide containing a GGGG sequence, Nature (London) 351(6324) (1991) 331-332. https://doi.org/10.1038/351331a0.

[9] P. Kharel, S. Balaratnam, N. Beals, S. Basu, The role of RNA G-quadruplexes in human diseases and therapeutic strategies, Wiley Interdiscip Rev RNA 11(1) (2020) e1568. https://doi.org/10.1002/wrna.1568.

[10] E.A. Venczel, D. Sen, Parallel and antiparallel G-DNA structures from a complex telomeric sequence, Biochemistry (Easton) 32(24) (1993) 6220-6228. https://doi.org/10.1021/bi00075a015.

[11] M. Sravani, V. Nagaveni, S. Prabhakar, M. Vairamani, G-Quadruplex formation of deoxyguanosine in the presence of alkaline earth metal ions studied by electrospray ionization mass spectrometry, Rapid communications in mass spectrometry 25(14) (2011) 2095-2098. https://doi.org/10.1002/rcm.5082.

[12] S. Balaratnam, S. Basu, Divalent cation-aided identification of physico-chemical properties of metal ions that stabilize RNA g-quadruplexes, BIOPOLYMERS 103(7) (2015) 376-386. https://doi.org/10.1002/bip.22628.

[13] C.-F. Tang, R.H. Shafer, Engineering the Quadruplex Fold: Nucleoside Conformation Determines Both Folding Topology and Molecularity in Guanine Quadruplexes, Journal of the American Chemical Society 128(17) (2006) 5966-5973. https://doi.org/10.1021/ja0603958.

[14] D.-H. Zhang, T. Fujimoto, S. Saxena, H.-Q. Yu, D. Miyoshi, N. Sugimoto, Monomorphic RNA G-Quadruplex and Polymorphic DNA G-Quadruplex Structures Responding to Cellular Environmental Factors, Biochemistry (Easton) 49(21) (2010) 4554-4563. https://doi.org/10.1021/bi1002822.
[15] B. Saccà, L. Lacroix, J.-L. Mergny, The effect of chemical modifications on the thermal stability of different G-quadruplex-forming oligonucleotides, Nucleic acids research 33(4) (2005) 1182-1192. https://doi.org/10.1093/nar/gki257.
[16] D. Bhattacharyya, G. Mirihana Arachchilage, S. Basu, Metal Cations in G-Quadruplex Folding and Stability, Front Chem 4 (2016) 38. https://doi.org/10.3389/fchem.2016.00038.
[17] C.J. Webb, Y. Wu, V.A. Zakian, DNA repair at telomeres: Keeping the ends intact, Cold Spring Harbor perspectives in biology 5(6) (2013) a012666-a012666. https://doi.org/10.1101/cshperspect.a012666.
[18] W.E. Wright, V.M. Tesmer, K.E. Huffman, S.D. Levene, J.W. Shay, Normal human chromosomes have long G-rich telomeric overhangs at one end, Genes & development 11(21) (1997) 2801-2809. https://doi.org/10.1101/gad.11.21.2801.
[19] P. Baumann, T.R. Cech, Pot1, the Putative Telomere End-Binding Protein in Fission Yeast and Humans, Science (American Association for the Advancement of Science) 292(5519) (2001) 1171-1175. https://doi.org/10.1126/science.1060036.
[20] A.M. Zahler, J.R. Williamson, T.R. Cech, D.M. Prescott, Inhibition of telomerase by G-quartet DNA structures, Nature (London) 350(6320) (1991) 718-720. https://doi.org/10.1038/350718a0.
[21] C.M. Incles, C.M. Schultes, H. Kempski, H. Koehler, L.R. Kelland, S. Neidle, A G-quadruplex telomere targeting agent produces p16-associated senescence and chromosomal fusions in human prostate cancer cells, Molecular cancer therapeutics 3(10) (2004) 1201-1206. https://doi.org/10.1158/1535-7163.1201.3.10.
[22] T. Taka, L. Huang, A. Wongnoppavich, S.-W. Tam-Chang, T.R. Lee, W. Tuntiwechapikul, Telomere shortening and cell senescence induced by perylene derivatives in A549 human lung cancer cells, Bioorganic & medicinal chemistry 21(4) (2013) 883-890. https://doi.org/10.1016/j.bmc.2012.12.020.
[23] W. Long, B.X. Zheng, X.H. Huang, M.T. She, A.L. Liu, K. Zhang, W.L. Wong, Y.J. Lu, Molecular Recognition and Imaging of Human Telomeric G-Quadruplex DNA in Live Cells: A Systematic Advancement of Thiazole Orange Scaffold To Enhance Binding Specificity and Inhibition of Gene Expression, J Med Chem 64(4) (2021) 2125-2138. https://doi.org/10.1021/acs.jmedchem.0c01656.
[24] A. Ambrus, D. Chen, J. Dai, R.A. Jones, D. Yang, Solution Structure of the Biologically Relevant G-Quadruplex Element in the Human c-MYC Promoter. Implications for G-Quadruplex Stabilization, Biochemistry (Easton) 44(6) (2005) 2048-2058. https://doi.org/10.1021/bi048242p.
[25] V. González, K. Guo, L. Hurley, D. Sun, Identification and Characterization of Nucleolin as a c-myc G-quadruplex-binding Protein, The Journal of biological chemistry 284(35) (2009) 23622-23635. https://doi.org/10.1074/jbc.M109.018028.

[26] U. Siebenlist, L. Hennighausen, J. Battey, P. Leder, Chromatin structure and protein binding in the putative regulatory region of the c-myc gene in burkitt lymphoma, Cell 37(2) (1984) 381-391. https://doi.org/10.1016/0092-8674(84)90368-4.
[27] T. Simonsson, M. Kubista, P. Pecinka, DNA tetraplex formation in the control region of c-myc, Nucleic acids research 26(5) (1998) 1167-1172. https://doi.org/10.1093/nar/26.5.1167.
[28] T.L. Davis, A.B. Firulli, A.J. Kinniburgh, Ribonucleoprotein and Protein Factors Bind to an H-DNA-Forming c-myc DNA Element: Possible Regulators of the c-myc Gene, Proceedings of the National Academy of Sciences - PNAS 86(24) (1989) 9682-9686. https://doi.org/10.1073/pnas.86.24.9682.
[29] S.-J. Adam, L.G. Cory, J.B. David, H.H. Laurence, Direct Evidence for a G-Quadruplex in a Promoter Region and Targeting with a Small Molecule to Repress c-MYC Transcription, Proceedings of the National Academy of Sciences - PNAS 99(18) (2002) 11593-11598.
[30] W. Long, B.X. Zheng, Y. Li, X.H. Huang, D.M. Lin, C.C. Chen, J.Q. Hou, T.M. Ou, W.L. Wong, K. Zhang, Y.J. Lu, Rational design of small-molecules to recognize G-quadruplexes of c-MYC promoter and telomere and the evaluation of their in vivo antitumor activity against breast cancer, Nucleic Acids Res 50(4) (2022) 1829-1848. https://doi.org/10.1093/nar/gkac090.
[31] E.-A. Raiber, R. Kranaster, E. Lam, M. Nikan, S. Balasubramanian, A non-canonical DNA structure is a binding motif for the transcription factor SP1 in vitro, Nucleic acids research 40(4) (2012) 1499-1508. https://doi.org/10.1093/nar/gkr882.
[32] M. Bejugam, M. Gunaratnam, S. Müller, D.A. Sanders, S. Sewitz, J.A. Fletcher, S. Neidle, S. Balasubramanian, Targeting the c-Kit Promoter G-quadruplexes with 6-Substituted Indenoisoquinolines, ACS medicinal chemistry letters 1(7) (2010) 306-310. https://doi.org/10.1021/ml100062z.
[33] M. Bejugam, S. Sewitz, P.S. Shirude, R. Rodriguez, R. Shahid, S. Balasubramanian, Trisubstituted Isoalloxazines as a New Class of G-Quadruplex Binding Ligands: Small Molecule Regulation of c-kit Oncogene Expression, Journal of the American Chemical Society 129(43) (2007) 12926-12927. https://doi.org/10.1021/ja075881p.
[34] J.R. Nevins, The Rb/E2F pathway and cancer, Human molecular genetics 10(7) (2001) 699-703. https://doi.org/10.1093/hmg/10.7.699.
[35] A.I.H. Murchie, D.M.J. Lilley, Retinoblastoma susceptibility genes contain 5′ sequences with a high propensity to form guanine-tetrad structures, Nucleic acids research 20(1) (1992) 49-53. https://doi.org/10.1093/nar/20.1.49.
[36] Y. Xu, H. Sugiyama, Formation of the G-quadruplex and i-motif structures in retinoblastoma susceptibility genes (Rb), Nucleic acids research 34(3) (2006) 949-954. https://doi.org/10.1093/nar/gkj485.
[37] S. Kumari, J.L. Huppert, S. Balasubramanian, A. Bugaut, An RNA G-quadruplex in the 5′ UTR of the NRAS proto-oncogene modulates translation, Nature chemical biology 3(4) (2007) 218-221. https://doi.org/10.1038/nchembio864.
[38] A. Arora, M. Dutkiewicz, V. Scaria, M. Hariharan, S. Maiti, J. Kurreck, Inhibition of

translation in living eukaryotic cells by an RNA G-quadruplex motif, RNA (Cambridge) 14(7) (2008) 1290-1296. https://doi.org/10.1261/rna.1001708.
[39] M.J. Morris, Y. Negishi, C. Pazsint, J.D. Schonhoft, S. Basu, An RNA G-Quadruplex Is Essential for Cap-Independent Translation Initiation in Human VEGF IRES, Journal of the American Chemical Society 132(50) (2010) 17831-17839. https://doi.org/10.1021/ja106287x.
[40] P.H. Wanrooij, J.P. Uhler, T. Simonsson, M. Falkenberg, C.M. Gustafsson, G-quadruplex structures in RNA stimulate mitochondrial transcription termination and primer formation, Proc Natl Acad Sci U S A 107(37) (2010) 16072-7. https://doi.org/10.1073/pnas.1006026107.
[41] J.-D. Beaudoin, J.-P. Perreault, Exploring mRNA 3′-UTR G-quadruplexes: Evidence of roles in both alternative polyadenylation and mRNA shortening, Nucleic acids research 41(11) (2013) 5898-5911. https://doi.org/10.1093/nar/gkt265.
[42] D. Gomez, T. Lemarteleur, L. Lacroix, P. Mailliet, J.L. Mergny, J.F.o. Riou, Telomerase downregulation induced by the G-quadruplex ligand 12459 in A549 cells is mediated by hTERT RNA alternative splicing, Nucleic acids research 32(1) (2004) 371-379. https://doi.org/10.1093/nar/gkh181.
[43] A.C. Blice-Baum, M.-R. Mihailescu, Biophysical characterization of G-quadruplex forming FMR1 mRNA and of its interactions with different fragile X mental retardation protein isoforms, RNA (Cambridge) 20(1) (2014) 103-114. https://doi.org/10.1261/rna.041442.113.
[44] Z.-Y. Yu, W.-H. Luo, X.-C. Chen, S.-B. Chen, Z.-S. Huang, J.-H. Tan, Efficient and rational development of a new fluorescent probe specific for RNA G-quadruplex imaging in cells, Sensors and Actuators B: Chemical 324 (2020). https://doi.org/10.1016/j.snb.2020.128770.
[45] S.B. Chen, M.H. Hu, G.C. Liu, J. Wang, T.M. Ou, L.Q. Gu, Z.S. Huang, J.H. Tan, Visualization of NRAS RNA G-Quadruplex Structures in Cells with an Engineered Fluorogenic Hybridization Probe, J Am Chem Soc 138(33) (2016) 10382-5. https://doi.org/10.1021/jacs.6b04799.
[46] A. Bugaut, R. Rodriguez, S. Kumari, S.T. Hsu, S. Balasubramanian, Small molecule-mediated inhibition of translation by targeting a native RNA G-quadruplex, Org Biomol Chem 8(12) (2010) 2771-6. https://doi.org/10.1039/c002418j.
[47] S.K. Wang, Y. Wu, X.Q. Wang, G.T. Kuang, Q. Zhang, S.L. Lin, H.Y. Liu, J.H. Tan, Z.S. Huang, T.M. Ou, Discovery of Small Molecules for Repressing Cap-Independent Translation of Human Vascular Endothelial Growth Factor (hVEGF) as Novel Antitumor Agents, J Med Chem 60(13) (2017) 5306-5319. https://doi.org/10.1021/acs.jmedchem.6b01444.
[48] J. Dai, Z.Q. Liu, X.Q. Wang, J. Lin, P.F. Yao, S.L. Huang, T.M. Ou, J.H. Tan, D. Li, L.Q. Gu, Z.S. Huang, Discovery of Small Molecules for Up-Regulating the Translation of Antiamyloidogenic Secretase, a Disintegrin and Metalloproteinase 10 (ADAM10), by Binding to the G-Quadruplex-Forming Sequence in the 5' Untranslated Region (UTR) of Its mRNA, J Med Chem 58(9) (2015) 3875-91. https://doi.org/10.1021/acs.jmedchem.5b00139.
[49] C. Jaubert, A. Bedrat, L. Bartolucci, C. Di Primo, M. Ventura, J.L. Mergny, S. Amrane, M.L. Andreola, RNA synthesis is modulated by G-quadruplex formation in Hepatitis C virus negative RNA strand, Sci Rep 8(1) (2018) 8120. https://doi.org/10.1038/s41598-018-26582-3.

[50] D. Drygin, A. Siddiqui-Jain, J.K.C. Lim, D. Von Hoff, K. Anderes, W.G. Rice, S. O'Brien, M. Schwaebe, A. Lin, J. Bliesath, C.B. Ho, C. Proffitt, K. Trent, J.P. Whitten, Anticancer Activity of CX-3543: A Direct Inhibitor of rRNA Biogenesis, Cancer research (Chicago, Ill.) 69(19) (2009) 7653-7661. https://doi.org/10.1158/0008-5472.CAN-09-1304.
[51] E. Sanij, K.M. Hannan, J.C. Xuan, S.F. Yan, J.E. Ahern, A.S. Trigos, N. Brajanovski, J. Son, K.T. Chan, O. Konashova, E. Lieschke, M.J. Wakefield, D. Frank, S. Ellis, C. Cullinane, J. Kang, G. Poortinga, P. Nag, A.J. Deans, K.K. Khanna, L. Mileshkin, G.A. McArthur, J. Soong, E. Berns, R.D. Hannan, C.L. Scott, K.E. Sheppard, R.B. Pearson, CX-5461 activates the DNA damage response and demonstrates therapeutic efficacy in high-grade serous ovarian cancer, Nature communications 11(1) (2020) 2641-2641. https://doi.org/10.1038/s41467-020-16393-4.
[52] J. Hilton, K. Gelmon, P.L. Bedard, D. Tu, H. Xu, A.V. Tinker, R. Goodwin, S.A. Laurie, D. Jonker, A.R. Hansen, Z.W. Veitch, D.J. Renouf, L. Hagerman, H. Lui, B. Chen, D. Kellar, I. Li, S.-E. Lee, T. Kono, B.Y.C. Cheng, D. Yap, D. Lai, S. Beatty, J. Soong, K.I. Pritchard, I. Soria-Bretones, E. Chen, H. Feilotter, M. Rushton, L. Seymour, S. Aparicio, D.W. Cescon, Results of the phase I CCTG IND.231 trial of CX-5461 in patients with advanced solid tumors enriched for DNA-repair deficiencies, Nature communications 13(1) (2022) 3607-3607. https://doi.org/10.1038/s41467-022-31199-2.
[53] G.W. Collie, S. Sparapani, G.N. Parkinson, S. Neidle, Structural basis of telomeric RNA quadruplex--acridine ligand recognition, J Am Chem Soc 133(8) (2011) 2721-8. https://doi.org/10.1021/ja109767y.
[54] A. Baudrimont, S. Voegeli, E.C. Viloria, F. Stritt, M. Lenon, T. Wada, V. Jaquet, A. Becskei, Multiplexed gene control reveals rapid mRNA turnover, Science advances 3(7) (2017) e1700006-e1700006. https://doi.org/10.1126/sciadv.1700006.
[55] N. Puget, K.M. Miller, G. Legube, Non-canonical DNA/RNA structures during Transcription-Coupled Double-Strand Break Repair: Roadblocks or Bona fide repair intermediates?, DNA repair 81 (2019) 102661-102661. https://doi.org/10.1016/j.dnarep.2019.102661.
[56] H. Técher, S. Koundrioukoff, A. Nicolas, M. Debatisse, The impact of replication stress on replication dynamics and DNA damage in vertebrate cells, Nature reviews. Genetics 18(9) (2017) 535-550. https://doi.org/10.1038/nrg.2017.46.
[57] P. Castillo Bosch, S. Segura-Bayona, W. Koole, J.T. van Heteren, J.M. Dewar, M. Tijsterman, P. Knipscheer, FANCJ promotes DNA synthesis through G-quadruplex structures, The EMBO journal 33(21) (2014) 2521-2533. https://doi.org/10.15252/embj.201488663.
[58] K. Paeschke, M.L. Bochman, P. Daniela Garcia, P. Cejka, K.L. Friedman, S.C. Kowalczykowski, V.A. Zakian, Pif1 family helicases suppress genome instability at G-quadruplex motifs, Nature (London) 497(7450) (2013) 458-462. https://doi.org/10.1038/nature12149.
[59] W. Peng, Z.Y. Sun, Q. Zhang, S.Q. Cheng, S.K. Wang, X.N. Wang, G.T. Kuang, X.X. Su, J.H. Tan, Z.S. Huang, T.M. Ou, Design, Synthesis, and Evaluation of Novel p-(Methylthio)styryl Substituted Quindoline Derivatives as Neuroblastoma RAS (NRAS) Repressors via Specific Stabilizing the RNA G-Quadruplex, J Med Chem 61(15) (2018) 6629-6646.

https://doi.org/10.1021/acs.jmedchem.8b00257.
[60] G. Miglietta, S. Cogoi, J. Marinello, G. Capranico, A.S. Tikhomirov, A. Shchekotikhin, L.E. Xodo, RNA G-Quadruplexes in Kirsten Ras (KRAS) Oncogene as Targets for Small Molecules Inhibiting Translation, J Med Chem 60(23) (2017) 9448-9461. https://doi.org/10.1021/acs.jmedchem.7b00622.
[61] E. Grabocka, Y. Pylayeva-Gupta, Mathew J.K. Jones, V. Lubkov, E. Yemanaberhan, L. Taylor, Hao H. Jeng, D. Bar-Sagi, Wild-Type H- and N-Ras Promote Mutant K-Ras-Driven Tumorigenesis by Modulating the DNA Damage Response, Cancer cell 25(2) (2014) 243-256. https://doi.org/10.1016/j.ccr.2014.01.005.
[62] F.C. Kelleher, G.A. McArthur, Targeting NRAS in melanoma, The cancer journal (Sudbury, Mass.) 18(2) (2012) 132-136. https://doi.org/10.1097/PPO.0b013e31824ba4df.
[63] C.J. Der, D. Vigil, J. Cherfils, K.L. Rossman, Ras superfamily GEFs and GAPs: validated and tractable targets for cancer therapy?, Nature reviews. Cancer 10(12) (2010) 842-857. https://doi.org/10.1038/nrc2960.
[64] I. Wortzel, R. Seger, The ERK cascade: Distinct functions within various subcellular organelles, Genes & cancer 2(3) (2011) 195-209. https://doi.org/10.1177/1947601911407328.
[65] A. Boespflug, J. Caramel, S. Dalle, L. Thomas, Treatment of NRAS-mutated advanced or metastatic melanoma: rationale, current trials and evidence to date, Ther Adv Med Oncol 9(7) (2017) 481-492. https://doi.org/10.1177/1758834017708160.
[66] M. Eskandarpour, F. Huang, K.A. Reeves, E. Clark, J. Hansson, Oncogenic NRAS has multiple effects on the malignant phenotype of human melanoma cells cultured in vitro, Int J Cancer 124(1) (2009) 16-26. https://doi.org/10.1002/ijc.23876.
[67] I.V. Fedorenko, G.T. Gibney, K.S.M. Smalley, NRAS mutant melanoma: Biological behavior and future strategies for therapeutic management, Oncogene 32(25) (2013) 3009-3018. https://doi.org/10.1038/onc.2012.453.
[68] J.L. Bos, ras Oncogenes in human cancer: A review, Cancer research (Chicago, Ill.) 49(17) (1989) 4682-4689.
[69] J. Canon, K. Rex, A.Y. Saiki, C. Mohr, K. Cooke, D. Bagal, K. Gaida, T. Holt, C.G. Knutson, N. Koppada, B.A. Lanman, J. Werner, A.S. Rapaport, T. San Miguel, R. Ortiz, T. Osgood, J.-R. Sun, X. Zhu, J.D. McCarter, L.P. Volak, B.E. Houk, M.G. Fakih, B.H. O'Neil, T.J. Price, G.S. Falchook, J. Desai, J. Kuo, R. Govindan, D.S. Hong, W. Ouyang, H. Henary, T. Arvedson, V.J. Cee, J.R. Lipford, The clinical KRAS(G12C) inhibitor AMG 510 drives anti-tumour immunity, Nature (London) 575(7781) (2019) 217-223. https://doi.org/10.1038/s41586-019-1694-1.
[70] Z.R.T. Sumirtha Balaratnam, David R. Calabrese, Michael T. Banco, Kamyar Yazdani,, A.R.F.-D.A. Xiao Liang, Danny Incarnato, and John S. Schneekloth Jr, Investigating the NRAS 5' UTR as a Target for Small Molecules, Obesity, fitness, & wellness week (2022) 1031.
[71] J. Nygren, N. Svanvik, M. Kubista, The interactions between the fluorescent dye thiazole orange and DNA, BIOPOLYM 46(1) (1998) 39-51. https://doi.org/10.1002/(SICI)1097-0282(199807)46:1<39::AID-BIP4>3.0.CO;2-Z.

[72] J. Mohanty, N. Barooah, V. Dhamodharan, S. Harikrishna, P.I. Pradeepkumar, A.C. Bhasikuttan, Thioflavin T as an efficient inducer and selective fluorescent sensor for the human telomeric G-quadruplex DNA, J Am Chem Soc 135(1) (2013) 367-76. https://doi.org/10.1021/ja309588h.
[73] S. Xu, Q. Li, J. Xiang, Q. Yang, H. Sun, A. Guan, L. Wang, Y. Liu, L. Yu, Y. Shi, H. Chen, Y. Tang, Thioflavin T as an efficient fluorescence sensor for selective recognition of RNA G-quadruplexes, Scientific reports 6(1) (2016) 24793-24793. https://doi.org/10.1038/srep24793.
[74] B.X. Zheng, M.T. She, W. Long, Y.Y. Xu, Y.H. Zhang, X.H. Huang, W. Liu, J.Q. Hou, W.L. Wong, Y.J. Lu, A small-sized benzothiazole-indolium fluorescent probe: the study of interaction specificity targeting c-MYC promoter G-quadruplex structures and live cell imaging, Chem Commun (Camb) 56(95) (2020) 15016-15019. https://doi.org/10.1039/d0cc06525k.
[75] X. Luo, B. Xue, G. Feng, J. Zhang, B. Lin, P. Zeng, H. Li, H. Yi, X.L. Zhang, H. Zhu, Z. Nie, Lighting up the Native Viral RNA Genome with a Fluorogenic Probe for the Live-Cell Visualization of Virus Infection, J Am Chem Soc 141(13) (2019) 5182-5191. https://doi.org/10.1021/jacs.8b10265.
[76] X. Lu, X. Wu, S. Kuang, C. Lei, Z. Nie, Visualization of Deep Tissue G-quadruplexes with a Novel Large Stokes-Shifted Red Fluorescent Benzothiazole Derivative, Anal Chem 94(28) (2022) 10283-10290. https://doi.org/10.1021/acs.analchem.2c02049.
[77] J.W. Yan, W.J. Ye, S.B. Chen, W.B. Wu, J.Q. Hou, T.M. Ou, J.H. Tan, D. Li, L.Q. Gu, Z.S. Huang, Development of a universal colorimetric indicator for G-quadruplex structures by the fusion of thiazole orange and isaindigotone skeleton, Anal Chem 84(15) (2012) 6288-92. https://doi.org/10.1021/ac300207r.
[78] X.C. Chen, S.B. Chen, J. Dai, J.H. Yuan, T.M. Ou, Z.S. Huang, J.H. Tan, Tracking the Dynamic Folding and Unfolding of RNA G-Quadruplexes in Live Cells, Angew Chem Int Ed Engl 57(17) (2018) 4702-4706. https://doi.org/10.1002/anie.201801999.
[79] A. Gluszynska, B. Juskowiak, M. Kuta-Siejkowska, M. Hoffmann, S. Haider, Carbazole ligands as c-myc G-quadruplex binders, Int J Biol Macromol 114 (2018) 479-490. https://doi.org/10.1016/j.ijbiomac.2018.03.135.
[80] N.I. Shank, H.H. Pham, A.S. Waggoner, B.A. Armitage, Twisted Cyanines: A Non-Planar Fluorogenic Dye with Superior Photostability and its Use in a Protein-Based Fluoromodule, Journal of the American Chemical Society 135(1) (2013) 242-251. https://doi.org/10.1021/ja308629w.
[81] Y. Venkata Suseela, P. Sengupta, T. Roychowdhury, S. Panda, S. Talukdar, S. Chattopadhyay, S. Chatterjee, T. Govindaraju, Targeting Oncogene Promoters and Ribosomal RNA Biogenesis by G-Quadruplex Binding Ligands Translate to Anticancer Activity, ACS Bio & Med Chem Au 2(2) (2021) 125-139. https://doi.org/10.1021/acsbiomedchemau.1c00039.
[82] S. Asamitsu, S. Obata, Z. Yu, T. Bando, H. Sugiyama, Recent Progress of Targeted G-Quadruplex-Preferred Ligands Toward Cancer Therapy, Molecules 24(3) (2019). https://doi.org/10.3390/molecules24030429.

[83] N. Kosiol, S. Juranek, P. Brossart, A. Heine, K. Paeschke, G-quadruplexes: a promising target for cancer therapy, Molecular cancer 20(1) (2021) 40-40. https://doi.org/10.1186/s12943-021-01328-4.
[84] X. Cao, L. Meng, Z. Li, Y. Mao, H. Lan, L. Chen, Y. Fan, T. Yi, Large Red-Shifted Fluorescent Emission via Intermolecular π–π Stacking in 4-Ethynyl-1,8-naphthalimide-Based Supramolecular Assemblies, Langmuir 30(39) (2014) 11753-11760. https://doi.org/10.1021/la503299j.
[85] P. Agarwala, S. Pandey, S. Maiti, The tale of RNA G-quadruplex, Org Biomol Chem 13(20) (2015) 5570-85. https://doi.org/10.1039/c4ob02681k.
[86] G. Biffi, M. Di Antonio, D. Tannahill, S. Balasubramanian, Visualization and selective chemical targeting of RNA G-quadruplex structures in the cytoplasm of human cells, Nat Chem 6(1) (2014) 75-80. https://doi.org/10.1038/nchem.1805.
[87] M. Garavís, B. López-Méndez, A. Somoza, J. Oyarzabal, C. Dalvit, A. Villasante, R.n. Campos-Olivas, C. González, Discovery of Selective Ligands for Telomeric RNA G-quadruplexes (TERRA) through 19F-NMR Based Fragment Screening, ACS chemical biology 9(7) (2014) 1559-1566. https://doi.org/10.1021/cb500100z.
[88] C.M. Azzalin, P. Reichenbach, L. Khoriauli, E. Giulotto, J. Lingner, Telomeric Repeat-Containing RNA and RNA Surveillance Factors at Mammalian Chromosome Ends, Science (American Association for the Advancement of Science) 318(5851) (2007) 798-801. https://doi.org/10.1126/science.1147182.
[89] M.A. Blasco, S. Schoeftner, Developmentally regulated transcription of mammalian telomeres by DNA-dependent RNA polymerase II, Nature cell biology 10(2) (2008) 228-236. https://doi.org/10.1038/ncb1685.
[90] Z. Deng, J. Norseen, A. Wiedmer, H. Riethman, P.M. Lieberman, TERRA RNA Binding to TRF2 Facilitates Heterochromatin Formation and ORC Recruitment at Telomeres, Molecular cell 35(4) (2009) 403-413. https://doi.org/10.1016/j.molcel.2009.06.025.
[91] N. Bettin, C. Oss Pegorar, E. Cusanelli, The Emerging Roles of TERRA in Telomere Maintenance and Genome Stability, Cells (Basel, Switzerland) 8(3) (2019) 246. https://doi.org/10.3390/cells8030246.
[92] B.-K. Oh, Y. Choi, J. Bae, W.M. Lee, J.-K. Hoh, J.S. Choi, Increased amounts and stability of telomeric repeat-containing RNA (TERRA) following DNA damage induced by etoposide, PloS one 14(11) (2019) e0225302. https://doi.org/10.1371/journal.pone.0225302.s008.
[93] W. Klapper, W. Qian, C. Schulte, R. Parwaresch, DNA damage transiently increases TRF2 mRNA expression and telomerase activity, Leukemia 17(10) (2003) 2007-2015. https://doi.org/10.1038/sj.leu.2403086.
[94] Y. Katsuda, S.-i. Sato, L. Asano, Y. Morimura, T. Furuta, H. Sugiyama, M. Hagihara, M. Uesugi, A Small Molecule That Represses Translation of G-Quadruplex-Containing mRNA, Journal of the American Chemical Society 138(29) (2016) 9037-9040. https://doi.org/10.1021/jacs.6b04506.
[95] L.J. Mah, A. El-Osta, T.C. Karagiannis, γH2AX: a sensitive molecular marker of DNA damage

and repair, Leukemia 24(4) (2010) 679-686. https://doi.org/10.1038/leu.2010.6.
[96] X.U. Yi, X.I.N. Zhang, H. Jeong, Y.M. Shin, D.H. Park, S. You, D.-K. Kim, A novel bispidinone analog induces S-phase cell cycle arrest and apoptosis in HeLa human cervical carcinoma cells, Oncology reports 33(3) (2015) 1526-1532. https://doi.org/10.3892/or.2015.3722.
[97] Z. Xu, F. Zhang, C. Bai, C. Yao, H. Zhong, C. Zou, X. Chen, Sophoridine induces apoptosis and S phase arrest via ROS-dependent JNK and ERK activation in human pancreatic cancer cells, Journal of experimental & clinical cancer research 36(1) (2017) 124-124. https://doi.org/10.1186/s13046-017-0590-5.
[98] Z. Pan, Y. Luo, Y. Xia, X. Zhang, Y. Qin, W. Liu, M. Li, X. Liu, Q. Zheng, D. Li, Cinobufagin induces cell cycle arrest at the S phase and promotes apoptosis in nasopharyngeal carcinoma cells, Biomedicine & pharmacotherapy 122 (2020) 109763-109763. https://doi.org/10.1016/j.biopha.2019.109763.
[99] A. Abulaiti, A.J. Fikaris, O.M. Tsygankova, J.L. Meinkoth, Ras induces chromosome instability and abrogation of the DNA damage response, Cancer research (Chicago, Ill.) 66(21) (2006) 10505-10512. https://doi.org/10.1158/0008-5472.CAN-06-2351.
[100] M. Podhorecka, A. Skladanowski, P. Bozko, H2AX Phosphorylation: Its Role in DNA Damage Response and Cancer Therapy, Journal of nucleic acids 2010 (2010) 1-9. https://doi.org/10.4061/2010/920161.
[101] A. Campos, A. Clemente-Blanco, Cell cycle and DNA repair regulation in the damage response: Protein phosphatases take over the reins, International journal of molecular sciences 21(2) (2020) 446. https://doi.org/10.3390/ijms21020446.
[102] F. Sadoughi, J. Hallajzadeh, Z. Asemi, M.A. Mansournia, F. Alemi, B. Yousefi, Signaling pathways involved in cell cycle arrest during the DNA breaks, DNA repair 98 (2021) 103047-103047. https://doi.org/10.1016/j.dnarep.2021.103047.
[103] Y.N. Yu, M. Fang, Y.F. Dai, X.R. Chen, On the relationship between adenosine diphosphoribosyl transferase and S phase DNA synthesis in cultured mammalian cells, Proc Chin Acad Med Sci Peking Union Med Coll 4(3) (1989) 157-61.
[104] L.R. Barkley, H. Ohmori, C. Vaziri, Integrating S-phase checkpoint signaling with trans-lesion synthesis of bulky DNA adducts, Cell biochemistry and biophysics 47(3) (2007) 392-408. https://doi.org/10.1007/s12013-007-0032-7.
[105] H. Bae, Y.-H. Go, T. Kwon, B.J. Sung, H.-J. Cha, A Theoretical Model for the Cell Cycle and Drug Induced Cell Cycle Arrest of FUCCI Systems with Cell-to-Cell Variation during Mitosis, Pharmaceutical research 36(4) (2019) 57-13. https://doi.org/10.1007/s11095-019-2570-2.
[106] H.X. Chao, C.E. Poovey, A.A. Privette, G.D. Grant, H.Y. Chao, J.G. Cook, J.E. Purvis, Orchestration of DNA Damage Checkpoint Dynamics across the Human Cell Cycle, Cell systems 5(5) (2017) 445-459.e5. https://doi.org/10.1016/j.cels.2017.09.015.
[107] N. Hustedt, D. Durocher, The control of DNA repair by the cell cycle, Nature cell biology 19(1) (2017) 1-9. https://doi.org/10.1038/ncb3452.
[108] Y. Anno, T. Kubo, R. Ueki, M. Yano, K. Sasaki, H. Ohba, M. Fujii, Synthesis of DNA

Conjugates by Solid Phase Fragment Condensation, Nucleosides, nucleotides & nucleic acids 22(5-8) (2003) 1451-1453. https://doi.org/10.1081/NCN-120023008.
[109] R. Kumari, P. Jat, Mechanisms of Cellular Senescence: Cell Cycle Arrest and Senescence Associated Secretory Phenotype, Frontiers in cell and developmental biology 9 (2021) 645593-645593. https://doi.org/10.3389/fcell.2021.645593.
[110] J.C.M. Mombach, C.A. Bugs, C. Chaouiya, Modelling the onset of senescence at the G1/S cell cycle checkpoint, BMC genomics 15(7) (2014) S7-S7. https://doi.org/10.1186/1471-2164-15-S7-S7.
[111] C. Wang, Y.-J. Lu, S.-Y. Cai, W. Long, Y.-Y. Zheng, J.-W. Lin, Y. Yan, X.-H. Huang, W.-L. Wong, K. Zhang, C.-F. Chow, Advancing small ligands targeting RNA for better binding affinity and specificity: A study of structural influence through molecular design approach, Sensors and Actuators B: Chemical 262 (2018) 386-394. https://doi.org/10.1016/j.snb.2018.02.004.